2013-01-01

Integration Of Memristors With Mems For Dynamic Displacement Control

Sergio Fabian Almeida Loya
University of Texas at El Paso, sfalmeida@miners.utep.edu

INTEGRATION OF MEMRISTORS WITH MEMS FOR DYNAMIC DISPLACEMENT CONTROL

SERGIO FABIAN ALMEIDA LOYA

Department of Electrical and Computer Engineering

APPROVED:

David Zubia, Ph.D., Chair

Jose Mireles Jr., Ph.D.

Joseph Pierluissi, Ph.D.

Eric MacDonald, Ph.D.

Ernest J Garcia, Ph.D.

Benjamin C. Flores, Ph.D.
Dean of the Graduate School

Dedication

To my wife and daughter

INTEGRATION OF MEMRISTORS WITH MEMS FOR DYNAMIC DISPLACEMENT CONTROL

by

SERGIO FABIAN ALMEIDA LOYA, MS

DISSERTATION

Presented to the Faculty of the Graduate School of

The University of Texas at El Paso

in Partial Fulfillment

of the Requirements

for the Degree of

DOCTOR OF PHILOSOPHY

Department of Electrical and Computer Engineering

THE UNIVERSITY OF TEXAS AT EL PASO

December 2013

Acknowledgements

I am very grateful for the opportunity of being involved in this experience and be part of an excellent research group. I want to express gratitude to my mentor, friend, and committee chair Dr. David Zubia, who inspired and guided me throughout my research work and gave me the opportunity to be part of this research project. Also I would like to thank my committee members Dr. Jose Mireles Jr., Dr. Joseph Pierluissi, Eric MacDonald, and Dr. Ernest J Garcia for their support and valuable guidance. This work was supported by Sandia National Laboratories.

A special thanks to Arka Talukdar for his help and ideas. I would also like to thank the nanoMIL students and friends for their help and useful ideas: Brandon Aguirre, Jose Chavez, and Ghassan K. Kachmar. Their feedback and advice were important to accomplish this research work.

Finally, I would like to thank my wife Haydee, my daughter Abigail, my mother Norma, my little sister Anally, and my father Refugio who have been my inspiration and motivation throughout life. Thank you for all your love, patience and support.

Abstract

In recent years the demand for high-speed, lower power consumption and large-capacity non-volatile memories has increased. Promisingly the memristor can be used due to its special characteristic of having memory through resistance change. The memristor behavior is not limited to digital applications but it can be used in analog application as well including: memristors in chaotic circuits, amoeba's learning, neural synaptic emulation, reprogrammable and reconfigurable circuits, and for neuromorphic computers. On the other hand Micro Electro Mechanical Systems (MEMS) are small scale structures that can interact with the physical world due to their mechanical properties. These devices are widely used in diverse applications such as: accelerometers, pressure sensors, micro-optics, biosensors, tilting mirrors, and RF switches. One of the most common MEMS devices is the electrostatic actuator which moves a metal electrode when a voltage is applied; however these actuators are limited to one third of its gap. The purpose of this work is to investigate the potential of the integration of these two devices and extend the application branch of the memristor.

This work starts with the integration of the MEMS parallel plate capacitor and the memristor in a simple series circuit configuration where it is possible to observe that the displacement can be a function of the memristance giving the possibility of interpreting the upper electrode position in form of resistance instead of capacitance. Thus the memristor has the potential to sense the MEMS dynamics for different applications. The current in this configuration is limited by the MEMS restricting the change in the resistance of the memristor. To overcome this disadvantage different amplification stages are investigated to maximize the charge interaction between both devices using a BJT amplification, a MOSFET amplification, and an Op Amp stage.

Finally the memristor is used as a sensor element for the MEMS displacement in a simple design for a voltage close-loop control in order to improve the MEMS operation range. In the final control design it is shown that the MEMS upper plate can be stabilized up to 95% of the total gap with low power consumption. Thus the memristor can play an important role overcoming the limited operation range of the MEMS actuators

Table of Contents

List of tables

List of Figures

1 Introduction

In recent years the demand for high-speed, lower power consumption and large-capacity non-volatile memories has increased. Several alternatives have emerged in order to meet this demand. Within the alternatives is the resistance random access memory (ReRAM) [1]. Promisingly, ReRAM can be implemented using memristor devices due to its special characteristic of having memory through resistance change. The memristor is a feasible option for this application because of its simple metal/metal-oxide/metal (MOM) structure, which can be arranged in form of crossbar architectures. Many applications for memristors besides non-volatile memories have been proposed including: memristors in chaotic circuits [2], amoeba's learning [3], neural synaptic emulation [4], reprogrammable and reconfigurable circuits [5], and for neuromorphic computers [6].

On the other hand Micro Electro Mechanical Systems (MEMS) are small scale structures that can interact with the physical world due to their mechanical properties. These devices can be created with state of the art integrated circuit (IC) fabrication technologies and are widely used in diverse applications such as: accelerometers [7], pressure sensors [8], micro-optics [9], biosensors [10], tilting mirrors [11], and RF switches [12]. One of the most versatile MEMS structures is the MEMS parallel plate capacitor which can be used as an actuator or sensing element [13] and it has a big potential for mobile communication terminals where variable plate capacitors or varicaps are needed for tuning the voltage controlled oscillators (VCO) [14].

Interestingly, charge transfer is an operating principle that is common to both memristors and certain kinds of MEMS devices such as parallel plate capacitors. More specifically, electronic charge transfer plays a central role in the capacitive operating principle of the parallel plates MEMS. Similarly, memristors use the migration of ions to change their resistance in response to charge flow. Unlike MEMS capacitors, memristors also demonstrate non-volatile memory of the charge transferred through the device. This ability makes the integration of memristors with MEMS capacitors highly intriguing to create capacitors with local memory storage in what can be called mems-capacitors.

Due to the variety of applications for these two devices and common operating principle the general concept of integrating memristors with MEMS has been postulated [15]. However the actual

details for the different synergies are lacking as well specific applications. This work consists in investigating the interaction of these two devices.

The integration of these two devices as well as the potential application is explained in five sections. In section one, an introduction of the memristor and parallel plate MEMS devices is presented as well their current applications and potential market. In section two, the operating principle for the memristor and parallel plate MEMS is explore individually. One of the main disadvantages of the parallel plate MEMS is the limited working range of one third of its potential capacity. In section three, the integration of these devices in a series-circuit configuration is studied where a correlation between the change in the resistance of the memristor and the MEMS dynamics is analyzed. This creates a new application for the memristor as a sensing element. Furthermore, it innovates the current measurement methods that measure the capacitance and are used to improve the MEMS working range. Although the correlation between these two devices was found, the resistance change is very small and unpractical to be measured. Section four analyzes an integration of the memristor and MEMS with an amplification stage in order to improve the correlation and the resistance change. Finally, in section five a new method to drive a parallel plate MEMS actuator integrating the memristor as feedback element is analyzed. This method improves the MEMS working range up to at least nighty five percent of its total capacity using a closed-loop voltage control and incorporating the memristor as position sensing element simplifying the capacitance methods.

1.1 MEMRISTOR AND ITS APPLICATIONS

Leon Chua in 1971 proposed for first time the existence of a new passive circuit element called "memristor" as contraction for "memory resistor" [16]. The memristor is a two-terminal device which links two fundamental circuit variables similar to the resistor, capacitor, and inductor; for that reason it is called the fourth basic circuit element. Chua predicted the existence of the memristor by observing that one relation of the fundamental circuit variables (voltage (V), current (i), electric charge (q), and magnetic flux (Φ_m)) remained undefined. Specifically the link between the magnetic flux and the electric charge was not defined by any device unlike the current and the voltage that are linked by the

resistor, the voltage and the charge by the capacitor, and the current and the flux by the inductor as shown in Figure 1. Therefore the memristor was needed to define the missing link.

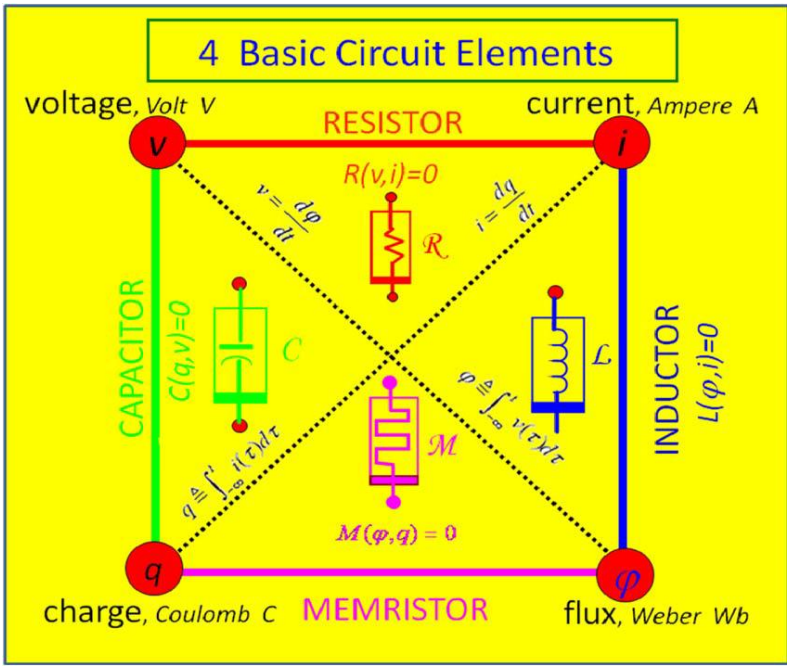

Figure 1. Fundamental circuit variables relationships [17].

Mathematically, the memristor is described by,

$$V = M(q)i$$

Equation 1

where $M(q)$ is the memristance and is given by,

$$M(q) \equiv \frac{d\varphi}{dq}.$$

Equation 2

Equation 1 shows that the memristor is similar to a resistor and the unit of the memristance is Ohms. However the memristance describes the change of the magnetic flux with respect to the charge (*q)* instead of the change of the voltage with respect to the current, as expressed in Equation 2. This new device was illustrated with a new symbol, Figure 2, proposed by Leon Chua and it is been used since then.

Figure 2. Memristor symbol.

Equation 1 and Equation 2 can show that the memristance will depend on its previous states, thus the memristor is able to store memory of its previous events through its *M* (memristance) value. This phenomenon can be illustrated as follows: assuming the charge a function of the magnetic flux, as shown in Figure 3(A), where two different slopes are present. Then a voltage pulse in the form of Figure 3(B) is applied, and as a consequence of this voltage the magnetic flux will change due to the relationship $\varphi = \int V dt$, as shown in Figure 3 (C). If the value of the magnetic flux is such that $\frac{d\varphi}{dq}$ changes, when $\varphi = \varphi_n$. Then the memristance state will switch from one resistance value (M1) to another (M2) as in Figure 3 (D). In other words, when a device changes in resistance from one state to another and the state is maintained after the voltage is removed, then this device has a memristor behavior [18].

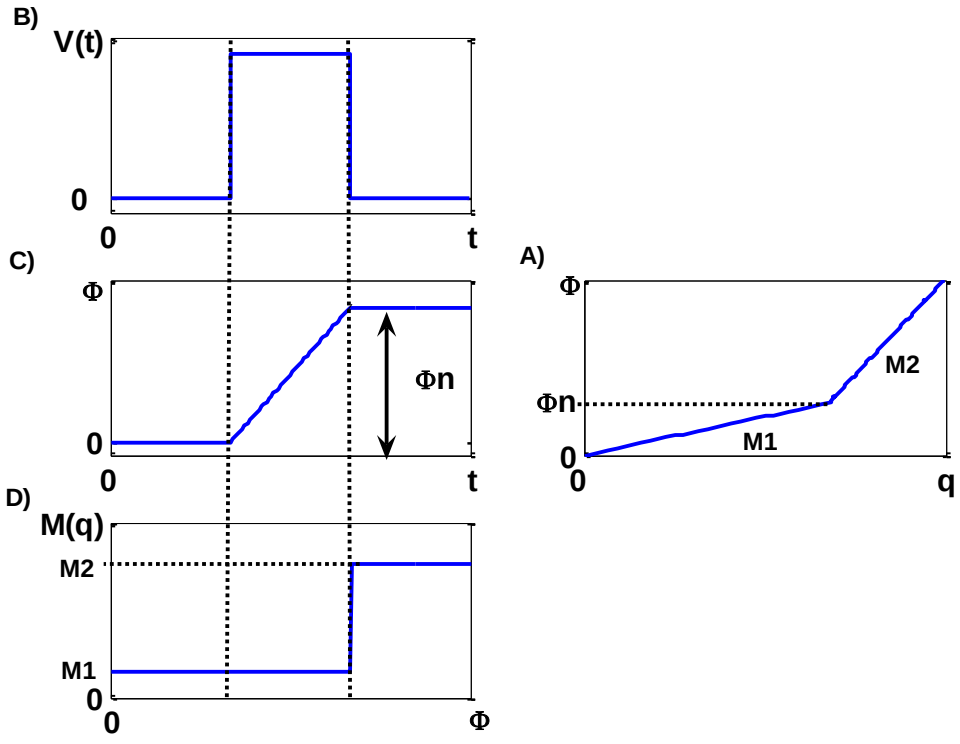

Figure 3. Memristance state change with a voltage pulse [18].

The original work of Chua was only theoretical and it was until 2008 that bipolar resistive switching behavior was related to the memristor device [19]. This relationship was noticed by Hewlett-Packard (HP) on a metal/metal-oxide/metal (MOM) structure using pt/ TiO_2/pt [20]. Since 1962 a large variety of MOM structures with diverse configurations have shown different types of resistive switching [21], which will be explained in the following section.

1.1.1 Classification of resistive switching types

The switching type is an essential characteristic for resistive switching in MOM structures which define the voltage polarity needed to change the resistance from high resistance state (HRS) to low resistance state (LRS) and vice versa. There are two types of resistive switching: bipolar and unipolar.

In the bipolar case a switch from HRS to LRS occurs when a set voltage with a defined polarity is applied. Then in order to return to switch backwards from LRS to HRS, the structure is submitted to a reset voltage with an opposite polarity to the set voltage [21]. Thus, both forward and reverse biases are required for resistive switching forming a hysteresis loop for the I-V characteristic curve as shown in Figure 4(A). In the Figure, the trace labeled "OFF" is in the HRS state and switches to LRS (trace labeled "ON") when a reverse bias is applied. Subsequently, the memristor switches from LRS to HRS when a forward bias is applied. In the practice when a switching from HRS to LRS occurs the current has to be limited to avoid device damage due to the sudden resistance change. This parameter is known as the compliance current (CC).

For the unipolar case a switch from HRS to LRS also occurs when a set voltage is applied between the contacts. Unlike the bipolar type, a reset voltage with the same polarity is required to switch between LRS and HRS [22]. Figure 4(B) shows this type of switching, where it is noticed that the reset voltage is smaller than the set voltage. This switching type can occur either with a reverse or forward bias depending on the MOM structure materials. The bipolar case in the practice is important to consider as well the compliance current used to switch from HRS to LRS. Also it is important to limit the reset voltage when it is switching from LRS to HRS to avoid device damage and recurrent switching. Figure 4 shows switching in reverse and forward voltage bias, the green line is the LRS and the red line is the HRS. The switching occurs only with one polarity but with different voltage levels.

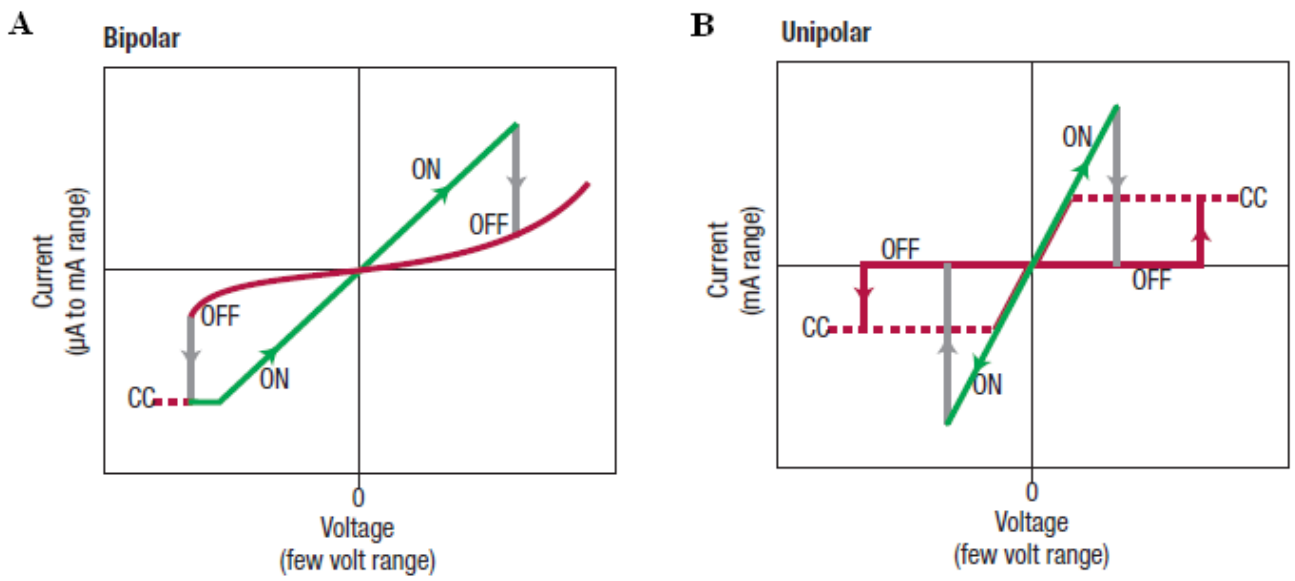

Figure 4. Resistive switching types; A) bipolar switching, B) unipolar switching [21].

Different MOM structures have been investigated for bipolar resistive switching including Au/ZnO/SS [23], Ti/ZrO_2/Pt [24], Au/HfO_2/Pt [25], Ti/MnO_2/Pt [26], and Pt/TiO_2/Pt [27]. As well, ITO/ZnO/ITO [28], Au/$ZnMnO_3$/Pt [29], Pt/Cu_2O/Pt [30], and Ag/SnO_2/Ti [31] MOM structures have been investigated for unipolar resistive switching.

1.1.3 Memristor applications

The variety of memristor applications has expanded over the last years due to its versatile behavior. In other words, this circuit element can be implemented in digital applications and similarly it can be implemented in complex analog applications without any change to its basic physical MOM structure [32]. A high density non-volatile memory fabricated with a memristor nanocrossbar, as shown in Figure 5 a), is an example for a digital application.

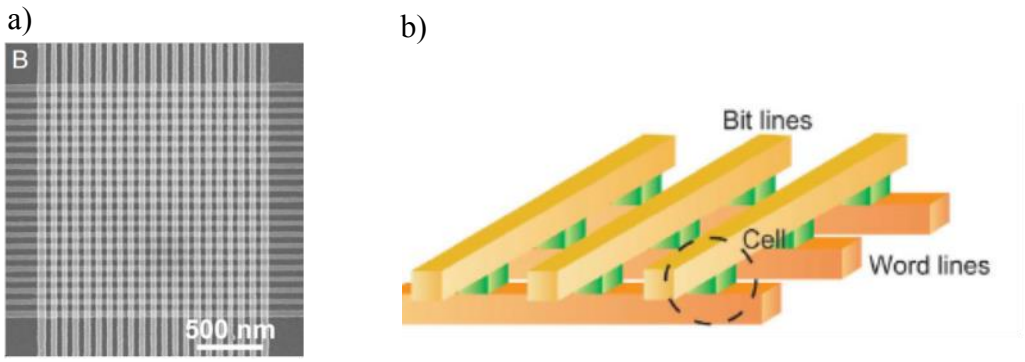

Figure 5. a) scanning electron microscope image of a nanocrossbar [5], b) bit cell memory representation [1].

Here the metal horizontal lines are the bottom electrode, or the first metal film, then after an oxide film is deposited on top of the bottom electrode, and finally the top electrodes are the vertical metal films. Each vertical and horizontal intersection represents a memory bit cell, as shown in Figure 5 b). Therefore, the physical memristor structure allows the fabrication of non-volatile memories arrays in very small areas and with few fabrication process steps. It is been predicted that the memory retention time can be up to 10 years [33] and that the switching time can be as fast as 10 ns [34].

Due to the versatility of the memristor behavior, where the resistance change levels can be controlled to be more than two (HRS and LRS), its application is not limited to digital but also the memristor can be implemented in analog applications as well. It has been demonstrated the capability of brain-like computing based on memristor devices [32] as well that this device can emulate the brain learning mechanism spike-time-dependent plasticity (STDP) [4]. Furthermore the combination of memristor with other circuit elements can lead to different applications like the model of an amoeba's learning represented by the circuit in Figure 6 [3]. In this case the change in the memristance represents the response of the *Physarum polycephalum* organism to different environment conditions.

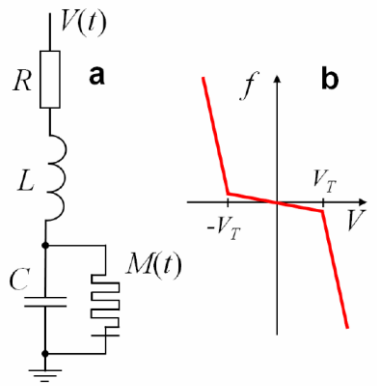

Figure 6. Circuit representation of an amoeba's learning to different environments [3].

Many other applications can be mentioned in both areas, Figure 7 shows a schematic of several applications that have been investigated separated by digital and analog [32].

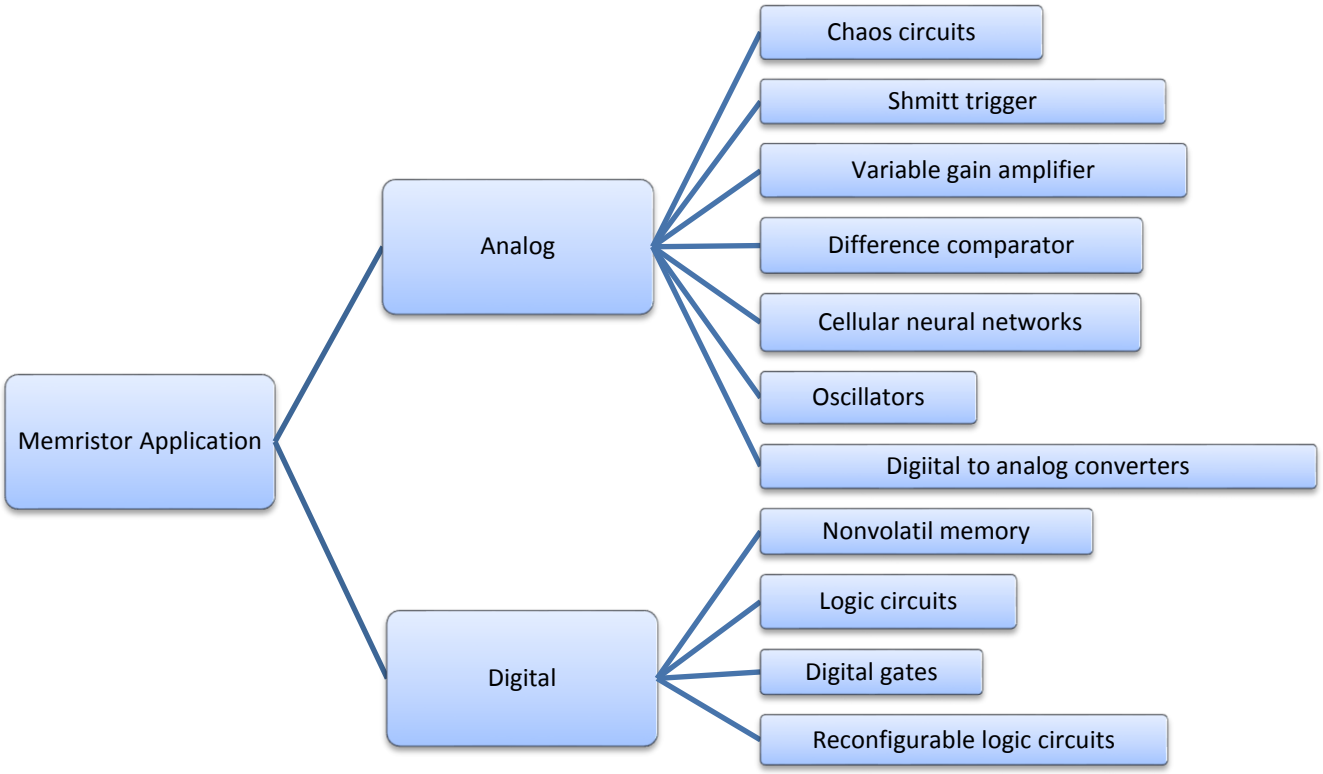

Figure 7. Analog and digital memristor applications.

These applications show the potential of memristors behavior. In this work a new integration of memristors with MEMS is explored in order to expand its application's branches.

1.2 MICRO ELECTRO MECHANICAL SYSTEMS (MEMS) AND ITS APPLICATIONS

The MEMS have been known for a while, these devices born with the discovery of the piezoresistive effects in silicon and germanium at the Bell laboratories around the early 1950s [35]. Over the last decades a broad range of MEMS devices have been developed, notable applications for these devices are the invention of scanning tunneling microscopy (STM) in 1981, and later the atomic force microscopy (AFM) in 1986 by Binnig [10].

There is a wide variety of MEMS devices that have been proposed and produced for commercial use at different applications. Figure 8 shows the current application market and a forecast of the market growth for the MEMS devices in 2015.

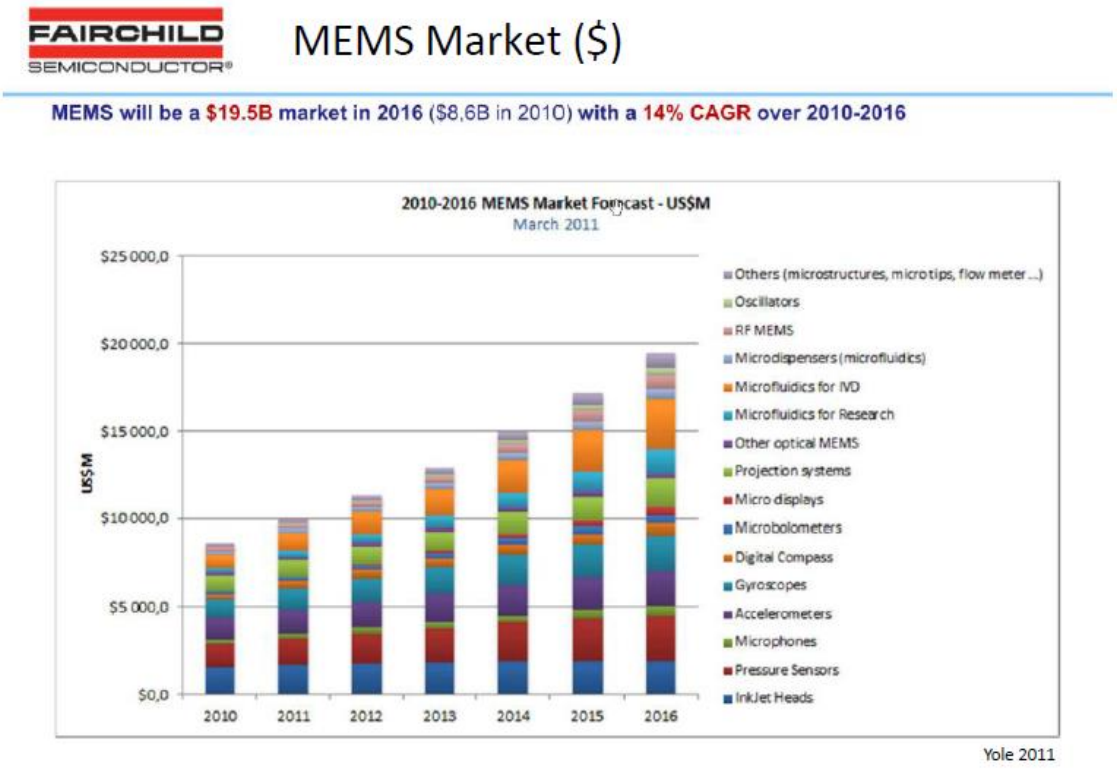

Figure 8. Forecast for the MEMS market in important applications [36].

One of the most versatile structure of MEMS is the parallel plate, due to its simple structure and the variety of available fabrication technologies to build it. Within the applications there are: microgrippers, micro-relays, gyro sensors, micromotors, cantilevers, optical shutters, optical attenuators and micromirros [35].

1.2.1 Parallel plate MEMS designs and applications

The basic physical structure of the parallel plate MEMS consist of two metal plates separated by an air gap, Figure 9 shows an example of this device where it is used as a capacitive MEMS RF switch [12]. For this type of device when a voltage is applied between the two contacts an attraction force is created, thus the two contacts will tend to close the gap between them. In this design the bottom electrode is fixed and the upper electrode is able to move. However there are forces that oppose to this attraction force, in particular the opposition of the upper electrode to deform. Depending on the MEMS design the upper electrode motion can be predetermined as well as the MEMS capacitance.

a) b)

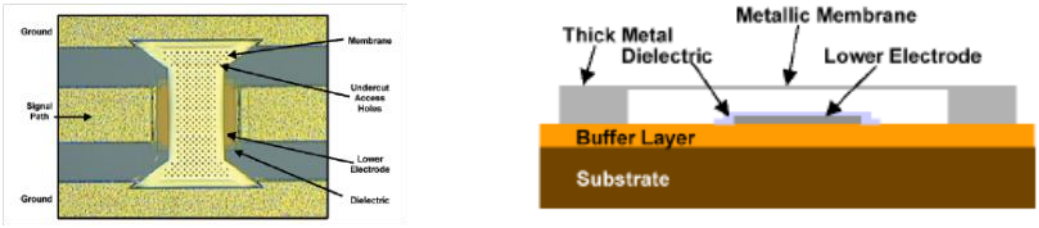

Figure 9. a) Top view picture and b) schematic representation of a MEMS RF switch [12].

Due to the advance in IC fabrication processes the parallel plate MEMS can have different configurations or designs; but its basic operating principle remains the same. Figure 10 shows another parallel plate MEMS design, this time it is for a voltage controlled oscillator (VCO) used in wireless systems [37]. The differences between these two designs are the area of the upper metal and the upper metal suspension structure. As consequence, there are different opposition forces to the upper electrode motion between both designs. Both approaches use a voltage between the two contacts to change the capacitance depending on the application.

a) b)

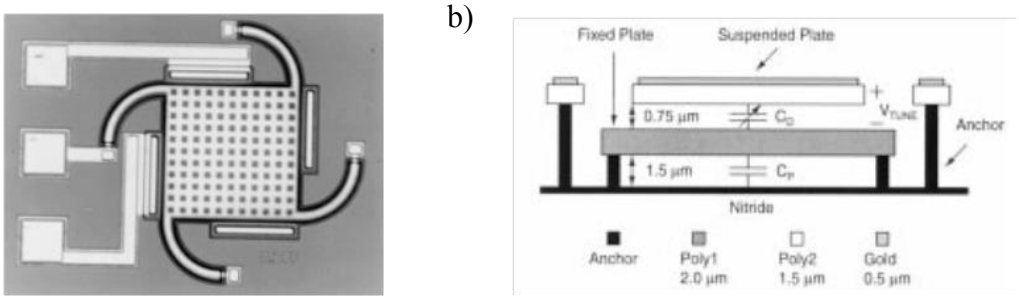

Figure 10. a) Top view picture and b) schematic representation of a MEMS VCO [37].

Another example of a different parallel plate MEMS design is shown in Figure 11, which is also used for RF switches [38]. In this case the upper electrode is a cantilever where one end of the upper electrode is fixed and the other end is totally free. In this case the force interactions occur in the middle of the total length and the switch contact takes place in the free end. The capacitance for this application is not important however a sustained and good contact is essential.

a) b)

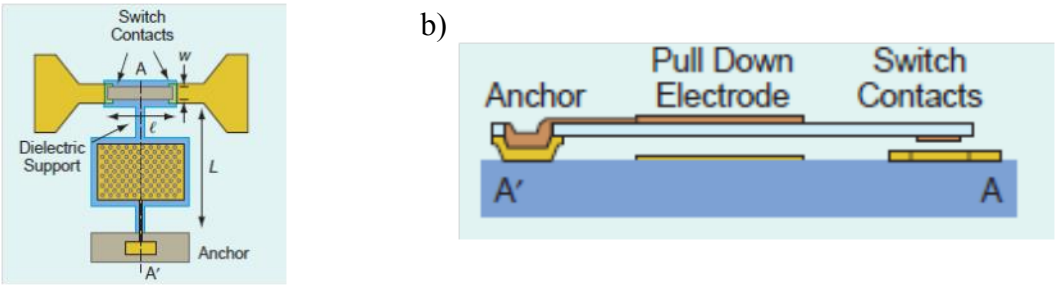

Figure 11. a) Top view picture and b) schematic representation of a MEMS switch [38].

Parallel plate MEMS plays an important role in optics as well, Figure 12 shows a design where parallel plate MEMS actuators are used to control the exact position of a mirror. Here the mirror is suspended with three bending beams, these beams are deformed through an array of MEMS actuators and according to the position of the actuators the mirror will tilt [39]. In the optics filed the MEMS can be used for adaptive optics [40], dual axis optical mirrors [41], light wave communications [42], and optical switches [43] [44] [45].

a) b)

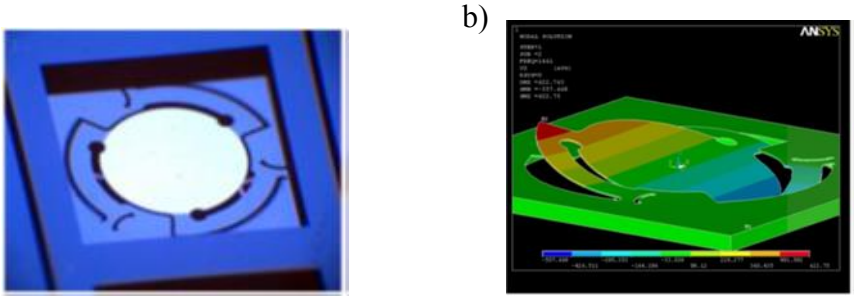

Figure 12. a) Top view picture and b) simulation of the deformation of a tilting MEMS mirror [39].

Consequently parallel plate MEMS have a wide range of applications due to its design flexibility while maintaining its basic operating principle. Its compatibility to IC fabrication allows the integration of these devices in different electronics and optics applications.

2 Operating Principles for Memristors and MEMS

2.1 MEMRISTOR MODELS

As mentioned in section 1.1.1 there are two types of memristor behaviors: bipolar and unipolar. Where the only difference between them is the voltage needed to change the resistance. For the bipolar case the change in the resistance depends on the polarity of the applied voltage whereas for the unipolar the change in the resistance depends on the magnitude of the applied voltage and not in the polarity. Even though the resistance change type in both cases is different it is been shown the filamentary resistive switching mechanism is similar for unipolar [46] and bipolar [33].

The filamentary resistive switching mechanism consists in formation and rupture of conductive filaments in the oxide layer. This mechanism has three states additionally to the original state as shown in Figure 23. The initial state is the oxide film (blue layer) without any conduction paths thus at this stage there is an insulation between the two metals (yellow layers). The first state is the forming process where conductive filaments are created in the oxide film applying a voltage in the metal contacts. The second and third states are called the reset and set, for the reset a small rupture in the filament is originated with an applied voltage thus the conductive channel is interrupted and the device will be at high resistance state (HRS). In the set state the filament rupture is regenerated as well with an applied voltage [1] and the device will switch to low resistance state (LRS). Therefore these devices can keep memory of its sates in form of resistance without any energy storage.

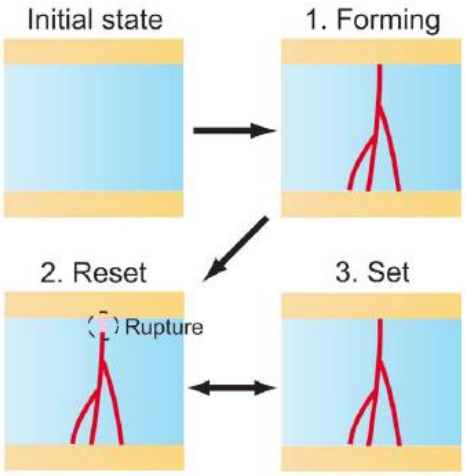

Figure 13. Filament forming mechanism for a memristor whit initial, forming, reset and set states [1].

Figure 14 a) and Figure 14 b) shows the I-V curves with the three states of a bipolar device with a Ti/TiO_2/Ti structure [33] and a unipolar device with a Ag/SnO_2/Ti structure [15] respectively. These graphs show the forming, reset, and set states proving a conductive path formation process.

a) b)

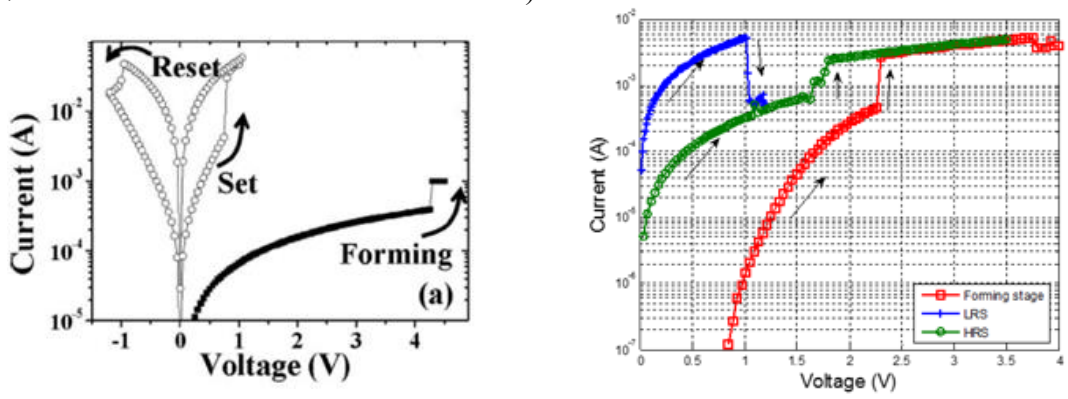

Figure 14. I-V curve of a) bipolar memristor [33] and b) unipolar memristor [15].

Even though the filamentary theory has been shown [47] to describe the resistive switching the physics behind the filament forming and the conductive mechanism is still under debate. Several theories have been postulated, in particular for Pt/TiO_2/Pt structures. This section will discuss different memristor device models in order to identify the most adequate for the integration with the MEMS.

2.1.1 Linear dopant drift memristor model

The basic mathematical formulation for a voltage controlled memristor proposed by Chua is the following:

$$v = R(w,i)i$$

Equation 3

$$\frac{dw}{dt} = f(w,i)$$

Equation 4

where R is the memristance and is a function of the state variable, w, and the device current, i. The state variable depends on time and the current that flows through the device. The state variable w is the fundamental characteristic of a memristor.

The linear dopant drift memristor (LDD) model was introduced for the first time by Strukov, *et al.* [20] in order to describe the memristor behavior in Pt/TiO_2/Pt structures. As shown in Figure 15 it is

considered that the TiO_2 film has two regions: one that is totally stoichiometric TiO_2 (undoped region) and the second one has some oxygen vacancies and is nonstoichiometric TiO_{2-x} (doped region). For this model, the state variable *w* is the length of the doped region. When a voltage is applied (with the positive polarity applied to the undoped region), the oxygen vacancies will drift to the undoped region increasing the length of *w*, and decreasing the resistance between the metals. When the voltage polarity is revered where the positive polarity is applied to the doped region, the oxygen vacancies will move towards the doped region, thus the w length will decrease and the device resistance will increase.

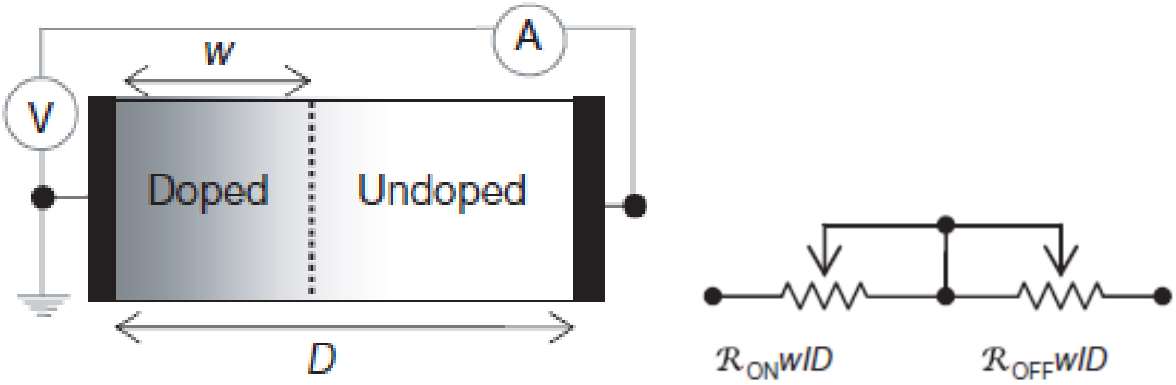

Figure 15. Graphic representation for the HP model and equivalent circuit for the equations 3 and 4 [20].

This model is represented by Equation 5 and Equation 6. Where *w* is the state variable and will change with respect to time if a current is passing through the device, *D* is the total oxide thickness, μ_v represents the average ion mobility, *Ron* is the low resistance (LR), and *Roff* is the high resistance (HR). From these equations it is possible to observe that if $w = D$ the memristor is in low resistance state (LRS) and if $w = 0$ the memristor is in high resistance state (HRS).

$$v(t) = \left(Ron \frac{w(t)}{D} + Roff\left(1 - \frac{w(t)}{D}\right)\right) i(t)$$

Equation 5

$$\frac{dw(t)}{dt} = \mu_V \frac{\mathrm{Ron}}{\mathrm{D}} i(t).$$

Equation 6

From Equation 6 it is possible to observe that when the device is submitted to a positive current the change of *w* with respect time will be positive indicating an increment of the doped region, in the same manner when the device is submitted to a negative current a decrement of the doped region will occur. These equations can be represented schematically with two variable resistors connected in series as shown in Figure 15. *w* controls the resistance variation; if *w = D, Roff* will be bypassed, the total resistance will be *Ron*, and vice versa when *w* = 0, *Ron* is bypassed and the total resistance is *Roff*. The memristance *M(w)* is given by:

$$M(w,t) = Ron\frac{w(t)}{D} + Roff\left(1 - \frac{w(t)}{D}\right).$$

Equation 7

The closed form solution for Equation 5 and Equation 6 can to be analyzed to study electrical behavior and physical constraints of the device. Equation 8 is obtained solving those equations as follows,

$$w(t) = \left(\frac{Ron}{Ron - Roff}\right)\left(\frac{DRoff}{Ron} \pm \sqrt{\left(\frac{DRoff}{Ron}\right)^2 - 2\mu_V\left(1 - \frac{Roff}{Ron}\right)\left(\int_{t_0}^{t} V(t)dt + c\right)}\right)$$

Equation 8

where *c* depends on the initial condition of *w*, in other words $w(t_0)$. This equation has several physical constraints that need to be taken in consideration. The first one is that the root square term always needs to be real which implies that the integral of the applied voltage needs to be restricted such that the square root term is between zero and one. If the integral of the applied voltage is zero, *w* will equal zero. On the other hand, if the square root term is equal to one, *w* will equate *D*, given that *w* equals zero initially. This restriction will limit the range of *w* between 0 and *D*. The second constraint is that *w* cannot be negative; therefore the positive and negative squares need to be evaluated such that the negative terms are discarded. These two constraints need to be considered when equation 3 and 4 are solved.

Figure 16 shows the current passing through the memristor (dotted line) solving Equation 5 and Equation 6. In this case an input voltage $v(t) = 0.8\sin(\omega_0 t)$ (solid line) was applied and the following

memristor parameters from Ref [20] were used: $\omega_0 = 2\pi$, $Ron = 100\ \Omega$, $Roff = 5000\ \Omega$, $\mu_v = 10^{-14} m^2 V^{-1} s^{-1}$, $D = 10x10^{-9}$ m, and initial condition $w(t_0) = 0$. The physical constraints mentioned above were also taken into account in the solution.

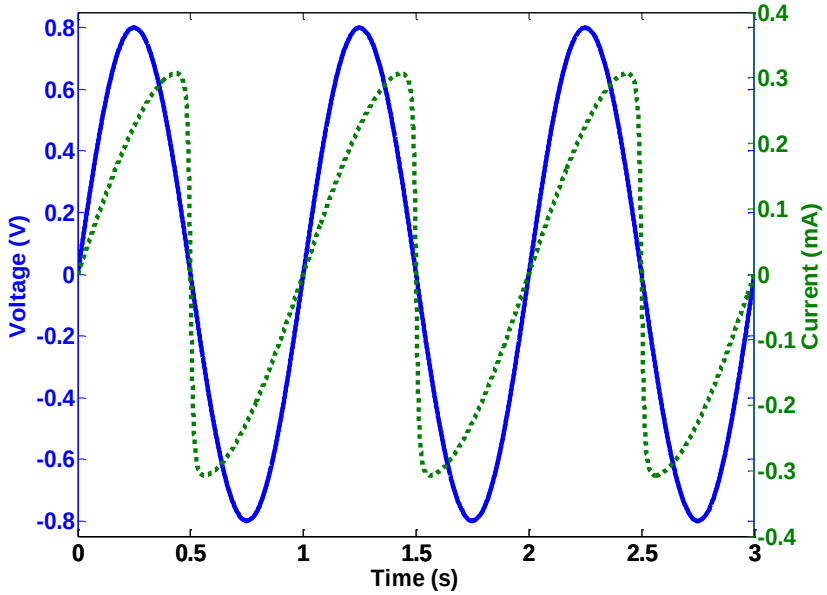

Figure 16. Current behavior for a LDD model with a sinusoidal voltage as input.

Here it is possible to see that the current is skewed with respect to the voltage but there is no a phase difference between them implying that there is no charge stored. Figure 17 is the plot of the hysteresis loop formed by the I-V characteristic at two different frequencies. It is possible to observe a slope difference when the voltage is swapped from 0 to 4 and from 4 to 0, indicating a resistance change. As well, when the frequency increases the resistance change is smaller, thus if the frequency is high enough the memristor will behave as a simple resistor. This phenomenon can be attributed to the small ion average mobility and the integral of the applied voltage in a time range as expressed in Equation 8. (Matlab code in Appendix A) In other words, at high frequency, the ions are slow to respond to the changes in the applied voltage or electric field.

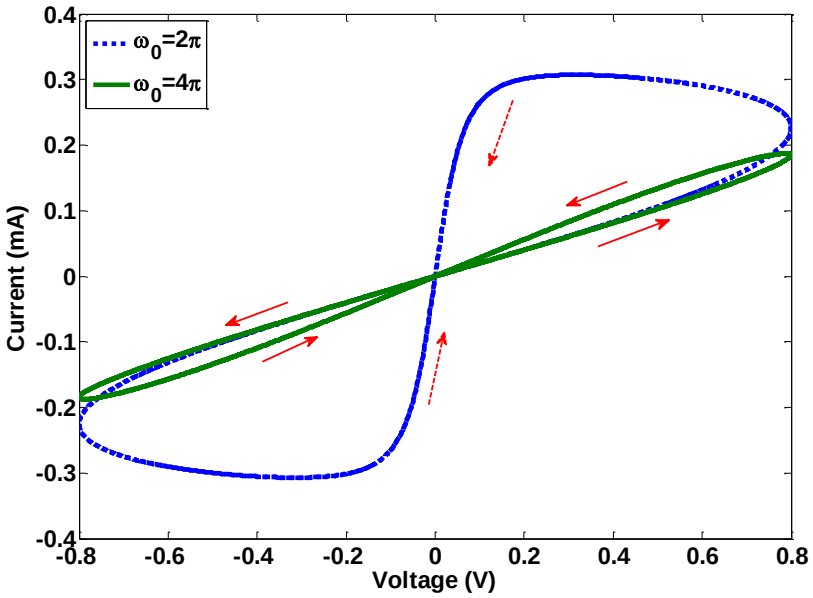

Figure 17. I-V hysteresis loop the LDD memristor model.

2.1.2 Non-Linear dopant drift memristor model

Even though LDD can describe the basic and ideal description of the memristor conductive behavior it does not explain the abrupt resistive switching of the memristor when *w* approaches 0 or *D*, as shown in experimental data in Figure 18. In order to account for abrupt resistive switching, a nonlinear dopant drift model was proposed to describe when the state variable is close to 0 or *D*. This nonlinear ionic transport can be attributed to the high electric field created in nanoscale contact area devices [19] [34].

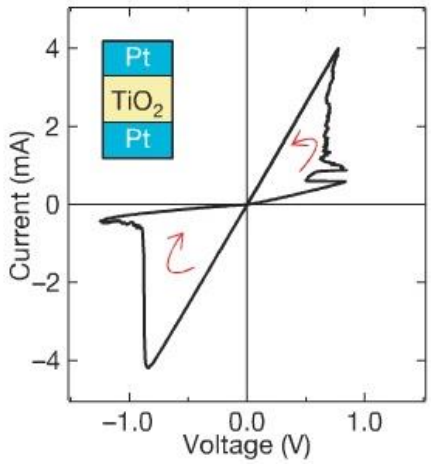

Figure 18. Experimental I-V characteristic for a Pt/TiO2-x/Pt device [48].

In order to overcome and describe this behavior quantitatively, Equation 6 is multiplied by a window function, *f(w)*, as given in Equation 9,

$$\frac{dw(t)}{dt} = \mu_V \frac{\text{Ron}}{\text{D}} i(t) f(w).$$

Equation 9

The purpose of *f(w)* is to take in consideration the nonlinear dopant drift (NDD) behavior. Several window functions have been proposed in order to add flexibility for different memristor structures [20], [49], [50], [51] or to reduce inaccuracy in the solutions [50]. Equation 10 represents the window function introduce by Strukov, *et al* [20],

$$f(w) = \frac{w(D-w)}{D^2}.$$

Equation 10

By combining Equation 9 and Equation 10, the derivative of the state variable with respect time is given by:

$$\frac{dw(t)}{dt} = \mu_V \frac{\text{Ron}}{\text{D}} i(t) \left(\frac{w(D-w)}{D^2} \right).$$

Equation 11

From Equation 11 it is possible to observe that when *w* is equal to 0 or *D* the derivative with respect time goes to zero. Therefore the variable state is constrained to these boundary conditions.

Figure 19 shows the I-V curve for this model at two different frequencies solving for Equation 11 and Equation 5, where the following parameters were used: $v(t) = 0.8\sin(\omega_0 t)$, $\omega_0 = 2\pi$ (blue line), $\omega_0 = 3\pi$ (green line), *Ron* = 100 Ω, *Roff* = 5000 Ω, $\mu_v = 10^{-14}\text{m}^2\text{V}^{-1}\text{s}^{-1}$, D = $10\text{x}10^{-9}$ m, and the initial condition $w(t_0)$ = 1 nm (for NDD $w(t_0) > 0$ to avoid numerical complications). (The Matlab code is shown in Appendix A.)

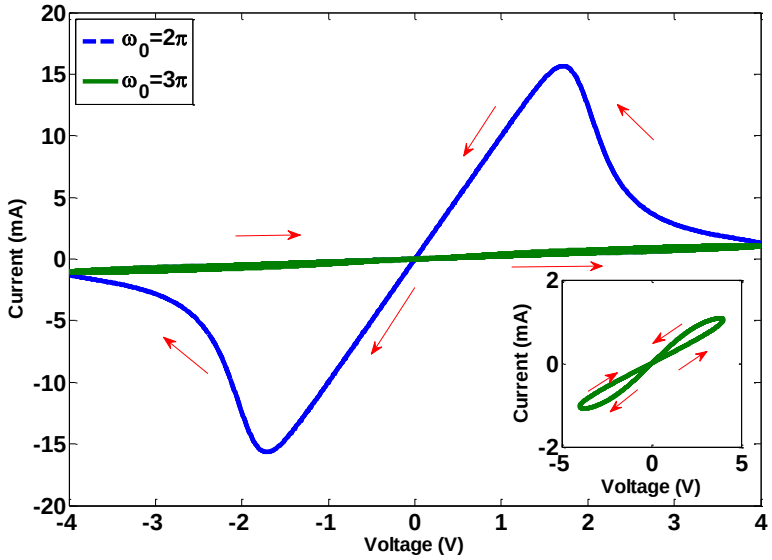

Figure 19. I-V hysteresis loop using the Strukov window NDD memristor model.

Here it is possible to observe that the frequency response is more sensitive for the NDD model than the LDD model. The inset plot is a closer look of the I-V characteristic for $\omega_0 = 3\pi$, where the current is smaller at higher frequencies due to the small change in the memristance. Drift nonlinearity in experimental devices occurs mainly near the boundaries, $w = 0$ and $w = D$, and unfortunately the Strukov window function does not capture this feature well since it describes nonlinearity over the full range of w. In order to overcome this drawback Joglekar and Wolf propose the following window function:

$$f(w) = 1 - \left(\frac{2w}{D} - 1 \right)^{2p},$$

Equation 12

where p is positive integer. Figure 20 shows the window function versus w normalized by D, for different values of p in the function of Equation 11. Here it is possible to observe that the value of function decays faster near the boundaries, (when w is closed to 0 or D) to take in account the abrupt switching in the resistance. If p becomes larger the abrupt change will begin almost at the boundaries. In contrast when p is smaller, the window function will affect the state variable far from the boundaries. The value p can be selected in order to control the nonlinear drift without affecting the full range of w. Also it is shown that the window function proposed by Strukov impacts the full range of w without the flexibility to adjust this condition.

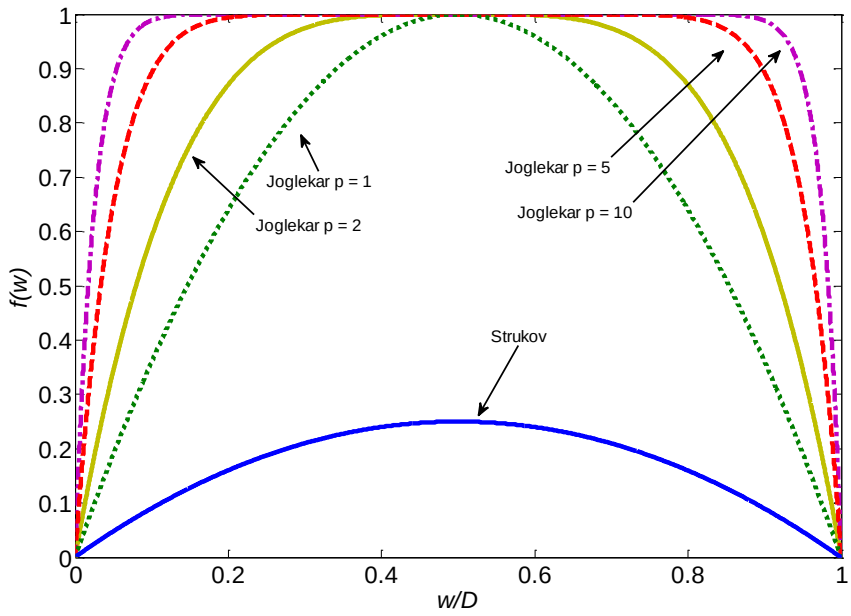

Figure 20. Window function versus w from Strukov and Joglekar for different values of p.

The I-V characteristic for the Joglekar NDD and the LDD model is plotted in Figure 21 a) for comparison purposes. In this chart the solid line (blue line) is the NDD model using the memristor parameters mentioned above but with an input voltage $v(t) = 0.85\sin(\omega_0 t)$, $\omega_0 = 2\pi$, $p = 2$, and the initial condition $w(t_0) = 1$ nm. The dotted line is the LDD model with the same previous conditions. For the NDD case, abrupt changes in the current is predicted corresponding to a saturation of the state variable, w. When w is saturated a resistive switching occurs and the resistance state, either LRS or HRS, is maintained until the polarity of the voltage is changed. This I-V curve matches the experimental data shown in Figure 18. On the other hand, the LDD model cannot maintain the saturation condition without specifying external conditioning functions. Moreover, the input voltage needs to be limited such that the solution for w must be in the 0 to D range taking in account the constraints mentioned in section 2.1.1. Figure 21 b) shows the state variable for the two models normalized by D. It is observed that w is saturated in the NDD but not in the LDD model. The shift is due to different initial condition $w(t_0) = 1$ nm for NDD and $w(t_0) = 0$ nm LDD .

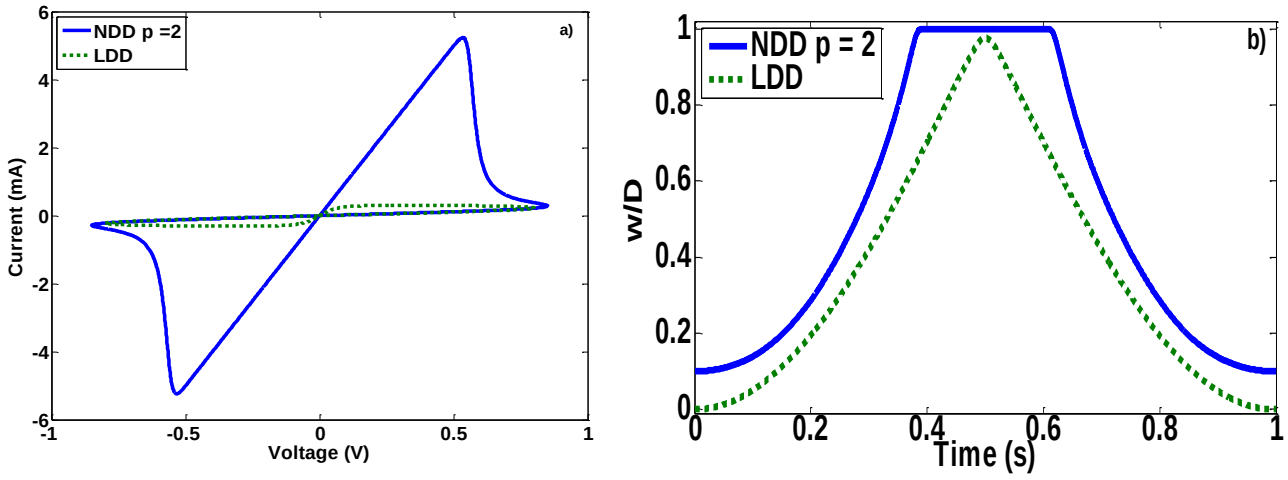

Figure 21. a) I-V characteristic for NDD and LDD model and b) *w/D* for LDD and NDD.

2.1.3 The tunnel barrier mechanism

Even though the LDD and NDD models can describe the memristor behavior qualitatively and quantitatively in some cases, as shown above, the physics behind the filamentary process and memristor current conduction process is still unclear [52]. One of the most promising models is the tunnel barrier mechanism (TBM) which proposes electron tunneling through the oxide film as the current conduction mechanism with an effective barrier width that varies over time [53].

Similar to the LDD and NDD models, the TBM model deals only with the set and reset stages and ignores the forming stage. During the forming stage a nonstoichiometric filament of TiO_{2-x} is formed in the stoichiometric TiO_2 film, as shown in Figure 22. However a gap remains between the filament and the Pt electrode, this gap is the state variable *w*. Therefore tunneling conduction occurs between the filament and the Pt electrode and at the same time this width *w* is changing through time [53]. For this case the device can be represented by an Ohmic resistor in series with a tunnel barrier.

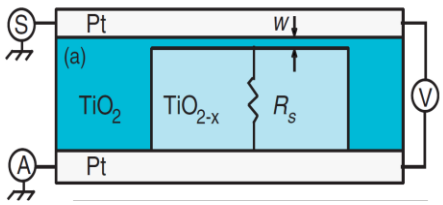

Figure 22. Schematic representation of the tunnel barrier mechanism for a $Pt/TiO_2/Pt$ structure [53].

Based on the electric tunnel effect formulated by Simmons [54], the current conduction is given by:

$$i = \frac{j_0 A}{\Delta w^2}\left(\phi_I e^{-B\sqrt{\phi_I}} - \left(\phi_I + q\left|v_g\right|\right)e^{-B\sqrt{\phi_I + q\left|v_g\right|}}\right),$$

Equation 13

where

$$j_0 = \frac{q}{2\pi h}$$

Equation 14

$$\Delta w = w_2 - w_1$$

Equation 15

$$w_1 = \frac{1.2\lambda w}{\phi_0}$$

Equation 16

$$\phi_I = \phi_0 - q\left|v_g\right|\left(\frac{w_1 + w_2}{w}\right) - \frac{1.15\lambda w}{\Delta w}\ln\left(\frac{w_2\left(w - w_1\right)}{w_1\left(w - w_2\right)}\right)$$

Equation 17

$$B = \frac{4\pi\Delta w\sqrt{2m}}{h}$$

Equation 18

$$w_2 = w_1 + w\left(1 - \frac{9.2\lambda}{3\phi_0 + 4\lambda - 2q\left|v_g\right|}\right)$$

Equation 19

$$\lambda = \frac{q^2 \ln(2)}{8\pi k\varepsilon_0 w}$$

Equation 20

$$\lambda = \frac{q^2 \ln(2)}{8\pi\varepsilon_i w}$$

Equation 21

$$v_g = Vs - iR_s$$

Equation 22

where A is the memristor channel area, q is the electron charge, m is the electron mass, h is Planck's constant, ε_i is the dielectric permittivity, R_s is the conductive channel resistance, ϕ_0 is the initial barrier height, v_g is the voltage across the tunnel barrier, and Vs is the applied voltage at the Pt electrodes.

In this model the state variable dynamic behavior was obtained empirically [53] and it is given by:

$$\frac{dw(t)}{dt} = \begin{cases} f_{off} \sinh\left(\frac{i}{i_{off}}\right) \exp\left[-\exp\left(\frac{w - a_{off}}{w_c} - \frac{|i|}{b}\right) - \frac{w}{w_c}\right] & i > 0 \\ f_{on} \sinh\left(\frac{i}{i_{on}}\right) \exp\left[-\exp\left(-\frac{a_{on} - w}{w_c} - \frac{|i|}{b}\right) - \frac{w}{w_c}\right] & i < 0 \end{cases}$$

Equation 23

where f_{off}, a_{off}, i_{off}, f_{on}, a_{on}, i_{on}, b, and w_c are fitting parameters (values in Ref [53]).

From Equation 13 and Equation 22 it is possible to observe that the current across the circuit cannot be solved explicitly thus an iterative solution is needed. This makes the model less feasible for simulation purposes. It is been shown that equivalent circuits can simulate this model in SPICE [55] [56] [57] although they are less accurate [55]. Additionally, the solution method for this model has not been optimized causing circuit simulations to be highly time consuming.

2.2 PARALLEL PLATE MEMS MODEL

In the previous section the behavior for the memristor was analyzed and different mathematical models were compared. To investigate the potential of integrating the memristor with a MEMS device, the MEMS model needs to be analyzed as well. This section will study the parallel plate MEMS at steady state followed by the dynamic behavior exploring its physical constraints in both cases. Finally, a transient and ac analysis of the MEMS capacitor with a resistor connected in series is performed.

As mentioned in section 1.2.1 one of the most versatile and simplest MEMS structure is the parallel plate. To analyze the behavior of this device a capacitor like structure as shown in Figure 23 will be considered. When a voltage is applied across the bottom and the upper electrode an attractive electrostatic force will move the upper electrode (which is free to move) towards to bottom electrode (which is fixed). However mechanical forces due to the physical characteristic of the MEMS will oppose to this motion, depending on the MEMS design as presented in section 1.2.1. These forces include: the opposition force of the upper electrode to be deformed which is represented by a spring force where the spring constant (k) depends on the electrode material and MEMS design, the inertia force due to the mass of the moving electrode, and the damping force which depends on the media between the two electrodes.

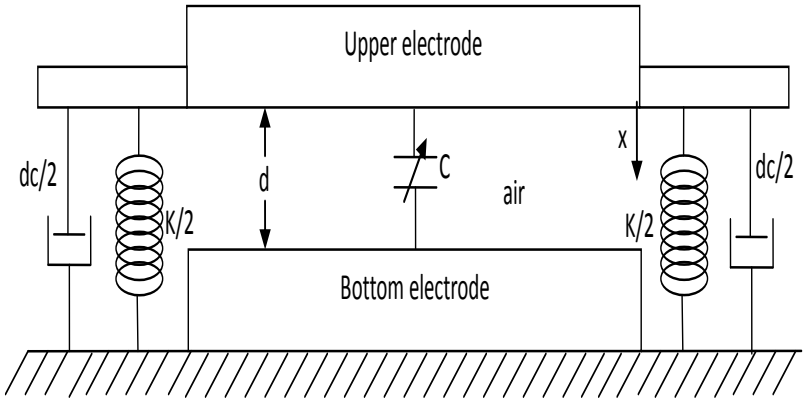

Figure 23. MEMS parallel plate capacitor structure. Where k is the spring constant, d_c is the damping constant, d is the distance between plates, x is the displacement of the upper electrode, and the air is dielectric medium.

Taking in consideration all the forces mentioned above the dynamic behavior of the MEMS is given by the nonlinear Equation 24 [37]. The left side of the equation contains all the mechanical forces and the right side contains the electrostatic force given by Coulomb's law.

$$m\frac{d^2x}{dt^2} + d_c\frac{dx}{dt} + kx = \frac{\varepsilon_0 A V_{MEMS}^2}{2(d-x)^2}.$$

Equation 24

From this equation the displacement of the upper electrode x can be manipulated by applying a voltage, V_{MEMS}.

2.2.1 MEMS steady-state analysis and pull-in voltage

At steady-state the acceleration and the velocity of the upper electrode become zero and Equation 24 will be reduced to Equation 25. At this point a force balance is achieved between the mechanical force (F_s) and the electrostatic force (F_e). F_s tends to return the upper electrode to its initial position and F_e is the attraction force between the electrodes due to the applied voltage.

$$\frac{\varepsilon_0 A V_{MEMS}^2}{2(d-x)^2} - kx = F_e(x) - F_s(x) = 0.$$

Equation 25

F_s is due to the MEMS spring and it has a linear behavior with respect the upper plate position whereas F_e has a parabola-like behavior. This implies that the steady-state can be achieved at two points

as shown in the graphical solution in Figure 24. One point is more stable than the other thus the upper electrode tends to stay at nearest and most stable position [58].

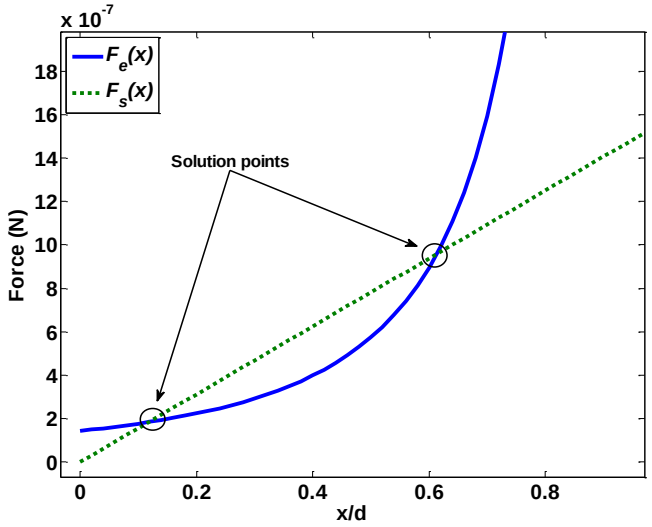

Figure 24. Graphical solution for the forces equilibrium acting in a MEMS at steady state.

A solution point is not considered stable unless the upper electrode can maintain this position even with small force fluctuations. Mathematically it means that a stable position is achieved when the partial derivative of the force with respect to the displacement is less than zero, in other words $\partial F/\partial x_1 < 0$. For that reason Equation 26 is obtained by taking the partial derivative of Equation 25 with respect the displacement:

$$\frac{\varepsilon_0 A V_{MEMS}^2}{(d-x_1)^3} - k < 0.$$

Equation 26

Combining Equation 25 and Equation 26 it is possible to obtain the range where the upper electrode displacement is stable, thus x is limited to $0 < x < \frac{1}{3}d$. If the electrode position has a displacement higher than $\frac{d}{3}$ it cannot be maintained and as consequence the upper electrode will collapse with the bottom electrode. This is a major constraint that limits operation of the upper electrode to one-third of total possible distance between the plates, $d/3$. Hence the maximum voltage that can be applied to avoid a collapse between the electrodes can be obtained by substituting this value into Equation 25. This voltage is known as pull-in voltage and it is given by:

$$V_{pi} = \sqrt{\frac{8kd^3}{27\varepsilon_0 A}}.$$

Equation 27

Although the MEMS device is unstable at displacements greater than *d*/3, it is possible to obtain a correspondent voltage for each position over the total gap under the case of static equilibrium from Equation 25. Figure 25 shows the applied MEMS voltage (normalized with respect to *Vpi*) versus the upper plate position (normalized with respect the total gap). The maximum voltage that can be applied (neglecting the dynamics of the MEMS) is the pull-in voltage. Since the MEMS is unstable above *d*/3, sophisticated control such as closed-looped voltage feedback is required to maintain stable positioning of the upper plate.

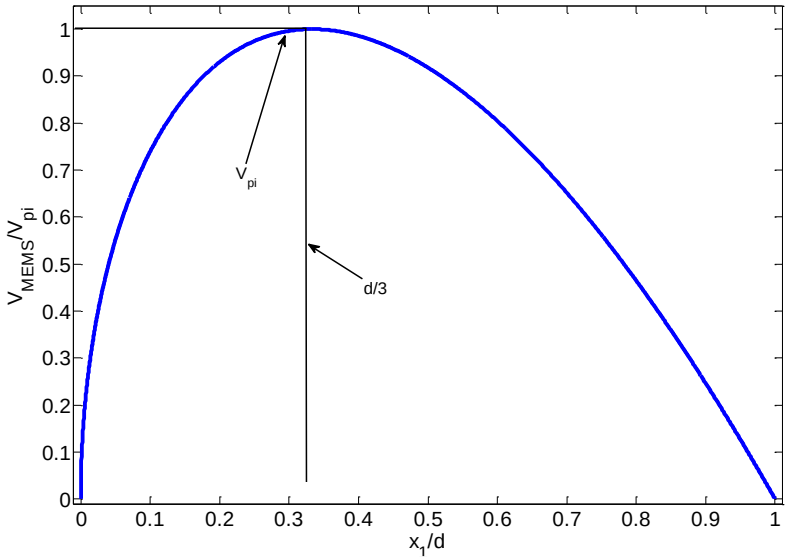

Figure 25. Normalized applied voltage in the MEMS versus normalized upper plate position.

The pull-in voltage depends purely on the MEMS design characteristics, for illustration purposes the following parameters will be assumed: k = 0.3125 N/m, .1 mm^2 < A < 1 mm^2, and 5 µm < d < 500 µm. Therefore the pull-in voltage can be manipulated in wide range by modifying the electrode area or the distance between plates, as shown in Figure 26. Although the voltage can be manipulated, the maximum displacement possible for stable operation is still *d*/3. This limits the range of useful capacitance for the MEMS device.

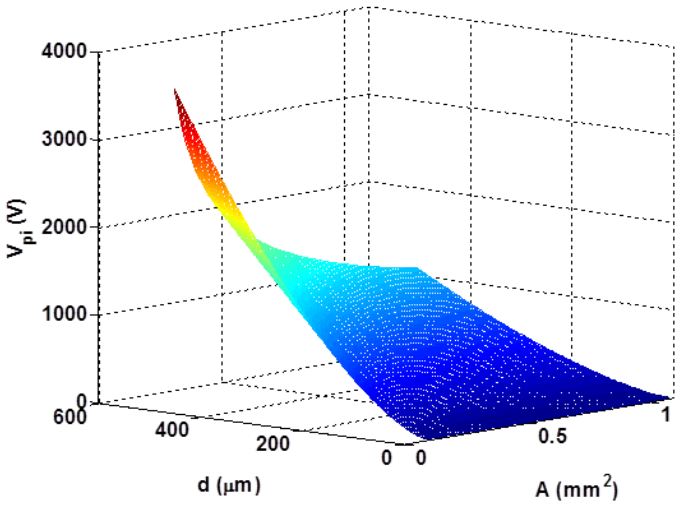

Figure 26. Pull-in voltage range with different plates areas and distance with k = 0.31525 N/m.

2.2.2 MEMS dynamic analysis

Even though a desired upper electrode position can be achieved with an applied voltage it is important to analyze the transient behavior of the MEMS in order to understand its dynamics and consequently the MEMS charge behavior for the integration with the memristor. In this section the transient analysis for the MEMS and the MEMS with a resistor in series is explored using a dc voltage input.

To study the MEMS behavior Equation 24 will be solved for x, however a numerical solution will be employed since a closed form solution cannot be obtained directly. To implement the equation in Matlab it was separated into two parts which allowed the order of the differential equations to be reduced as follows:

$$\frac{dx_1}{dt} = x_2$$

Equation 28

$$\frac{dx_2}{dt} = \frac{\varepsilon_0 A V_{MEMS}^2}{2m(d - x_1)^2} - \frac{d_c}{m} x_2 - \frac{k}{m} x_1$$

Equation 29

where $x_1 = x$ and x_2 is the upper plate velocity. The transient behavior was simulated using the following parameters (provided by the University Autonoma de Ciudad Juarez): ε_0 = 8.854x10^{-12} F/m, d = 5x10^{-6} m, k = 0.3125 N/m, A = (300x10^{-6})^2 m^2, d_c = 5x10^{-5} Kg/s, ρ = 2329 kg/m^3, $m = \rho * A * 2$x10^{-6} kg. For this

case $V_{pi} \approx 3.81$ V. (The Matlab code is listed in Appendix A). The results are shown in Figure 27 using three different input voltages: V_{pi}, 80% of V_{pi}, and 50% of V_{pi}.

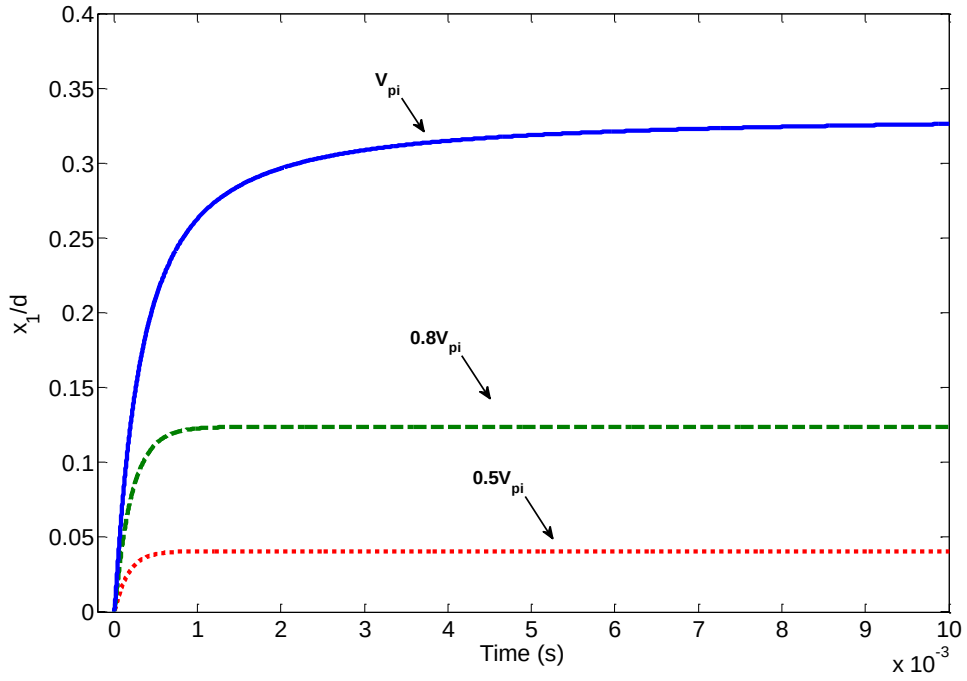

Figure 27. MEMS transient response with different pull-in voltages.

In this case, the transient response is over-damped due to the d_c value. If the damping constant is reduced some oscillations at the MEMS natural frequency will be observed. If this constant is zero the system will oscillate until an external force stops it. The damping condition is very important to take in consideration because if the system is under-damped the maxima step voltage that can be applied in a transient case will be smaller than the *Vpi* given by Equation 27 due to the displacement overshooting $d/3$. In other words, the collapse of the MEMS plates is governed by the dynamics also and not only by the voltage. The collapse between the two plates can be observed using a damping constant of $d_c = 5\text{x}10^{-7}$ Kg/s and applying a step voltage with an amplitude of 92% of the pull-in voltage. Figure 28 shows the transient response of the MEMS under these conditions. The collapse of plates is observed with a voltage smaller than the pull-in voltage due to the MEMS dynamics. Thus the MEMS physical characteristics also limit the operational range.

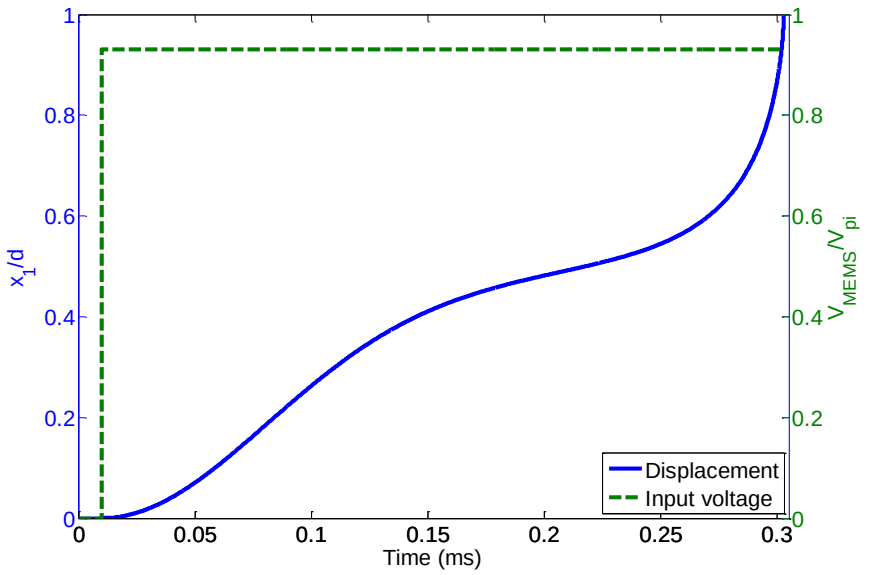

Figure 28. MEMS transient response where the MEMS plates collapse with an applied voltage of 0.92 V_{pi}.

Figure 29 shows the transient behavior of the MEMS with the parameters mentioned above at different damping constants with an applied voltage of $0.8V_{pi}$.

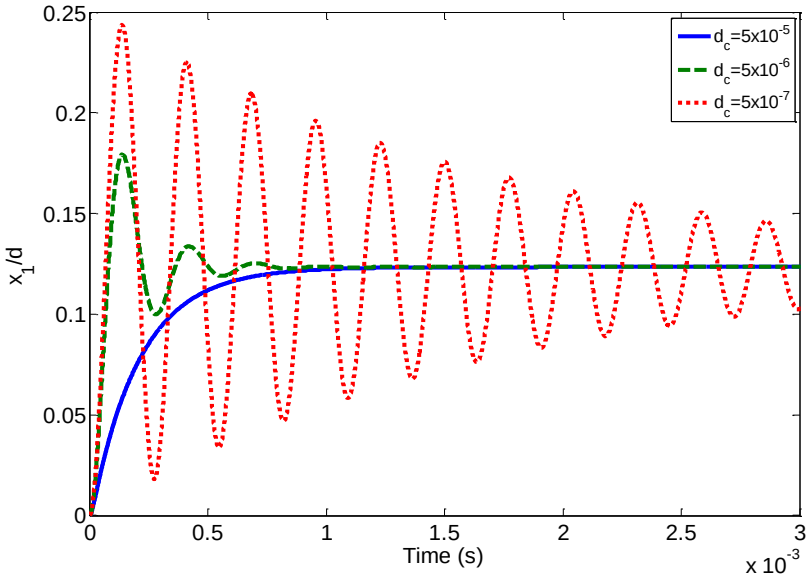

Figure 29. MEMS transient response with different damping values at 0.8 V_{pi}.

The frequency for the oscillations in Figure 29 with damping constant of d_c = 5x10^{-7} Kg/s is the MEMS natural frequency. This frequency defines the MEMS bandwidth, if the device is submitted to higher frequencies the upper plate will not respond properly. In this case it is given by:

$$f_{MEMS} = \frac{\omega_{MEMS}}{2\pi} = \frac{1}{2\pi}\sqrt{\frac{k}{m}} \approx 4.345\,\text{Khz}\,.$$

Equation 30

2.2.3 MEMS ac analysis with a resistor in series

In this section a parallel plate MEMS with a resistor in series will be explored to understand the behavior of the MEMS displacement when it is connected to other circuit elements. The circuit in Figure 30 will be considered where the MEMS is represented by a variable capacitor (varicap).

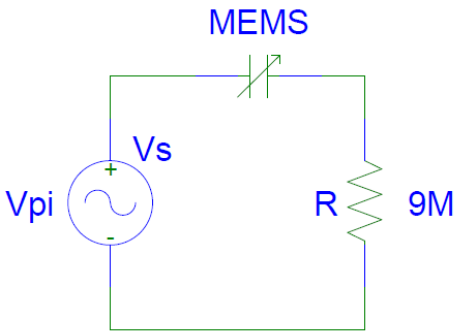

Figure 30. Circuit representation of a MEMS with a resistor in series and an ac power supply.

From Kirchhoff's voltage and current laws the MEMS voltage and current are given by:

$$Vs = V_{MEMS} + V_R$$

Equation 31

$$I_{MEMS} = I_R = \frac{V_R}{R}.$$

Equation 32

The current across the MEMS parallel plate capacitor is given by:

$$I_{MEMS} = \frac{d(CV_{MEMS})}{dt}\,.$$

Equation 33

The MEMS capacitance changes with time since it is a function of the displacement between the bottom and top electrodes. In turn, the top electrode changes over time because it is a function of the

voltage applied to the electrodes, according to Equation 24. Therefore the current through the MEMS capacitor, I_{MEMS}, is given as follows:

$$I_{MEMS} = C\frac{dV_{MEMS}}{dt} + V_{MEMS}\frac{dC}{dt} \quad .$$

Equation 34

The capacitance and the derivative of the capacitance are given by:

$$C = \frac{\varepsilon_0 A}{d - x_1}$$

Equation 35

$$\frac{dC}{dt} = \left(\frac{\varepsilon_0 A}{(d - x_1)^2}\right)\frac{dx_1}{dt} \, .$$

Equation 36

Combining Equation 31-Equation 32, Equation 34-Equation 36, and making $x_2 = \frac{dx_1}{dt}$ the derivative of the MEMS voltage can be obtained as follows:

$$\frac{dV_{MEMS}}{dt} = \left(\frac{Vs - V_{MEMS}}{R}\right)\left(\frac{d - x_1}{\varepsilon_0 A}\right) - \frac{x_2}{d - x_1}V_{MEMS} \, .$$

Equation 37

Hence the Equation 28, Equation 29, and Equation 37 can be solved simultaneously and numerically. The ac behavior was simulated using the MEMS parameters mentioned above with a d_c = 5x10^{-6} Kg/s. As input, a sinusoidal voltage with an amplitude equal to V_{pi} and under a frequency of 4 Hz was used. Also the following initial conditions were employed; $x_1(0) = 0$, $x_2(0) = 0$, which means that the upper MEMS electrode is initially stationary at its equilibrium position, and the initial voltage on the memristor is zero, $V_{MEMS}(0) = 0$.

Figure 31 shows the time response of the MEMS displacement. A smooth motion is observed even when the motion direction is reversed in the range from zero near to $\frac{d}{3}$.

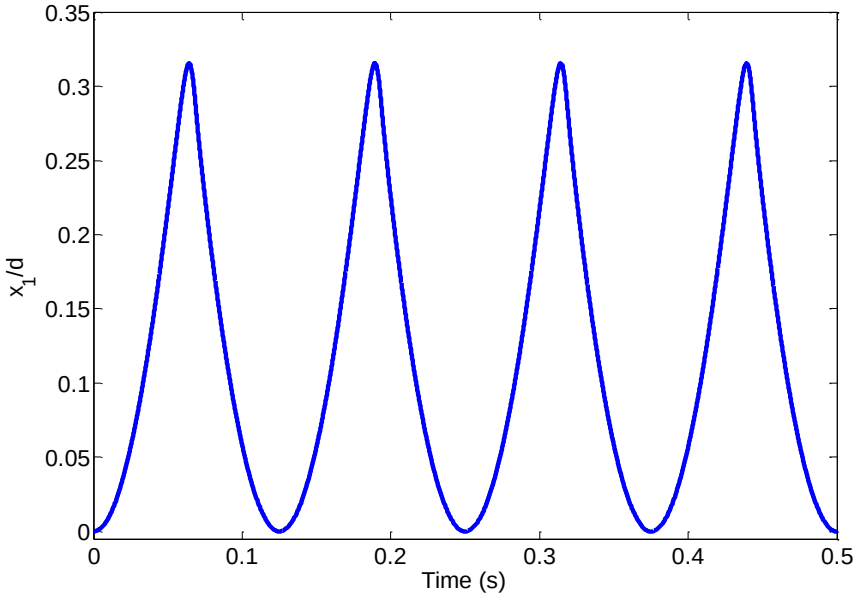

Figure 31. Normilzed MEMS displacement with a resistor in series and an ac input at 4 Hz.

Figure 32 shows the displacement-resistor voltage plot. Here it is possible to observe that the relationship between these two variables is multivalued and nonlinear. Due to this complicated relationship it is not feasible to use the voltage at the resistor to determine the MEMS upper plate position.

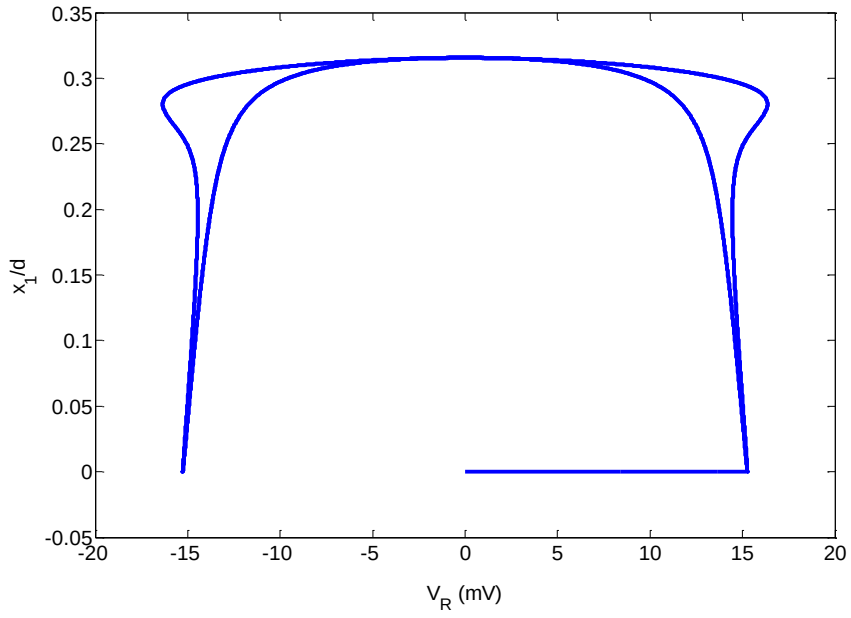

Figure 32. Displacement versus resistor voltage for a MEMS in series with a resistor.

2.2.4 MEMS transient analysis with a resistor in series

Similar to the ac analysis the transient response of the MEMS with a resistor in series will be investigated using the circuit shown in Figure 33.

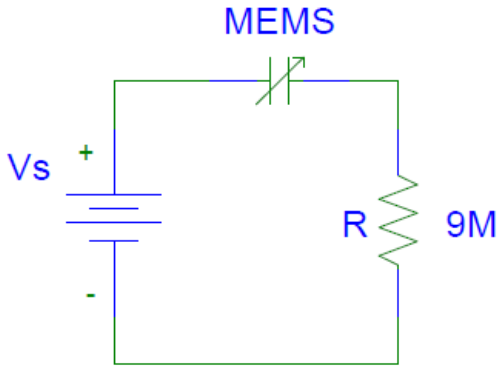

Figure 33. Circuit representation of a MEMS with a resistor in series.

Using the Equation 28, Equation 29, and Equation 37 the transient behavior was simulated for three different R values, 1 Ω, 9 MΩ, and 1000 MΩ. Using the MEMS parameters mentioned above with a d_c = 5x10^{-6} Kg/s and a step voltage $V_s = 0.95V_{pi}$. Also the following initial conditions were employed; $x_1(0) = 0$, $x_2(0) = 0$, and the initial voltage on the memristor is zero, $V_{MEMS}(0) = 0$ (The Matlab code is listed in Appendix A).

The MEMS voltage is plotted in Figure 34 a). With the 1 Ω and 9 MΩ resistors V_{MEMS} transient response is closed to V_s. As the series resistor is larger, 1000 MΩ, V_{MEMS} becomes over-damped. Figure 34 b) shows the voltage across the series resistor, V_R. When the upper plate reaches steady state V_R tends to zero due to the MEMS capacitor behaving as an open circuit. The over-damped response is also observed with the series resistor of 1000 MΩ. The circuit current is plotted in Figure 34 c), the time response is under-damped for the 1 Ω and the 9 MΩ resistors due to the oscillation of the MEMS plate, whereas an over-damped behavior is observed with the 1000 MΩ resistor. The MEMS displacement has a similar transient behavior to the current, under-damped for the 1 Ω and the 9 MΩ resistors and over-damped for the 1000 MΩ resistor. As depicted in Figure 34 d).

The resistor in series with the MEMS affects the MEMS reaction time, thus the resistor acts as a damping force by controlling the amount of current in the circuit. In order to have a significant impact

in the MEMS dynamics the resistor in series has to be in the order of GΩ. If a resistor of 9 MΩ is placed the MEMS dynamics is practically the same as a resistor of 1 Ω.

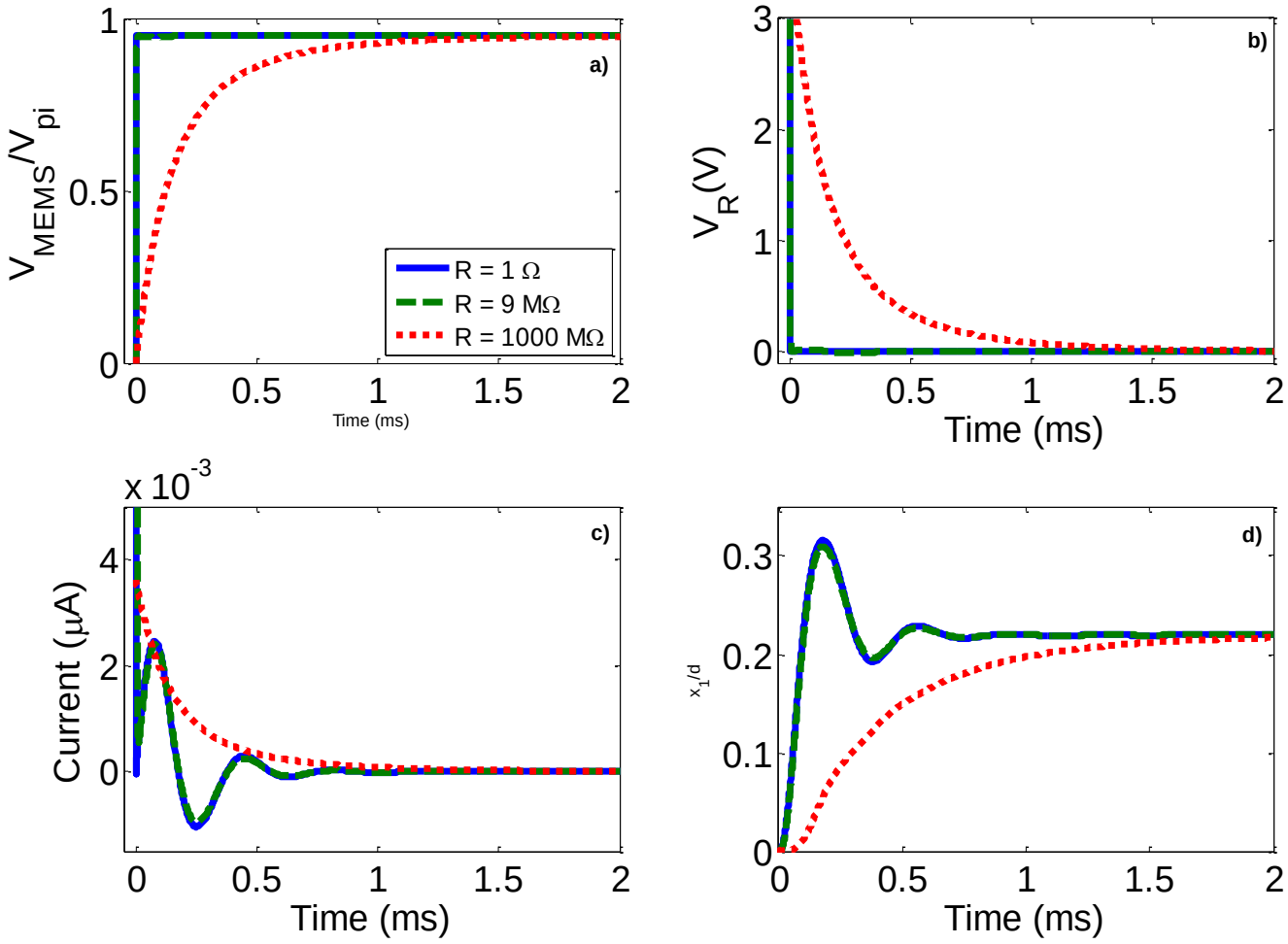

Figure 34. MEMS behavior with different series resistor values. a) MEMS voltage, b) resistor voltage, c) circuit current, and d) normalized MEMS displacement.

3 Direct Integration of the Memristor with a MEMS Capacitor

While the general concept of integrating a memristor with a MEMS device was introduced by Zubia *et al.* [15], the actual details of the integration were not specified. However in Ref [59] the memristor-MEMS series and parallel configurations were investigated for an ac voltage input, and showed that the memristance and the MEMS displacement can be correlated. In this section, the memristor-MEMS series configuration is analyzed both ac and dc input voltages to explore the MEMS mechanical movement (capacitance variation) as well as the memristor behavior.

Even though parallel configuration has shown some correlation between the MEMS motion and the memristance the devices are not strongly coupled [59]. The parameters for each device can be tuned separately in this configuration in order to correlate the memristance and the MEMS displacement with an ac input but not for a dc input. Since the devices can be treated separately, this implies that there is no interaction or real correlation between the main characteristics of the devices, such as the current that flows through them. Due to this drawback, the parallel configuration is not considered further.

3.1 Memristor and MEMS in a series circuit with ac voltage input

In this section a memristor in series with a parallel plate MEMS will be analyzed with an ac input voltage, similar to ref [59] as shown in Figure 35.

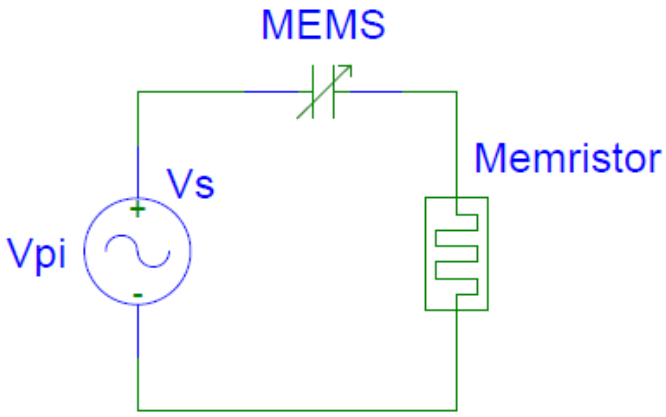

Figure 35. Circuit representation of a memristor and a MEMS series with an ac input.

Similar to section 2.2.1, Kirchhoff's voltage and current laws are used to derive the following expressions:

$$Vs = V_{MEMS} + V_{RM}$$

Equation 38

$$I_{MEMS} = I_{RM} = \frac{V_{RM}}{M(w)}$$

Equation 39

where V_{RM} and I_{RM} are the memristor voltage and current, respectively. $M(w)$ is the memristance as a function of the state variable, w.

The goal of correlating the MEMS displacement with the memristance [59] can be used to select an appropriate model and operating range for the memristance from those presented in in section 2.1. Since the MEMS displacement is an analog value, the linear-dopant-drift (LDD) is a suitable model since the memristance, $M(w)$, is also analog provided that w does not reach a boundary. Care must be taken to avoid operating the memristor near the boundaries, $w = 0$ and $w = D$. Otherwise, if w is allowed to reach a boundary, the value of $M(w)$ will saturate at either R_{off} or R_{on} as shown in section 2.1.2 and the correlation between the MEMS displacement and the memristance will be lost. Therefore the LDD memristance model is selected as given by Equation 7 and the circuit current can be expressed by,

$$I_{RM} = \frac{V_{RM}}{Ron\frac{w(t)}{D} + Roff\left(1 - \frac{w(t)}{D}\right)}.$$

Equation 40

Following the same procedure as in section 2.2.1, the derivative of the voltage with respect time is obtained by combining Equation 38, Equation 39, Equation 34, and Equation 36, and making $x_2 = \frac{dx_1}{dt}$ and is given by,

$$\frac{dV_{MEMS}}{dt} = \frac{(Vs - V_{MEMS})(d - x_1)}{\varepsilon_0 AM(w,t)} - \frac{V_{MEMS}x_2}{(d - x_1)}.$$

Equation 41

The memristor state variable can be obtained by combining Equation 6 and Equation 38 and is expressed as follows,

$$\frac{dw(t)}{dt} = Ron\mu_V \frac{(Vs - V_{MEMS})}{DM(w,t)}.$$

Equation 42

Recalling the mathematical expressions that describe this circuit and substituting Equation 7 into Equation 41 and Equation 42 the following set of equations is obtained:

$$\frac{dx_1}{dt} = x_2$$

Equation 43

$$\frac{dx_2}{dt} = \frac{\varepsilon_0 A V_{MEMS}^2}{2m(d - x_1)^2} - \frac{d_c}{m} x_2 - \frac{k}{m} x_1$$

Equation 44

$$\frac{dV_{MEMS}}{dt} = \frac{(Vs - V_{MEMS})(d - x_1)}{\varepsilon_0 A\left(Ron\frac{w(t)}{D} + Roff\left(1 - \frac{w(t)}{D}\right)\right)} - \frac{V_{MEMS} x_2}{(d - x_1)}$$

Equation 45

$$\frac{dw(t)}{dt} = Ron\mu_V \frac{(Vs - V_{MEMS})}{D\left(Ron\frac{w(t)}{D} + Roff\left(1 - \frac{w(t)}{D}\right)\right)}.$$

Equation 46

These equations can be solved simultaneously and numerically using the function ode23s from MATLAB, where *Vs* is a sinusoidal input voltage given by,

$$Vs = \sqrt{\frac{8kd^3}{27A\varepsilon_0}}(\sin(\omega t)).$$

Equation 47

The maximum amplitude of the input voltage was set to the MEMS pull-in voltage in order to avoid the unstable situation where the top electrode moves continuously towards the bottom electrode until making contact with it as mentioned in section 2.2.

For the following analysis, the parameters for each device are the same as previous given and repeated here for convenience. For the parallel plate MEMS the parameters are: $\varepsilon_0 = 8.854\text{x}10^{-12}$ F/m, $d = 5\text{x}10^{-6}$ kg/s, $k = 0.3125$ N/m, $A = (300\text{x}10^{-6})^2$ m^2, $dc = 5\text{x}10^{-6}$, $\rho = 2329$ kg/m^3, $m = \rho * A * h$, where h is the upper plate thickness and for this case it is equal to $2\text{x}10^{-6}$ m. The parameters for the memristor are: $Ron = 100\ \Omega$, $Roff = 5000\ \Omega$, $\mu_v = 10^{-14}\text{m}^2\text{V}^{-1}\text{s}^{-1}$, and $D = 10\text{x}10^{-9}$ m. Additionally, the following initial conditions are used; $x_1(0) = 0$, $x_2(0) = 0$, which means that the upper MEMS electrode is initially stationary and without any displacement, the initial voltage on the memristor is zero, $V_{MEMS}(0) = 0$, and

the doped and undoped regions have the same length initially. In other words, the state variable initial condition is $w(0) = D/2$. This implies that the initial memristance is $M(0) = 2{,}550$ Ohms.

Figure 36 shows the behavior of the memristance M (dotted line) and the normalized displacement $x_{1/d}$ (solid line) of the MEMS upper electrode through time applying a sinusoidal voltage with a frequency $f = 4$ Hz. Here, it is possible to observe that the frequency of the displacement is twice the memristance however both are in the same phase. The doubling of the frequency can be attributed to the V_{MEMS}^2 dependence of the displacement on the voltage which has a rectifying effect. In contrast, the frequency of the memristance, M, is the same as the frequency of the voltage. A positive voltage will deplete the oxide in the undoped region and reduce M while a negative voltage will oxidize it and consequently increase M .

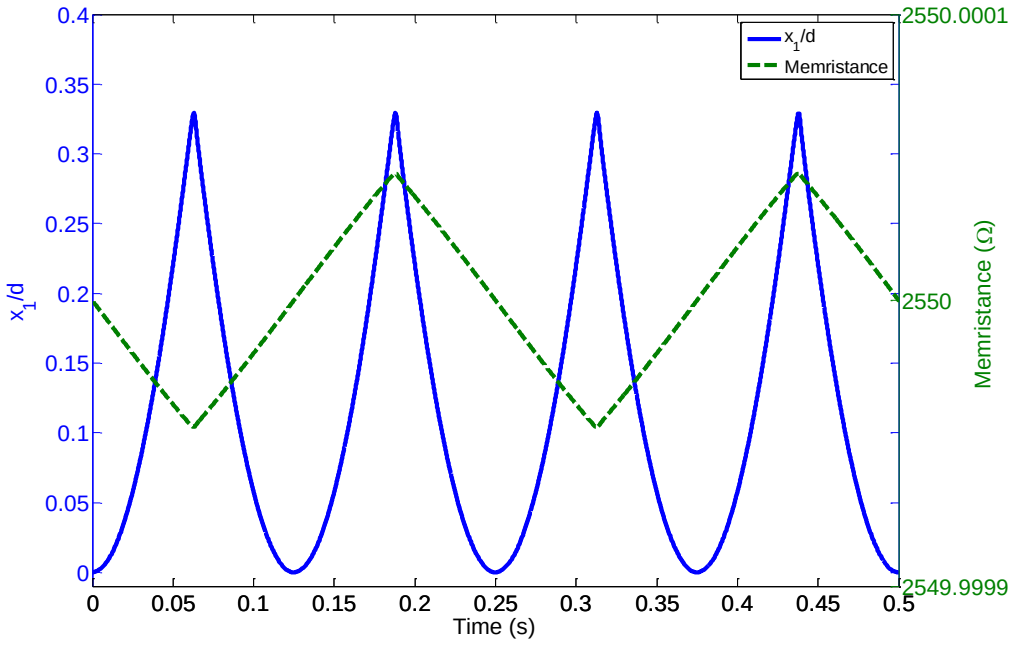

Figure 36. Memristance and normalized MEMS displacement time response with a input voltage with f = 4Hz.

This results in a parabolic form for the displacement-memristance curve as shown in Figure 37. The parabolic relationship implies that in principle, the memristance can be used to monitor the displacement of the MEMS upper plate in real-time. Moreover, since the memristor device has intrinsic memory, it may be possible to store the MEMS plate position in the form of memristance.

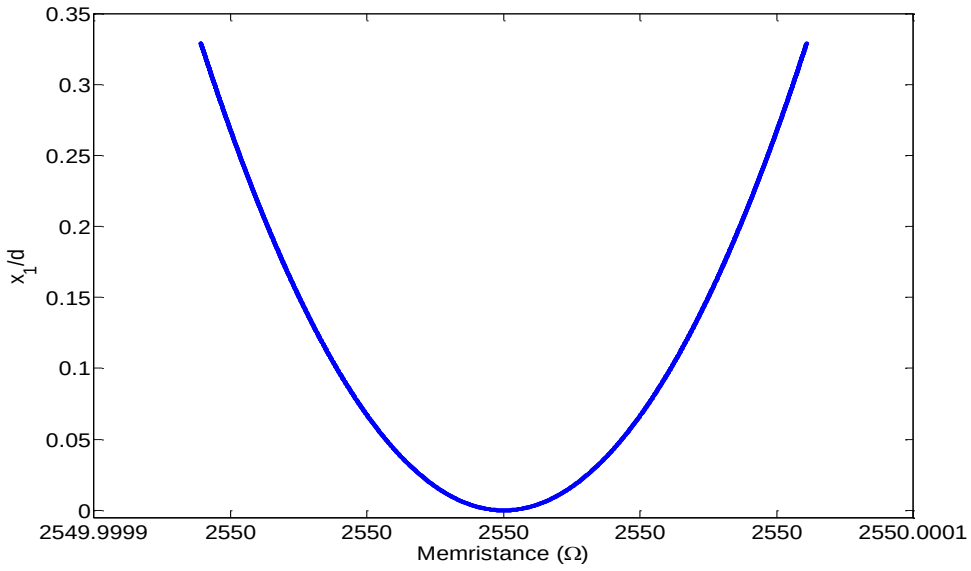

Figure 37. Normalized MEMS displacement-memristance with an input voltage with f = 4Hz.

Even though there is a relationship between the memristance and the MEMS displacement at low frequencies this is not the case for high frequencies, as plotted in Figure 38. For this case a sinusoidal voltage input with a frequency of 4 KHz was applied to the circuit using the same parameters as above for both devices.

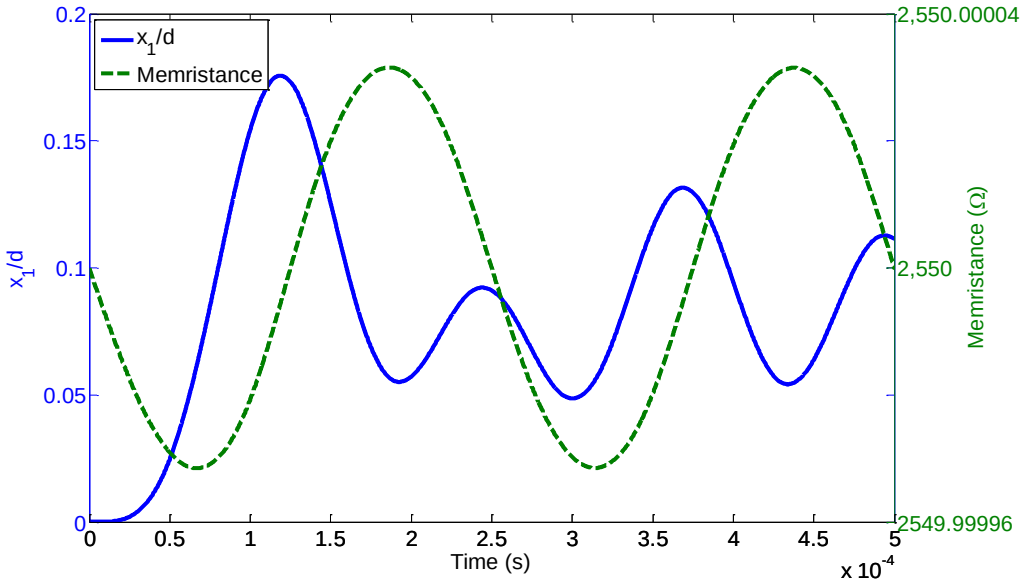

Figure 38. Memristance and MEMS displacement time response with a input voltage with f = 4 KHz.

In this case it is possible to observe that the devices are oscillating at different frequencies. The resistance of the memristor is oscillating similar to the input frequency whereas the MEMS motion is oscillating faster and with a phase shift. Even though the amplitude of the input voltage is equal to the pull-in voltage the MEMS displacement is not reaching the one third of the total plates separation, this can be attributed to the input frequency near to the MEMS natural frequency where the MEMS will not response due to physical limitations. This results in a time-variant hysteresis loop between the MEMS displacement and the memristance as shown in Figure 39.

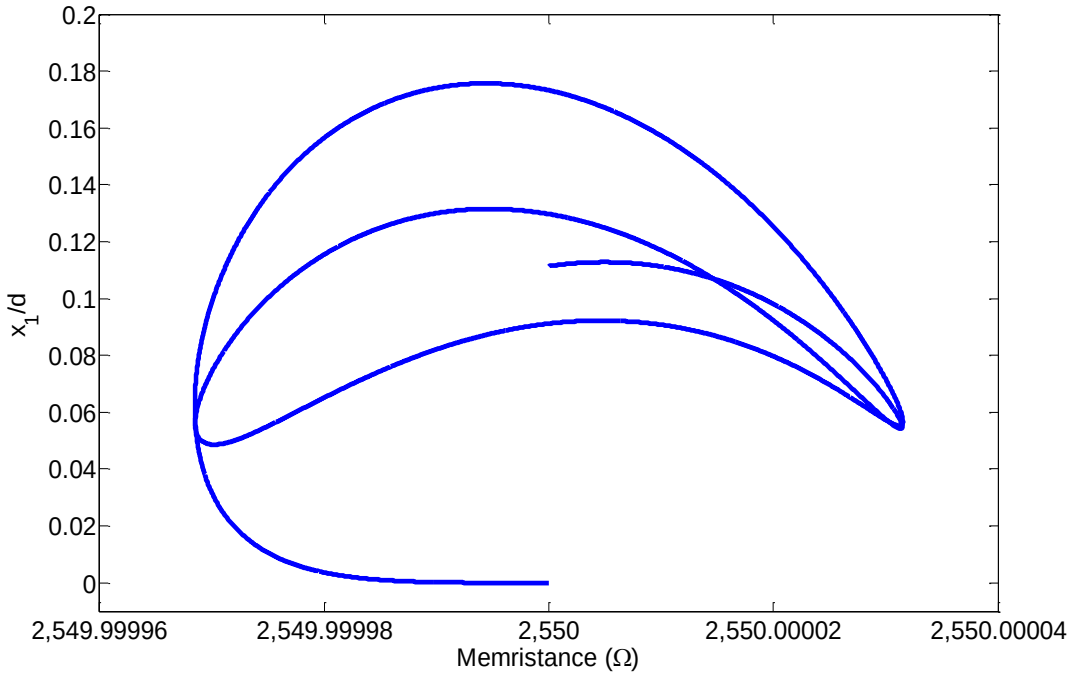

Figure 39. Normalized MEMS displacement-memristance with an input voltage with f = 4 KHz.

3.2 MEMRISTOR AND MEMS IN SERIES CIRCUIT: TRANSIENT ANALYSIS

In this section the transient response of the memristance and the MEMS displacement will be analyzed to investigate the relationship between these two parameters. Similar to the previous section the circuit in Figure 40 will be considered but with a dc input.

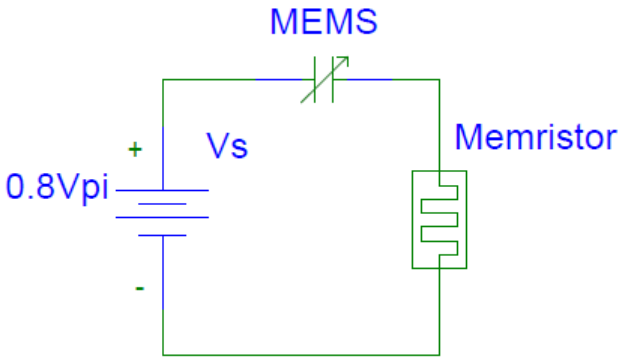

Figure 40. Circuit representation of a memristor and a MEMS in series with a dc input.

For this case the parameters of the devices will be the same as in section 3.1 but with a step input voltage of amplitude $0.8V_{pi}$ in order to avoid overshooting the MEMS critical displacement. To analyze this circuit, Equation 43 to 46 were solved with the ode23s function from Matlab.

Figure 41 shows the time response for the normalized MEMS displacement (solid line) and the memristance change with respect to the initial condition ($M(0)$ = 2,550 Ohms). Here it is possible to observe that the MEMS upper plate oscillations have the same frequency that the memristance change indicating a coupling between the memristor and the MEMS.

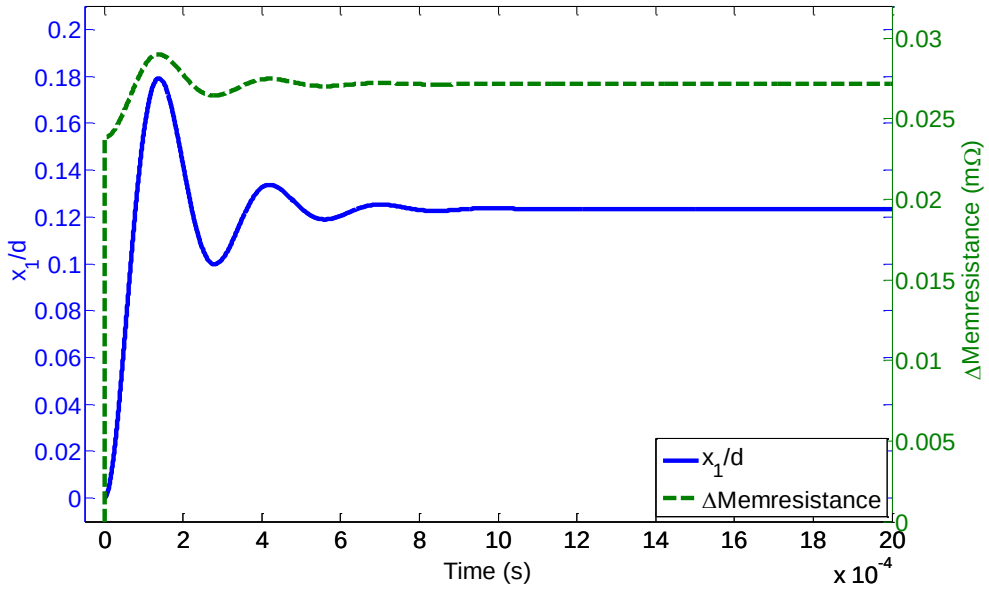

Figure 41. Memristance and normalized MEMS displacement time response with a step input voltage.

A spike in the memristance at time $t = 0$ there is observed, this can be attributed to the abrupt voltage change when the step function is applied. In other words, the voltage observed by the memristor will change suddenly from zero to the step amplitude, as shown in Figure 42. The memristor will change its resistance in response to this transient event.

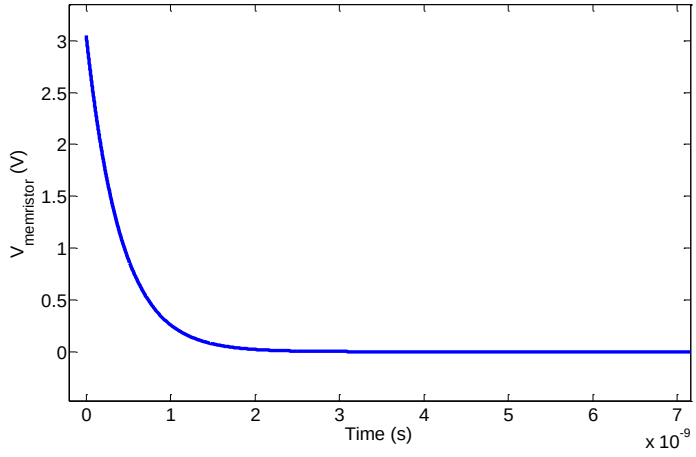

Figure 42. Memristor voltage for a series circuit with a MEMS with a step function input.

This initial behavior can be also observed in Figure 43, which is a plot of the normalized MEMS displacement versus the change in the memristance. After this transition there is a correlation between these two parameters, similar to the ac case for the dc case there is a relationship as well between the upper plate displacement and the change of the memristance. This relationship can be employed to measure the MEMS displacement in form of resistance change, or memristance modulation. Furthermore the MEMS dynamics can be store in non-volatile memory.

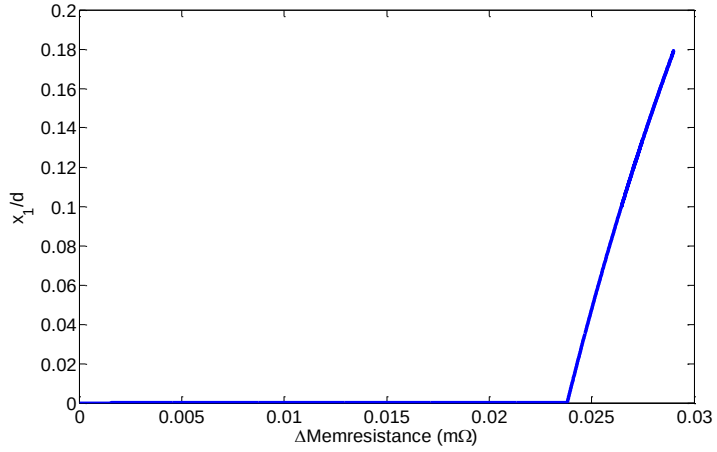

Figure 43. Normalized MEMS displacement-memristance with a step input voltage.

3.3 COUPLING DEFICIENCIES IN THE MEMRISTOR – MEMS SERIES CIRCUIT

In the series configuration for the memristor and the MEMS it is possible to observe that the displacement can be a function of the memristance with either dc voltage or ac voltage at low frequencies giving the possibility of representing the upper electrode position using the memristance instead of capacitance. In this configuration the change in the resistance is insignificant and physically impractical to measure.

Analyzing the series circuit, with an ac input voltage, it is possible to observe that the voltage at the memristor (V_{RM}) is very small at low frequencies as shown in Figure 44, where the dotted green line represents the memristor voltage from the analysis in section 3.1, using an input voltage frequency of 4 Hz. It is also possible to observe that the maximum difference is ~0.12 μV. This can be attributed to the capacitor-like behavior of the MEMS which has very high impedance at low frequency. This chart also shows that an abrupt change in V_{RM} occurs when the MEMS upper plate displacement (solid line) changes its direction of motion.

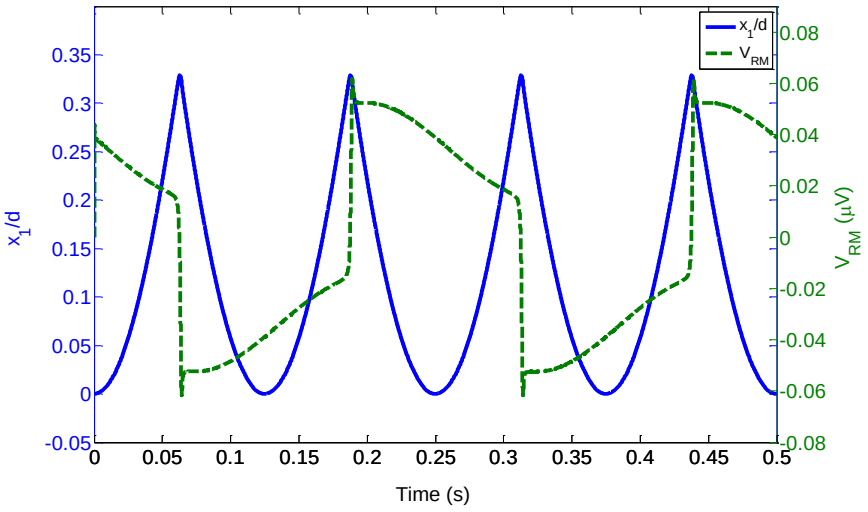

Figure 44. Solid line represents the normalized MEMS displacement and dotted line represent the voltage that is applied to the memristor in a series circuit under a sinusoidal input with f = 4Hz.

At high frequencies the voltage across to the memristor, V_{RM}, is higher as shown by the dotted line in Figure 45**Error! Reference source not found.**. This can be attributed to the MEMS capacitor having relatively lower impedance at high frequencies. In this case there is no abrupt change in either the MEMS displacement (solid line) direction or V_{RM}.

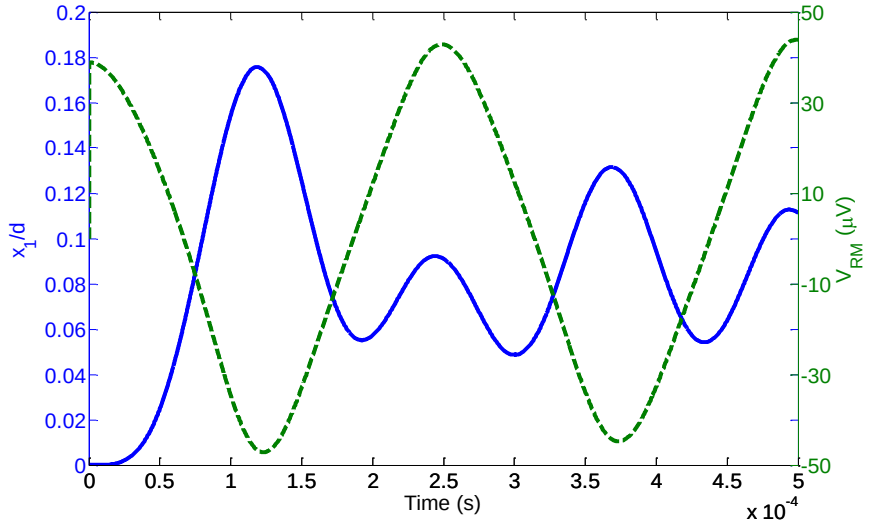

Figure 45. Solid line represents the normalized MEMS displacement and dotted line represent the voltage that is applied to the memristor in a series circuit under a sinusoidal input with f = 4 KHz.

The current that passes through the series circuit is very small at low frequency. Figure 46 shows the current passing through the MEMS and the memristor indicated by the dotted green line. The maximum current is approximately 0.03 nA. Similar to V_{RM}, I_{RM} also shows an abrupt change which occurs when the MEMS plate change its direction of motion or when the applied voltage changes its slope from positive to negative. Furthermore, the current is shifted 90˚ from the input voltage due to capacitive behavior of the MEMS.

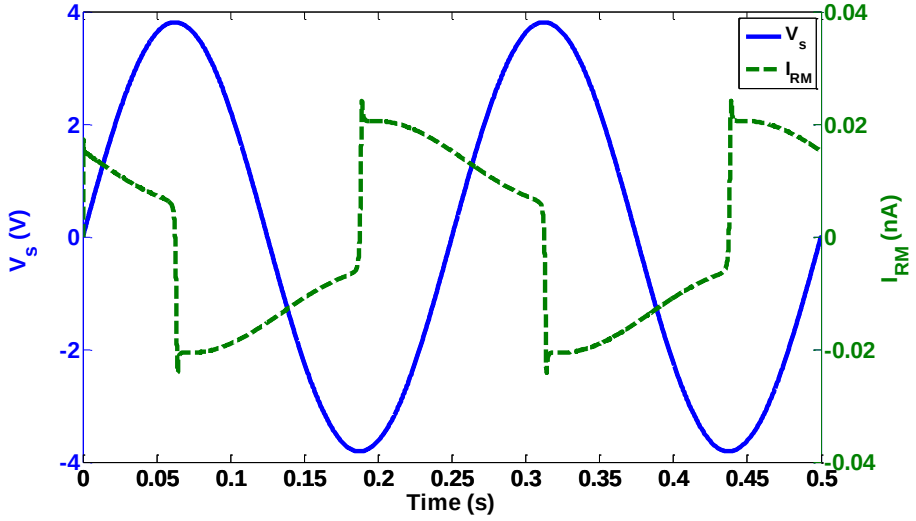

Figure 46. Solid line represents the applied voltage by the power supply, dotted line represent the current through the series circuit under a sinusoidal input with f = 4Hz.

In contrast, the current is larger at high frequency as shown in Figure 47. The maximum is ~20 nA (dotted line) and shifted 90˚ from the input voltage due to the capacitive behavior of the MEMS. Although V_{RM} and I_{RM} are larger at higher frequency, this is off-set with a smaller change in memristance due to the low ion mobility; at high frequencies the memristors behaves as a normal resistor as shown in section 2.1.1.

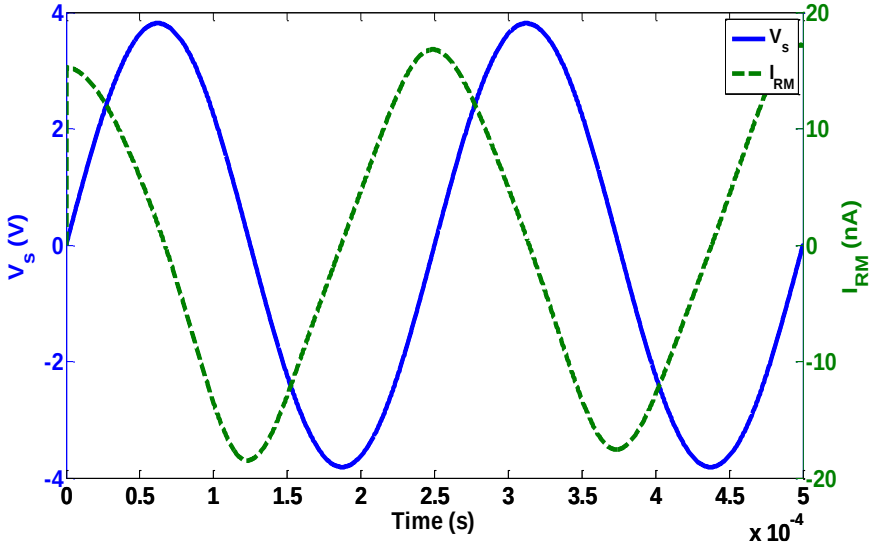

Figure 47. Solid line represents the applied voltage by the power supply, dotted line represent the current through the series circuit under a sinusoidal input with $f = 4$ KHz.

3.4 MEMRISTOR AND MEMS SERIES CIRCUIT CONCLUSIONS

The coupling of memristors and MEMS in a series circuit was analyzed in this chapter. The correlation between the memristance and the displacement is derived from the common charge that passes through both devices in the circuit. The charge in the MEMS can be obtained from Equation 35

$$q = \frac{\varepsilon_0 A}{d - x_1} V_{MEMS}$$

Equation 48

the memristance as a function of the charge is given by,

$$M = \left(\frac{Ron^2 \mu_V}{D^2} - \frac{RonRoff \mu_V}{D^2} \right) q + Roff$$

Equation 49

combining Equation 24, **Error! Reference source not found.**, and **Error! Reference source not found.** the memristance can be a function of the MEMS dynamics given by,

$$M = \sqrt{2\varepsilon_0 A}\mu_V Ron\left(Ron - Roff\right)\left(m\frac{d^2x}{dt^2} + d_c\frac{dx}{dt} + kx\right)^{1/2}.$$

Equation 50

From this equation it is possible to observe a quadratic relationship between the MEMS displacement and the memristance. This quadratic relationship creates the possibility of representing the upper electrode position in the form of memristance instead of capacitance. Additionally, there is also the possibility of storing the displacement state due to the intrinsic memory of memristors. This makes the memristor an excellent element to integrate with MEMS actuators to monitor and remember the position of the upper electrode.

The analysis of the quadratic relationship showed that the devices correlated in a time invariant fashion only for dc and low-frequency ac input voltages. For these cases the change in the memristance is impractically small due to the large voltage drop across the MEMS capacitor. At high frequencies the correlation is a complex time-variant multi-valued function. The memristance modulation is also small at high frequency; in this case it is due to the slow ion mobility in the memristor.

Consequently, the circuit current or the memristor voltage for the series circuit needs to be amplified in order to obtain a larger memristance modulation. In order to overcome this drawback different application stages are proposed in the following section.

4 Amplified Memristor-MEMS Coupling

In the previous section it was shown the memristance change can be used to measure the MEMS displacement. However the memristance change is impractical due to the small circuit current and large voltage drop across the MEMS attributed to the capacitor like behavior of the MEMS. Therefore an amplification stage between the MEMS and the memristor is needed. In this section the integration of the memristor with the MEMS is analyzed using three different kinds of amplifiers to couple the devices. The three types of amplifiers used are: the bipolar junction transistor (BJT) based amplifier, the metal-oxide-semiconductor field-effect transistor (MOSFET) based amplifier, and the operational amplifier (Op Amp). For each amplification case the circuit analysis is divided in three stages; the input, amplifier, and load stages. The input stage is modeled by a MEMS capacitor in series with a resistor. The analysis presented in in section 2.2.2 shows that the series resistor needs to have a very large value in order to affect the MEMS behavior. The amplification stage includes all the circuit elements needed (resistor, capacitor, and transistors), to amplify the voltage across the resistor in series with the MEMS capacitor. The load stage consists of the memristor that will receive the amplified current or voltage from the amplifier stage.

4.1 MEMS-BJT-MEMRISTOR ANALYSIS

The first amplification stage to analyze is the bipolar junction transistor (BJT) amplifier. The BJT transistor is extensively used in high-speed circuits, analog circuit, and power applications [60]. This semiconductor device has three jointed regions where two of them are negatively doped (n-type) and the other one is positively doped (p-type) or vice versa, forming npn or pnp transistor. The BJT is a three terminal device: the base (B), the collector (C), and the emitter (E), as shown in the npn transistor cross section Figure 48 a).

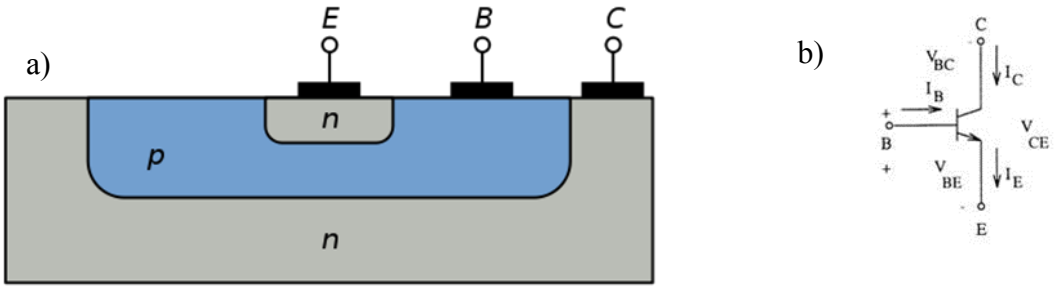

Figure 48. a) Crosse secctional illustration for a npn BJT transistor [61] b) npn BJT circuit symbol.

There are three main operation modes for the BJT transistor depending on the bias configuration: the active mode, where the emitter-base junction is forward-biased and the collector-base junction is reverse-biased. This mode is commonly used for amplifier circuits where the largest amplification for current and voltage is obtained. In the saturation mode both junction are forward-biased hence the ratio of the voltage to the current is small; this mode is used where the transistor is used as a switch, and it is at ON position. The cutoff mode is when both junctions are reverse-biased creating very small currents making this mode the OFF switch position, as opposite to saturation mode. Figure 49 shows the I-V characteristic of a BJT and the different operations modes at different base currents, where I_C is the collector current and the V_{CE} is the collector-emitter voltage [62].

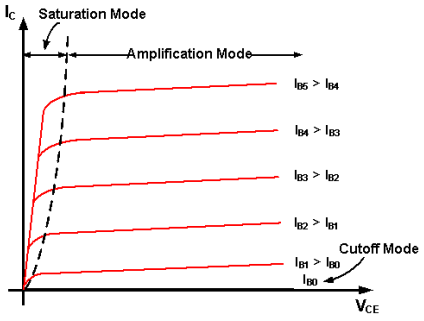

Figure 49. BJT current characteristc I_C-V_{CE} at different base current [63].

The main current conduction mechanism is the diffusion of electrons and holes between the emitter and the collector. Elbers-Moll mathematical model describes this mechanism, for a transistor operating in the active mode it can be approximated as follows:

$$I_C = I_S \exp\left(\frac{V_{BE}}{V_T}\right)$$

Equation 51

$$I_B = \frac{I_C}{\beta}$$

Equation 52

where I_c is the collector current, I_s is the reverse saturation current, V_{BE} is the base-emitter voltage, V_T is the thermal voltage (which is approximately 26 mV at 300 K), I_B is the base current, and β is the current gain which depends on some physical parameters of the transistor.

The emitter current can be obtained using Kirchhoff's current law from the electric symbol in Figure 48 b), and it is given by Equation 53. $I_E \approx I_C$ if the current gain is much bigger than 1.

$$I_E = I_C - I_B = I_C\left(\frac{1-\beta}{\beta}\right)$$

Equation 53

There are different circuit configurations for a BJT amplifier and each case can have different amplification gain as well different impedance input, as shown in Table 1 [64]. For the purpose of the integration of the memristor and the MEMS, the configuration with higher amplification gain and higher impedance input is preferred.

Table 1 Summary of BJT circuit configurations

Configuration	Circuit	Input impedance Zi	Output impedance Zo	Voltage gain Av	Current gain Ai
Common emitter	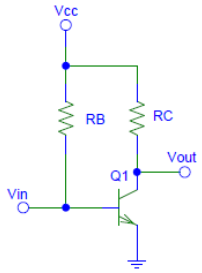	Medium (1 KΩ) $=\beta r_p$	Medium (1 KΩ) $=R_C$	High (-200) $=-\frac{R_C}{r_p}$	High (100) $\approx \beta$

Emitter follower	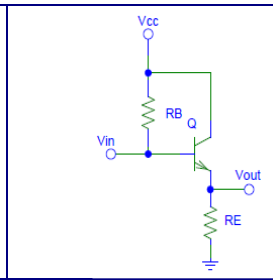	High (100 KΩ) $=R_B \| \beta R_B$	Low (20 Ω) $=R_E \| r_p$	Low (1) $=-\frac{R_C}{r_p}$	High (-50) $=\frac{\beta R_E}{R_B + Zo}$
Common base	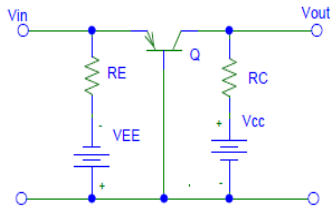	Low (20 Ω) $=R_E \| r_p$	Medium (2 KΩ) $=R_C$	High (200) $=\frac{R_C}{r_p}$	Low (-1) $=-1$

In order to use the BJT transistor as an amplifier it needs to operate in the active region. In this analysis the commercial npn transistor 2N3904 was employed using the following parameters from SPICE: I_s = 6.734x10^{-15} A, a base-emitter built-in voltage[1] of 0.75 V, and β = 416.4 [65]. The dc analysis is performed using the circuit in Figure 50.

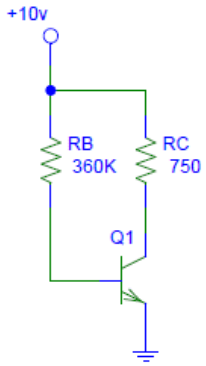

Figure 50. BJT circuit for dc analysis.

The dc base and collector currents and voltages were calculated as follows,

$$I_B = \frac{10 - V_{bi}}{R_B} = \frac{10 - 0.75}{360} mA = 0.02569mA$$

Equation 54

$$I_C = \beta I_B = 417.6 * 0.02569mA = 10.73mA$$

Equation 55

1 The built-in voltage is created in the interface of a pn junction, and it is the potential that in needs to be overcome in order to have electrons and holes diffusion, in other words it is the minimum voltage required in order to have current flow.

$$V_C = 10 - I_C R_C = 10 - .01073 * 750 = 1.9525V$$

Equation 56

$$V_B = 10 - I_B R_B = 10 - 270 * 0.0342 = 0.75V \ .$$

Equation 57

Since $V_C > V_B$, the BJT transistor is operating in active mode allowing this configuration be used as an amplifier.

4.1.1 BJT small signal model

After the operating point (Q-point) of the transistor was found with the dc analysis, a small signal model was used to study the amplification stage. In this particular case the hybrid-pi small signal model can be employed due to the low working frequency limited by the MEMS natural frequency of ~4.7 KHz. This model is represented by the circuit in Figure 51. The input voltage is the voltage of the resistor connected in series with the MEMS (input stage), and the output voltage will applied to the memristor at the load stage. There are no circuit elements connected across the MEMS avoiding any unintended change in its behavior.

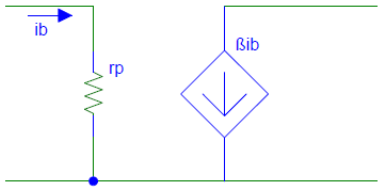

Figure 51. Hybrid-pi model for a BJT transistor.

The input resistance, r_p, is given by

$$r_p = \left.\frac{\partial V_{BE}}{\partial I_B}\right|_{Q-\text{point}} = \frac{\beta V_T}{I_C} = \frac{417.6 * 26}{10.73}\Omega = 1011.8918\Omega \ .$$

Equation 58

4.1.2 MEMS-BJT-memristor circuit analysis

The final circuit to analyze is depicted in Figure 52 where it is possible to observe that two amplifiers are cascaded to have a significant impact on the memristance.

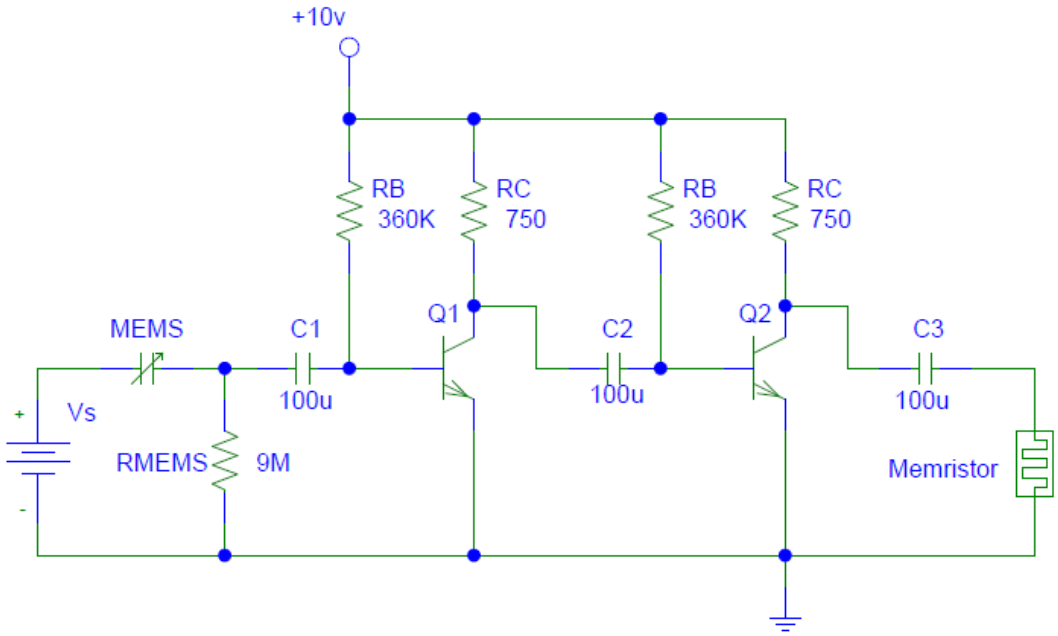

Figure 52. MEMS-BJT-memristor final circuit.

The small signal model for the cascaded BJT amplifier circuit is shown in Figure 53. Coupling capacitors were used to analyze the cut-off frequency of the amplifier.

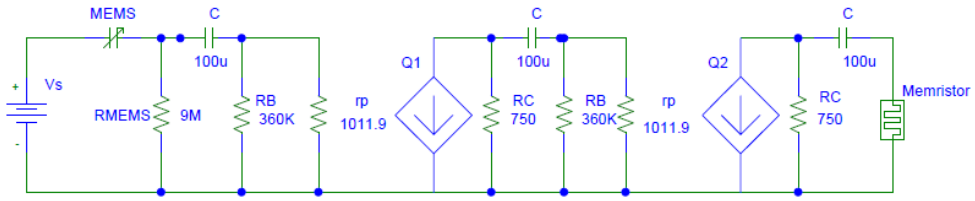

Figure 53. MEMS-BJT-memristor small signal circuit.

To solve this circuit a transfer function of the amplification stage is obtained using the Laplace transform where the capacitor impedance is given by $X_C = \frac{1}{sC}$. The transfer function also represents the amplification gain, A_{BJT}.

$$A_{BJT} = \frac{I_{memristor}(s)}{V_{RMEMS}(s)} = \left(\frac{R_C}{R_C + R_{Memristor} + \frac{1}{Cs}} \right) \left(\frac{CR_{eq}R_C s}{C(R_{eq} + R_C)s + 1} \right) \left(\frac{\beta^2 CR_{eq} s}{Cr_p^2 R_{eq} s + r_p^2} \right)$$

Equation 59

where $R_{Memristor}$ is the memristance and

$$R_{eq} = R_B \| r_p = \frac{R_B r_p}{R_B + r_p} = 1.0091\,\mathrm{K\Omega}\,.$$

Equation 60

To study A_{BJT} function, the memristance was fixed to the initial condition $w(0) = \frac{D}{2}$ giving a memristance value of 2550 Ω. All the couple capacitors are set to C = 100 µF. The impact of this value will be discussed later in this section. The frequency response can be analyzed with the bode diagram shown in Figure 54 where the magnitude and the phase are plotted, respectively. It is possible to observe that the cut-off frequency is approximately 1 Hz with a phase shift of ~135°. For operating frequencies higher than 10 Hz the phase shift is minimal. This amplifier can work within the MEMS bandwidth with minimal current distortion, in a frequency range from 10 Hz to 4 KHz. Below 1 Hz its performance will be affected including the transient response. To improve this condition larger coupling capacitors are needed to reduce the cut-off frequency.

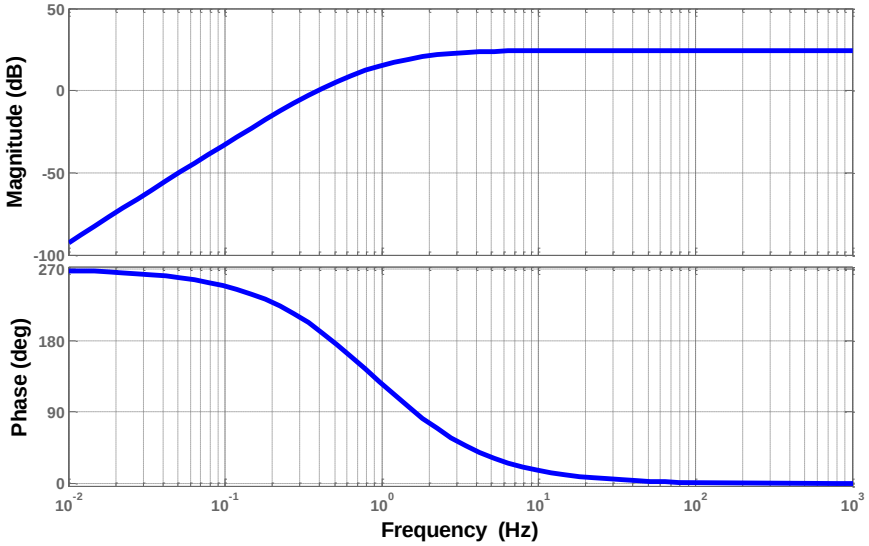

Figure 54. Bode diagram for the BJT amplifier, where the magnitud is plotted in the upper chart and the phase in the lower chart.

To solve and simulate the circuit from Figure 53 Equation 5, Equation 7, Equation 28, Equation 29, Equation 37, and Equation 59 were placed in Simulink as shown in Figure 55.

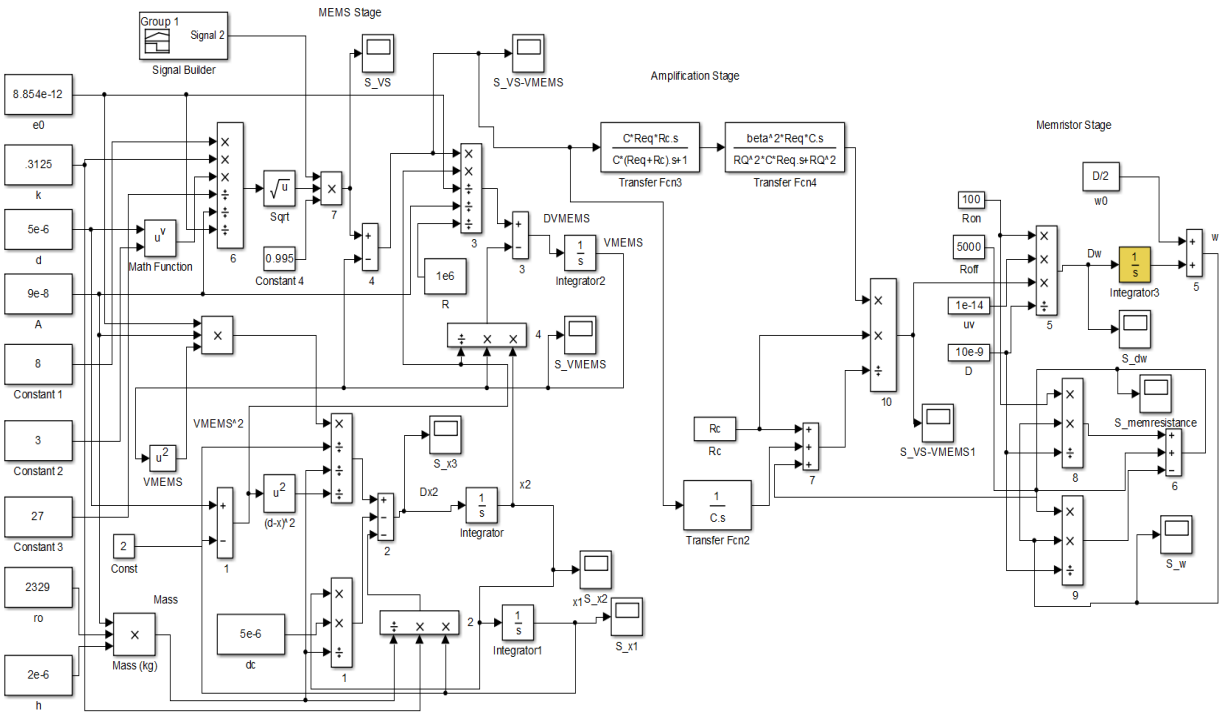

Figure 55. Simulink diagram of the MEMS-BJT amplifier-memristor.

For this case, the value of the resistor connected in series with the MEMS is 1 MΩ. The initial conditions were similar to before: $x_1(0) = 0$, $x_2(0) = 0$ for the MEMS, and for the memristor $w(0) = D/2$ or $M(0) = 2{,}550$ Ohms. The input voltage profile is a step function with an initial ramp of 4 V/sec as shown in Figure 56. The voltage ramp (instead of a discontinuous voltage step) was used to reduce a voltage spike across the 1 MΩ resistor.

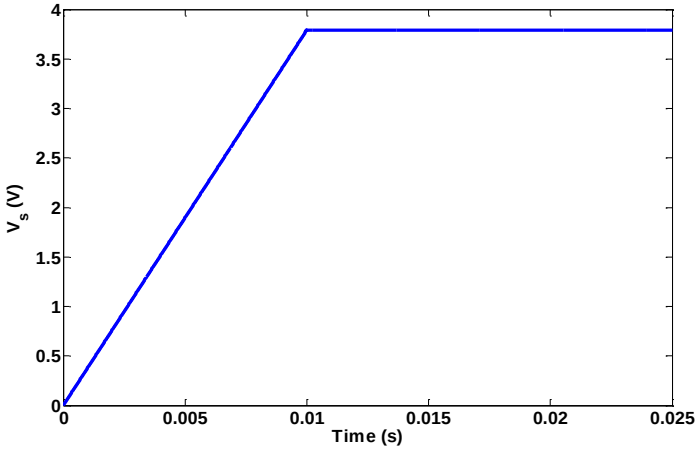

Figure 56. Input voltage for the MEMS-BJT amplifier-memristor circuit.

The simulation results for the MEMS-BJT amplifier-memristor circuit are shown in Figure 57. Figure 57 a) shows the voltage observed by the 1 MΩ resistor connected in series with the MEMS. A spike is observed when the applied voltage abruptly changes slope. A similar profile including the spike is also observed in the memristor current as shown in Figure 57 b) which shows that the current through the memristor is an amplified replica of the voltage across the MEMS as desired multiplied by the amplification gain A_{BJT}. The current is in the order of mA which indicates amplification by the BJT transistors. Figure 57 c) shows the upper plate MEMS displacement with an under-damped behavior. Finally the memristance is plotted in Figure 57 d), where two regimes are observed. In the first regime, there is a ~750 Ω modulation in the memristance from time $t = 0$ to $t = 0.01$ sec. In the second regime, a gradual increase in the memristance is observed at $t \geq 0.01$ sec although the voltage input is constant (~3.8 V) and the voltage across the MEMS goes to zero during this period. As the memristor current is also slightly below zero after the MEMS reaches steady state this effect in the memristance can be attributed to the discharge of the coupling capacitors in the amplification stage.

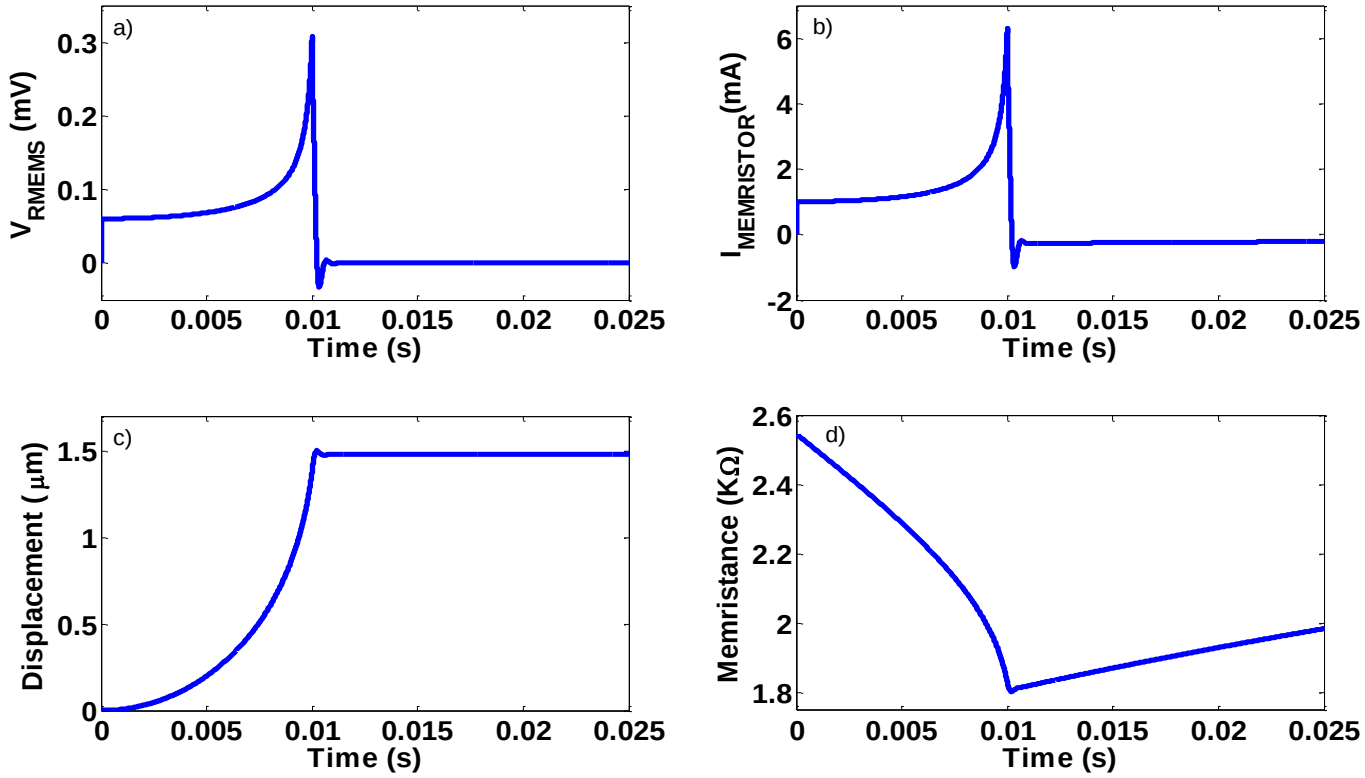

Figure 57. Results from the MEMS-BJT amplifier-memristor circuit. a) voltage at the resistor connected in siries with the MEMS, b) amplified current of the memeristor, c) MEMS displacement, and d) memristance.

To study how the coupling capacitors affect the second regime in the memristance, the circuit was simulated using two different input coupling capacitors values. The results of these simulations are presented in Figure 58 where the solid line is using a coupling capacitor of 100 µF and the dotted line is with the coupling capacitor value at 1 mF. Figure 58 shows that the larger capacitance significantly reduces the rate of the memristance change but does not completely eliminate it. This is attributed to a slower discharging time of the larger coupling capacitor; the time constant, τ, is proportional to the resistance and the capacitance in a RC circuit.

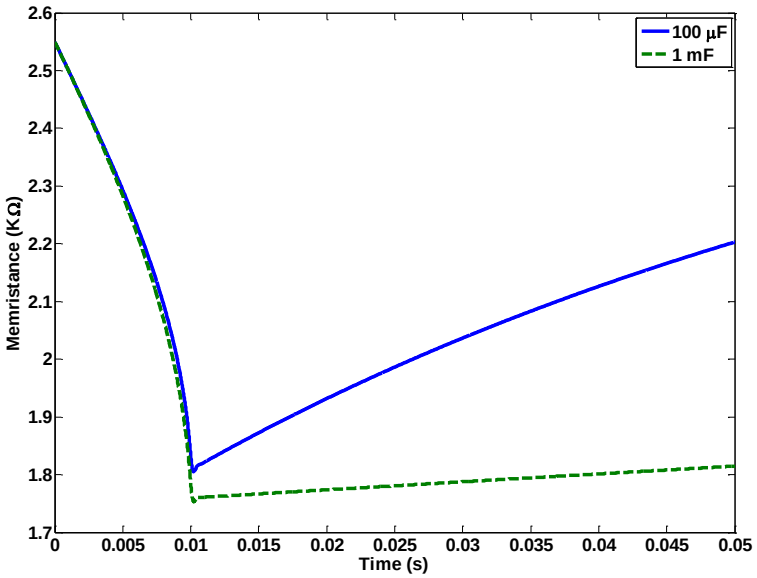

Figure 58. Memristance with different coupling capacitor values for the BJT amplification stage.

From the amplifier transfer function, a lower cut-off frequency is obtained with larger coupling capacitors. As well the capacitor discharge is slower due to a larger time constant. In this application, a wider bandwidth and an infinite capacitance discharging time are desired. This implies a high input resistance or avoid the storage of charge in the amplification stage.

Figure 59 shows the MEMS displacement versus the memristance, where a correlation between the memristance and the MEMS upper plate position is observed however the discharge of the coupling capacitor from the amplification stage will affect gradually this relationship.

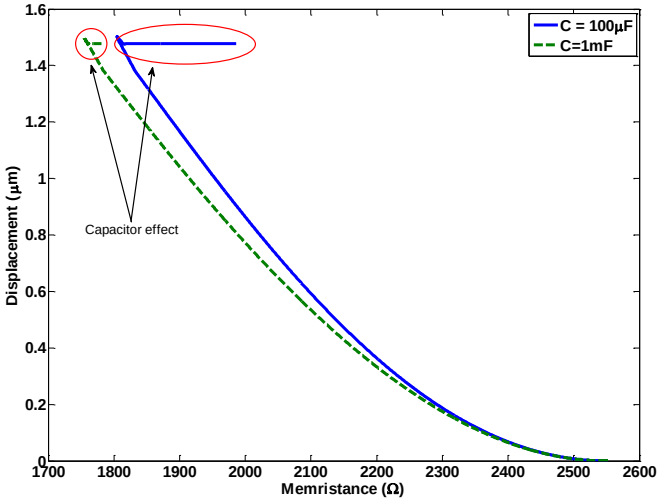

Figure 59. MEMS displacement vs memristance with different capacitor values in the BJT amplification stage.

The correlation between the MEMS displacement and the memristance with a sinusoidal input using three different frequencies is presented in Figure 60, where the pull-in voltage was used as the amplitude. A hysteresis loop is observed at low (10 Hz) and high (1 kHz) frequencies. At low frequencies the hysteresis is due to the amplification stage, whereas at high frequencies it is due to the memristor response. In contrast, a good correlation is observed at medium frequencies (100 Hz). This analysis highlights the bandwidth of the circuit.

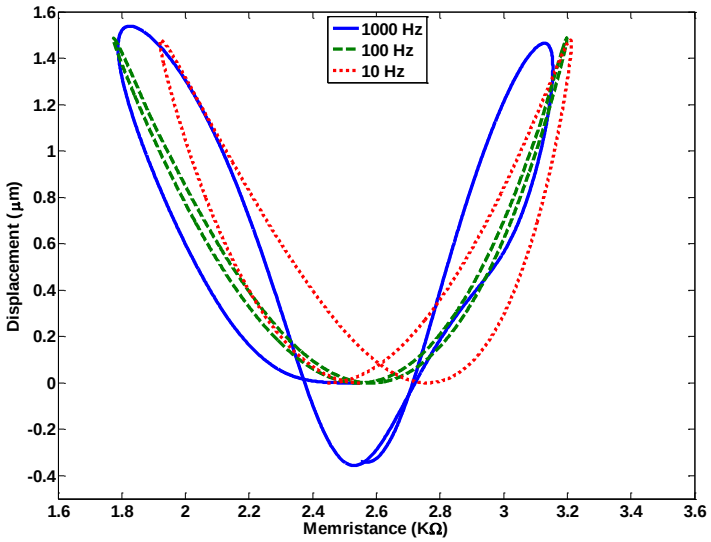

Figure 60. MEMS displacement versus memristance at different frquencies with a BJT stage.

4.2 MEMRISTOR-MEMS-MOSFET ANALYSIS

In the following section a Metal-Oxide-Semiconductor-Field-Effect-Transistor (MOSFET) will be analyzed as an amplification stage between a MEMS and a memristor. The MOSFET operation is based on the effect of electric field on a longitudinal motion of carriers. In contrast to the BJT in which the current is mainly by the diffusion of minority carriers, the MOSFET current is a result of the carrier drift under the influence of an electric field [62]. The MOSFET is a three terminal device: the source, drain, and gate, as shown in Figure 61. The gate is the transistor control terminal, i.e. the transistor working zone depends on the gate voltage (V_G) and is formed by a metal or polysilicon, silicon dioxide (SiO_2), and a semiconductor.

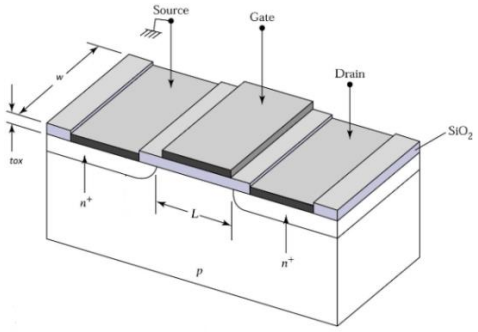

Figure 61. n-type MOSFET schematic [66].

There are two types of MOSFETs: nMOS and pMOS. The nMOS transistor is fabricated on a p-type substrate and has two n-type doped source and drain regions adjacent to the gate. In contrast a pMOS transistor is fabricated on an n-type tub region and the source and the drain are p-type regions. Figure 62 shows cross section diagrams of nMOS and pMOS transistors and their respective circuit symbol.

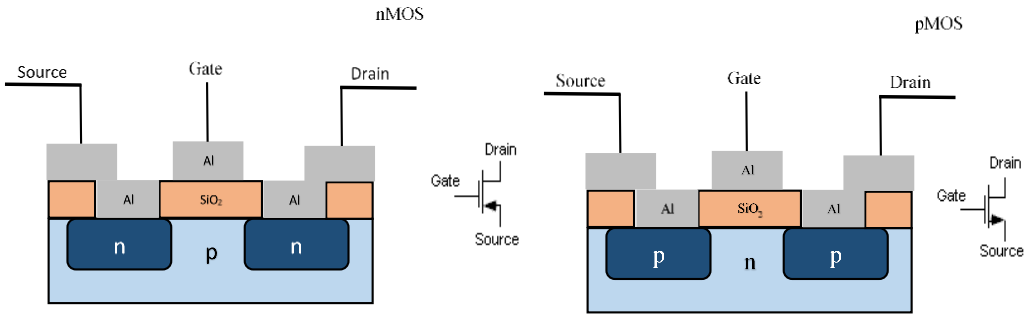

Figure 62. Cross sectional views and circuit symbol representation of nMOS (left) and pMOS (right) transistors.

As mentioned above the transistor operation mode depends on the voltage at the gate as well as the drain to source voltage (V_{DS}). The MOSFET basically has three operation regions: the cutoff region, linear region, and saturation region. Figure 63 shows a schematic description of every region. The cutoff region is when V_G is equal to zero and no current is flowing from source to drain ($I_{DS} = 0$) therefore the transistor is off. In order to operate in the linear region V_G needs to be bigger than the transistor's threshold voltage[2] (V_T) but V_{DS} needs to be less than V_G minus V_T, at this region a conduction channel due to the electric field applied in the gate is formed and I_{DS} is proportional to the V_{DS}. And finally the saturation region, this occurs when V_G is bigger than V_T and V_{DS} is bigger than the difference between V_G and V_T. At this region the channel is no longer inverted near the drain, it is pinched off instead. In this operation mode I_{DS} is independent of V_{DS}, except for the dependency in the channel modulation (λ), but is dependent on V_G.

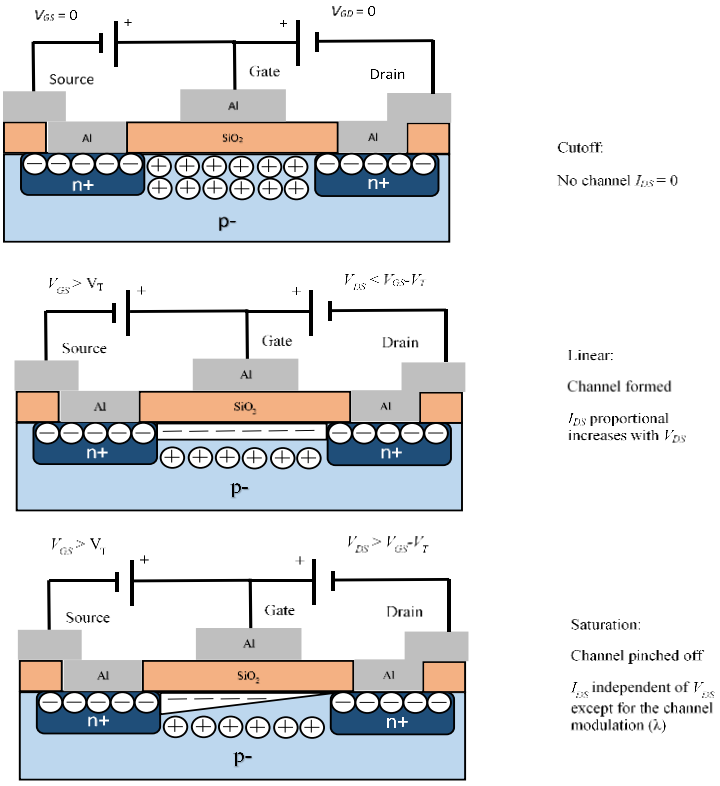

Figure 63. Schematic representation of the operation regions of nMOS.

[2] This voltage is a transistor characteristic that depends on the gate materials work function difference, surface inversion potential, charge density at the surface inversion, and the fixed positive charge that exist in the gate oxide.

Equation 61 describes the MOSFET behavior in all its operating regions, these equations are used for the level 1 [67] n-type MOSFET model in SPICE.

$$I_{DS} = \begin{cases} 0 & V_{GS} < V_T \quad \textit{cutoff} \\ \beta\left(V_{GS} - V_T - \dfrac{V_{DS}}{2}\right)(1 + \lambda V_{DS}) & V_{GS} \geq V_T \text{ and } V_{DS} < V_{GS} - V_T \quad \textit{linear} \\ \dfrac{B}{2}(V_{GS} - V_T)^2(1 + \lambda V_{DS}) & V_{GS} \geq V_T \text{ and } V_{DS} \geq V_{GS} - V_T \quad \textit{saturation} \end{cases}$$

Equation 61

where,

$$\beta = \mu \frac{\varepsilon_{OX} W}{t_{OX} L}.$$

Equation 62

For the n-type transistor, μ is the electron mobility, ε_{OX} is the oxide permittivity, t_{OX} is the oxide thickness, W is the gate width, L is the channel length, and λ is the channel length modulation. Figure 61 shows the transistor dimensions.

There are mainly three circuit configurations for the MOSFET transistor: the common-source, common-gate, and common-drain. Table 2 shows the characteristics for each configuration. Due to its high impedance and high current gain, the common-source configuration will be used for the amplifier stage.

Table 2 Summary of MOSFET circuit configurations

Configuration	Circuit	Input impedance Zi	Output impedance Zo	Voltage gain Av
Common drain	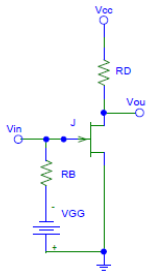	High (10 MΩ) $=R_G$	Medium (2 KΩ) $=R_D$	Medium (-10) $=-gm(rd\|\|R_D)$

Source follower	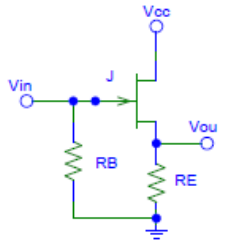	High (10 MΩ) $=R_G$	Low (20 Ω) $=rd\|\|R_S\|\|\frac{1}{gm}$	Low (<1) $=\frac{gm(rd\|\|R_S)}{1+gm(rd\|\|R_S)}$
Common gate	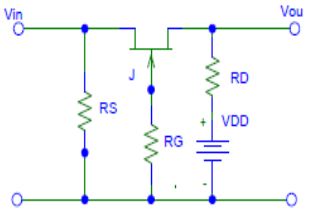	Low (1 KΩ) $=R_S\|\|\left(\frac{rd+R_D}{1+gmrd}\right)$	Medium (2 KΩ) $=R_D\|\|rd$	Medium (10) $=\frac{gmR_D+\frac{R_D}{rd}}{1+\frac{R_D}{rd}}$

For the dc analysis the circuit shown in Figure 64 will be used.

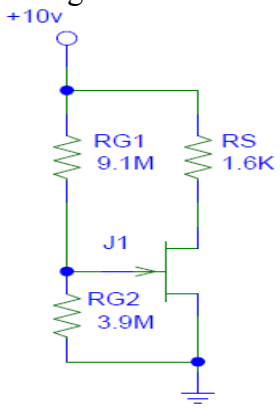

Figure 64. MOSFET circuit for dc analysis.

The MOSFET used for this application is the CMOS7 architecture from Sandia Laboratories, which is radiation hardened, where

$$\beta = \mu \frac{\varepsilon_{OX} W}{t_{OX} L} = 147 \frac{W}{L} \frac{\mu A}{V^2}$$

Equation 63

$$\frac{W}{L} = 10$$

Equation 64

$$V_T = 0.65$$

Equation 65

and

$$\lambda = 0.01 .$$

Equation 66

Thus

$$I_D = \frac{\beta}{2}(V_{GS} - V_T)^2(1+\lambda V_{DS}) = \frac{1470}{2}\left(\frac{3.9(10)}{3.9+9.1} - 0.65\right)^2(1+0.01V_{DS})$$

Equation 67

$$10 - R_S I_D - V_{DS} = 0 = 10 - 1600 I_D - V_{DS}.$$

Equation 68

Solving Equation 67 and Equation 68 for V_{DS} and I_D, the following values are obtained:

$$V_{DS} = 3.29V$$

Equation 69

$$I_D = 4.19mA.$$

Equation 70

The biasing for this circuit is such that $V_{GS} \geq V_T$ and $V_{DS} \geq V_{GS} - V_T$ which means that the transistor is operating in saturation and can be used as an amplifier.

4.2.1 MOSFET small signal model

Similar to the BJT analysis, after the operating point (Q-point) of the transistor was defined it is possible to explore the integration of the MEMS and the memristor with this amplification stage. The small signal model for the MOSFET transistor is represented by the circuit in Figure 67. Since the maximum bandwidth of the MEMS device is up to ~4.7 KHz, the parasitic capacitances of the MOSFETs were neglected. The input voltage will be the voltage of the resistor that is connected in series with the MEMS and the output voltage is applied to the memristor.

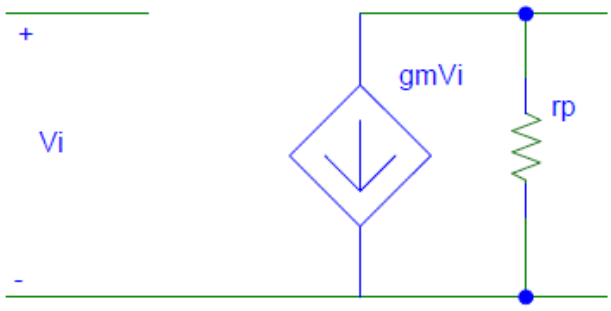

Figure 65. Small signal model for a MOSFET transistor.

The transconductance and the output resistance of the small signal model for the MOSFET are calculated as follows,

$$gm = \left.\frac{\partial I_D}{\partial V_{GS}}\right|_{V_{DS}=const} = \beta(V_{GS} - V_T)(1 + \lambda V_{DS}) = 3.568\frac{mA}{V}$$

Equation 71

$$rd = \frac{1}{g_d} = \left.\frac{\partial V_D}{\partial I_D}\right|_{V_{GS}=const} = \left(\frac{\beta}{2}(V_{GS} - V_T)^2 \lambda\right)^{-1} = 24.636K\Omega .$$

Equation 72

4.2.2 Circuit analysis

The final circuit to analyze is presented in Figure 66. Similar to the BJT, two MOSFET transistors in cascade are required to have a significant impact on the memristance change. The MOSFET amplifier has a lower gain but higher impedance compared to the BJT amplifier. This will result in a smaller modulation in memristance in the first regime and smaller rate of the gradual increase in the memristance in the second regime, as shown in the following section.

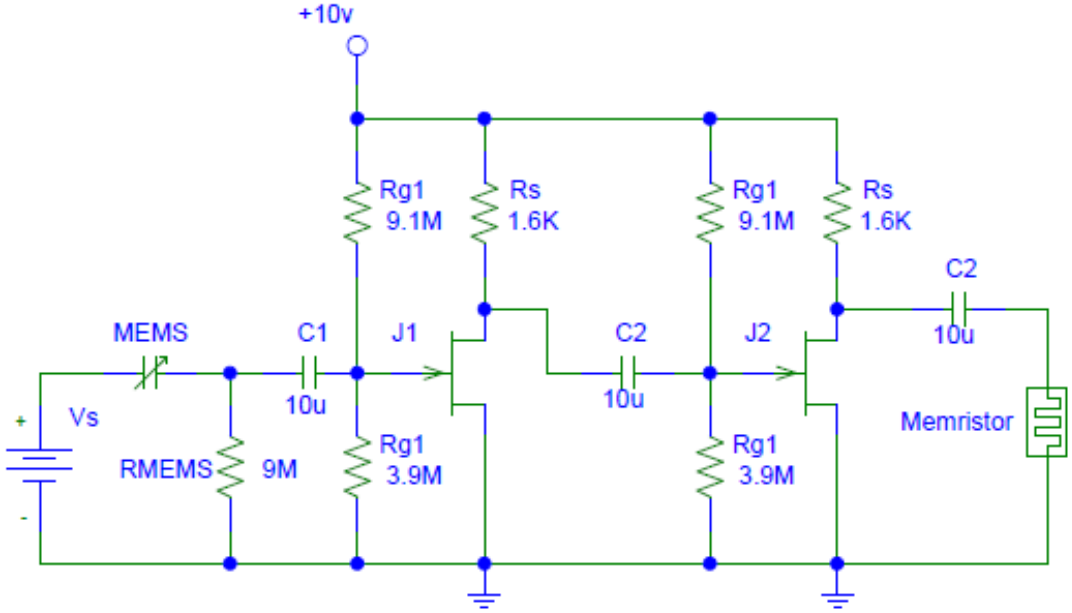

Figure 66. MEMS-MOSFET-memristor final circuit.

Replacing the MOSFET transistors for the small signal model and taking in account the coupling capacitance the circuit to analyze is shown in Figure 67.

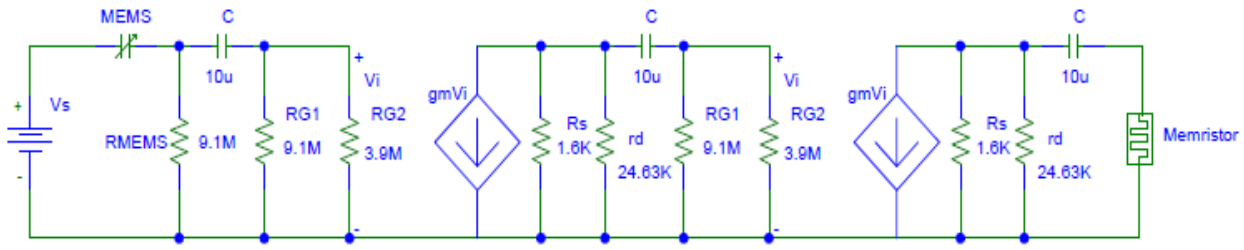

Figure 67. MEMS-MOSFET-memristor small signal circuit.

To solve this circuit a transfer function of the amplification stage is obtained using the Laplace transform where the capacitor impedance is given by $X_C = \frac{1}{sC}$. The transfer function also represents the amplification gain, A_{MOSFET}.

$$A_{MOSFET} = \frac{I_{memristor}(s)}{V_{RMEMS}(s)} = \left(\frac{R_{eq2}}{R_{eq2} + R_{Memristor} + \frac{1}{Cs}} \right) \left(\frac{CR_{eq1}R_{eq2}s}{C(R_{eq1} + R_{eq2})s + 1} \right) \left(\frac{gm^2 CR_{eq1}s}{CR_{eq1}s + 1} \right)$$

Equation 73

where $R_{Memristor}$ is the memristance and,

$$R_{eq1} = R_{G1} \| R_{G2} = \frac{R_{G1}R_{G2}}{R_{G1} + R_{G2}} = \frac{9.1 * 3.9}{9.1 + 3.9} = 2.73\,\text{M}\Omega$$

Equation 74

$$R_{eq2} = R_s \| rd = \frac{R_S rd}{R_S + rd} = \frac{1.6 * 24.63}{1.6 + 24.63} = 1.5024\,\text{K}\Omega\,.$$

Equation 75

To study the A_{MOSFET} function, the memristance was fixed to the value of 2550 Ω and the couple capacitors are set to the same C = 10 µF. The frequency response can be analyzed with the bode diagram shown in Figure 68 where the magnitude and the phase are plotted, respectively. It is possible to observe that the cut-off frequency is approximately 1 Hz for the magnitude with a phase shift of ~90°. This the phase shift becomes minimal at ~10 Hz. In the frequency range of 0.1 Hz to 1 Hz there is a shift of 90° of the current (output) with respect to the voltage (input) creating a small distortion in the signal and affecting the coupling between the MEMS and the memristor which is manifested in the transient response.

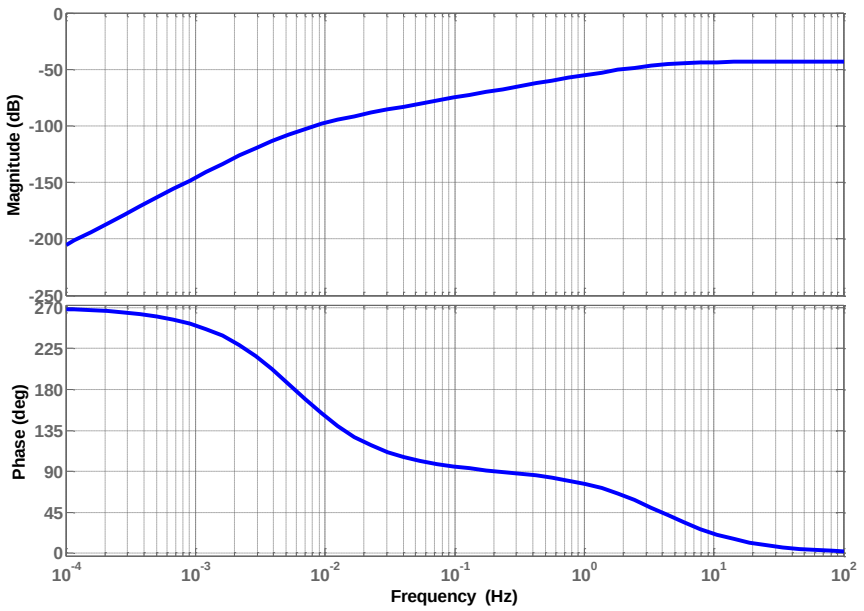

Figure 68. Bode diagram for the MOSFET amplifier, where the magnitud is ploted in the upper chart and the phase in the chart below.

Similar to the BJT case, Equation 5, Equation 7, Equation 28, Equation 29, Equation 37, and Equation 73 were place in Simulink as shown in Figure 69 for the MEMS-MOSFET-memristor circuit.

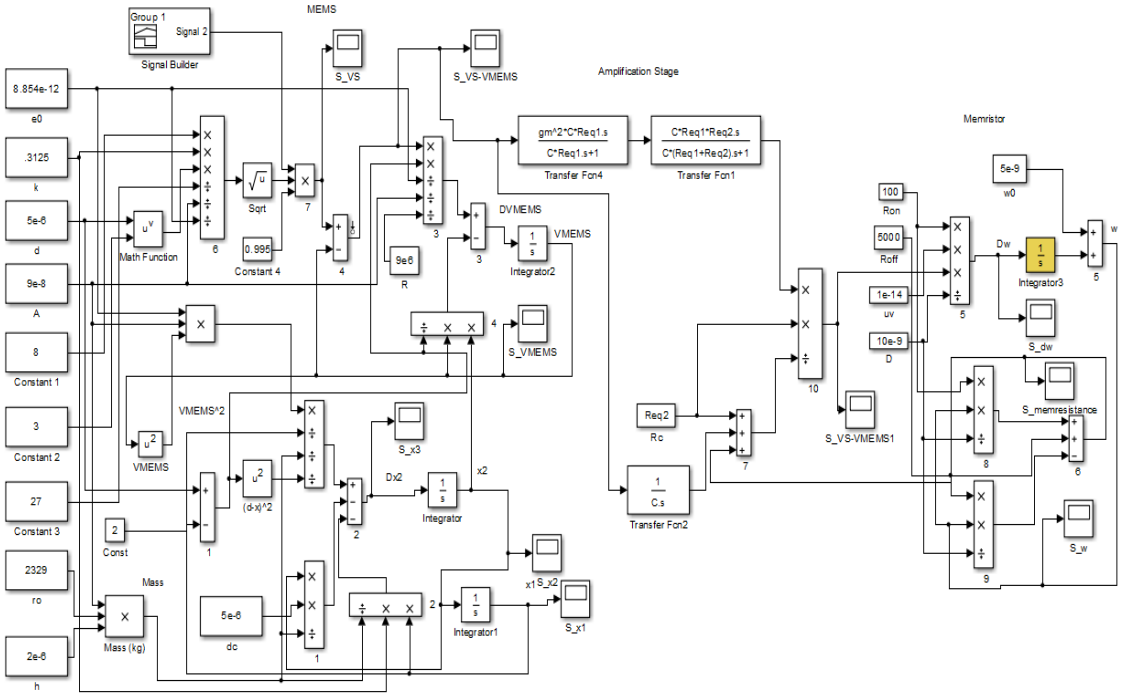

Figure 69. Simulink diagram of the MEMS-MOSFET amplifier-memristor.

For this case the value of the resistor connected in series with the MEMS is 9.1 MΩ in order to maximize the input voltage for the amplifier. The input voltage profile is given by Figure 56. The initial conditions were: $x_1(0) = 0$, $x_2(0) = 0$ for the MEMS, and for the memristor $w(0) = D/2$ or $M(0) = 2{,}550$ Ohms.

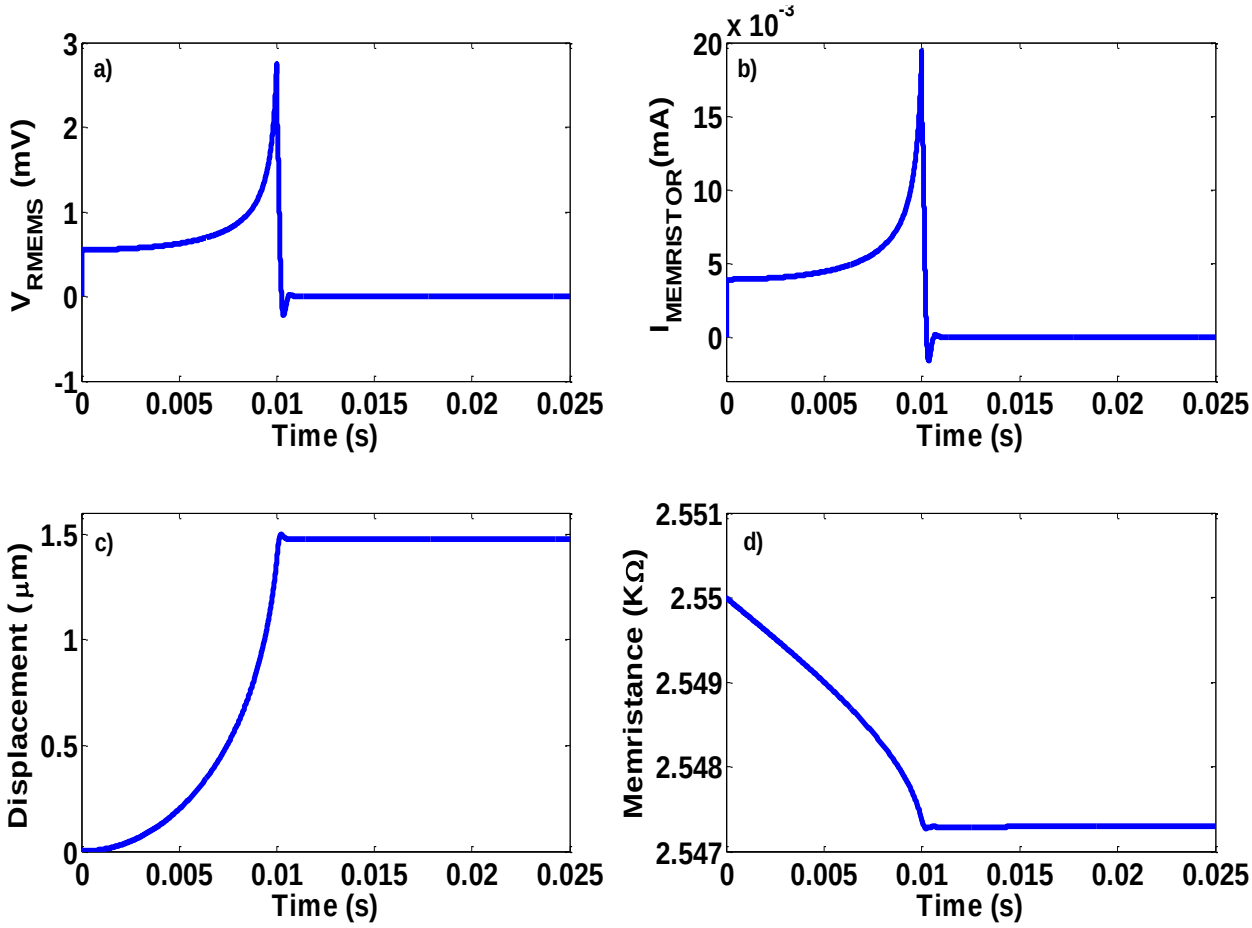

Figure 70. Results from the MEMS-MOSFET amplifier-memristor circuit. a) voltage at the resistor connected in siries with the MEMS, b) amplified current of the memeristor, c) MEMS displacement, and d) memristance.

The simulation results for the MEMS-MOSFET amplifier-memristor circuit are shown in Figure 70. Figure 70 a) shows the voltage across the 9.1 MΩ resistor connected in series with the MEMS, the magnitude is almost one order of magnitude bigger than the BJT case due to the larger resistor value. Figure 70 b) shows the current through the memristor with a similar profile as the voltage across the MEMS multiplied by the amplification gain, A_{MOSFET}. The current is in the order of μA indicating low

amplification gain. Figure 70 c) shows the upper plate MEMS displacement with an under-damped behavior, there is no significant change in the MEMS performance between the 1 M Ω and the 9.1 M Ω series resistor, as it can be compared with the BJT case. Finally the memristance is plotted in Figure 70 d), where the two regimes are observed. In the first regime, there is a ~3 Ω modulation in the memristance from time $t = 0$ to $t = 0.01$ sec. In the second regime, a gradual increase in the memristance is observed at $t \geq 0.01$ sec although the input stage is constant during this time frame. As the memristor current is slightly below zero after the MEMS stabilizes, this effect in the memristance can be attributed to the discharging of the coupling capacitors in the amplification stage. The MOSFET has larger input impedance than the BJT, which explains the slower discharging time.

In order to compare how the input impedance affects the memristance change two different values for the gate resistors were simulated. Figure 71 shows the MEMS displacement versus the memristance. The solid line is using the original values in the order of MΩ and the dotted line is with the values in the order of KΩ. It is possible to observe that the input impedance of the amplifier has a considerable contribution to the rate of the gradual increase in the memristance. As the amplifier impedance decreases the discharging time of the coupling capacitors decreases as well as creating a faster change in the memristance at the second regime.

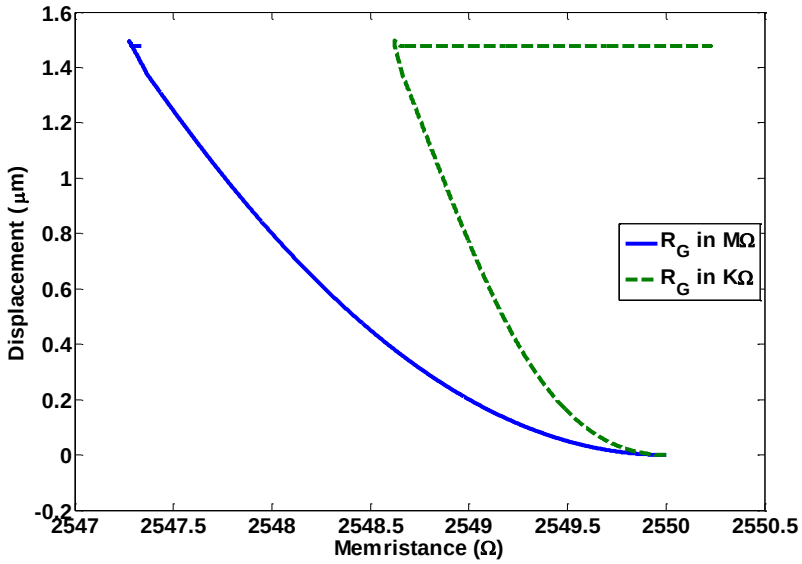

Figure 71. MEMS displacement vs memristance with different gate resistor values in the MOSFET amplification stage.

The correlation between the MEMS displacement and the memristance with a sinusoidal input voltage at different frequencies is presented in Figure 72, where the magnitude is equal to the pull-in voltage. A good correlation is observed at medium (100 Hz) and low (10 Hz) frequencies, whereas at higher frequencies (1 KHz) the correlation is represented by a hysteresis loop. The coupling at high frequencies is limited by the memristor response. However for the three frequencies simulated, the modulation of the memristance is impractically small (~3 Ω). To increase the amplification gain additional transistors in cascade are needed.

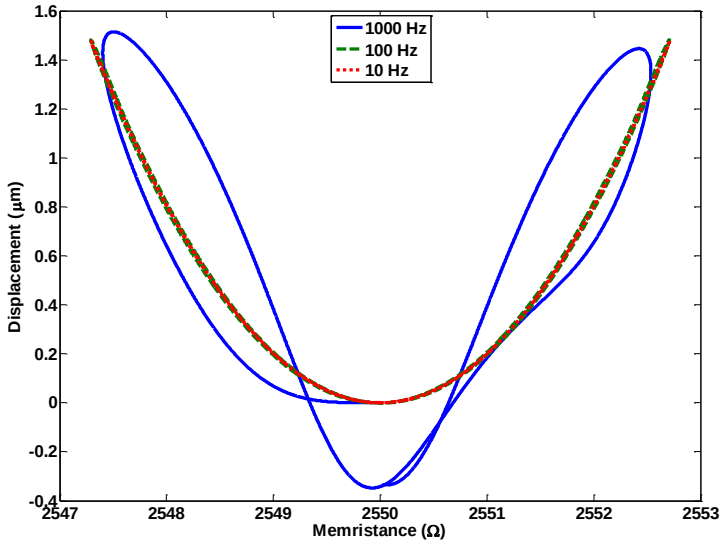

Figure 72. MEMS displacement versus memristance at different frquencies with MOSFET stage

4.3 MEMRISTOR-MEMS-OP AMP ANALYSIS

The last amplification stage to analyze is the operational amplifier (Op Amp). The Op Amp will be used to amplify the voltage across the resistor connected in series with the MEMS and then apply this voltage to the memristor. Op Amps are widely used for linear current and voltage amplification where the output voltage is proportional to the input and the proportionally constant is given by the gain. If this gain is constant, independent of the input voltage, the amplifier is considered linear [68]. The Op Amp is consists of either BJT or MOSFET transistors . One of the most common Op Amp is the 741 which consists of 22 BJT transistors. There are also two CMOS Op Amp configurations: the two stage CMOS Op Amp, and the folded cascade CMOS Op Amp. Due to the requirement of a high input

impedance the two stage CMOS Op Amp will be investigated to couple the MEMS capacitor and the memristor.

The Op Amp can be configured in two modes for amplification according to its circuitry connection: the inverting amplifier and the noninverting amplifier, as shown in left and right circuit in Figure 73, respectively.

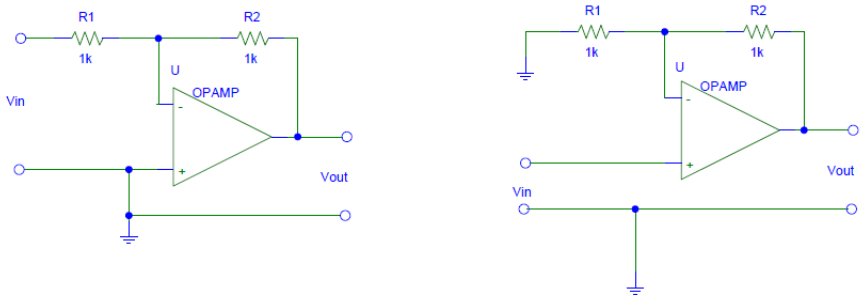

Figure 73. Op Amp amplifier configurations, inveting amplifier in the left side and noninverting amplifier in the rigth side.

The two stages CMOS Op Amp in inverting configuration will be used due to its high input impedance and large voltage gain. Additionally, some compensation needs to be taken in account in order to achieve voltage stability at the output. There are different types of compensations for the purpose of this application however the Miller capacitor compensation will be used.

Figure 74 shows the common schematic representation for a two stages CMOS Op Amp with the Miller capacitor, C_C, compensation. This structure consists of 7 MOSFETs. Parasitic capacitances are neglected since the much smaller MEMS bandwidth will be the limiting bandwidth. V_{Bias} is the output voltage offset with respect to the input and is set to zero in this case. V_{DD} and V_{SS} are the supply voltages for the Op Amp. These voltages define the saturation voltage for the negative V_{SS} and the positive V_{DD} sides.

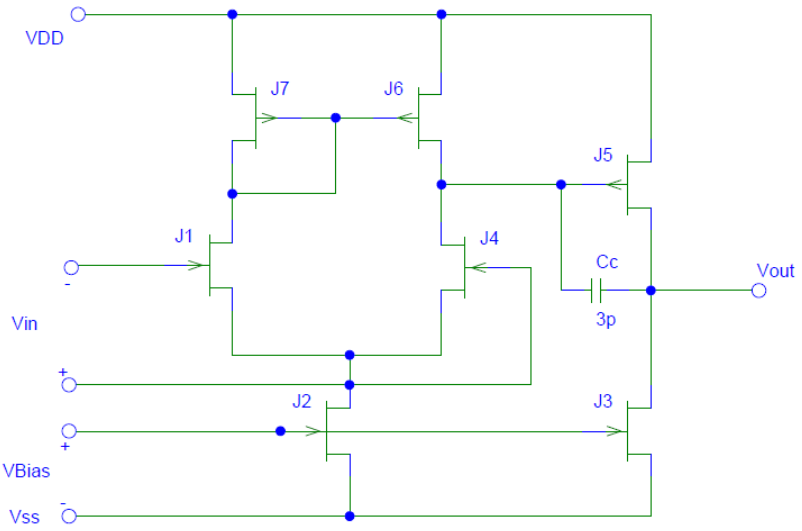

Figure 74. Two stages Op Amp amplifier schematics with Miller capacitor compensantion.

The gain for an ideal inverting amplifier is given by,

$$A_V = -\frac{R2}{R1}$$

Equation 76

where R2 = 840 KΩ and R1 = 100 Ω.

4.3.1 Op Amp small signal model

The typical small signal model for a two stages CMOS Op Amp in open-loop configuration is given by the circuit shown in Figure 75. In this case the CMOS7 architecture from Sandia National Laboratories is consider for the Op Amp design.

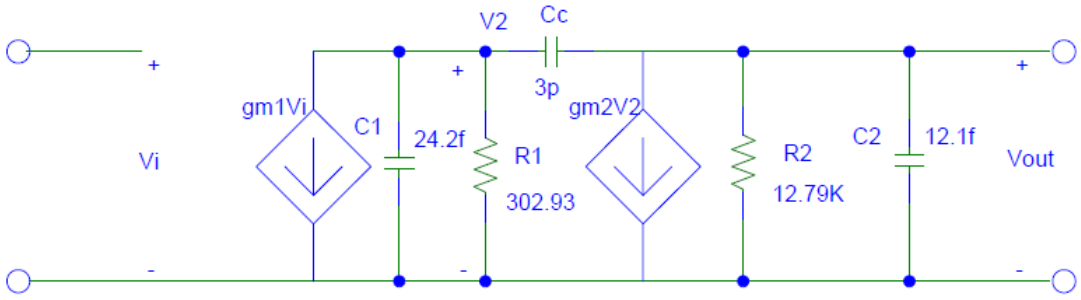

Figure 75. Two stages CMOS Op Amp small signal circuit.

Where *Cc* is the Miller capacitance, $C_1 = C_{gs6}+C_{gs7}$, $C_2 = C_{gs5}$, $R_1 \approx 1/gm_7$, and $R2 = rd_4||rd_6$, C_{gs} is the capacitance of the gate where the index indicates the transistor number from Figure 74. gm_1 and gm_2 are given by Equation 71. The capacitor, output resistor and transconductance values are given by:

$$C_1 = C_{gs6} + C_{gs7} = 2\frac{k\varepsilon_0 A}{t_{ox}} = 2\frac{3.9*8.85x10^{-12}*WL}{7x10^{-9}} = 24.2\,\text{fF}$$

Equation 77

$$C_2 = C_{gs5} = \frac{k\varepsilon_0 A}{t_{ox}} = \frac{3.9*8.85x10^{-12}*WL}{7x10^{-9}} = 12.1\,\text{fF}$$

Equation 78

$$gm_7 = \beta(V_{GS} - V_T)(1+\lambda V_{DS}) = 1360(3-0.65)(1+0.01\bullet 3.29) = 3.301\frac{\mu A}{V}$$

Equation 79

$$rd_4 = \left(\frac{\beta}{2}(V_{GS} - V_T)^2\lambda\right)^{-1} = 26.69K\Omega$$

Equation 80

$$rd_6 = \left(\frac{\beta}{2}(V_{GS} - V_T)^2\lambda\right)^{-1} = 24.63K\Omega\,.$$

Equation 81

From the circuit above, the transfer function can be obtained from nodal equations and is given by,

$$H(s) = \frac{V_{out}(s)}{V_{in}(s)} = \frac{-gm_1R_1R_2C_cs + gm_1gm_2R_1R_2}{R_1R_2(C_1C_2 + C_cC_1 + C_cC_2)s^2 + (R_1(C_1+C_2) + R_2(C_2+C_c) + gm_2R_1R_2C_c)s + 1}\,.$$

Equation 82

Equation 82 represents the open-loop transfer function of the Op Amp. In contrast, the closed-loop transfer function incorporates the negative feedback as shown in the block diagram in Figure 76.

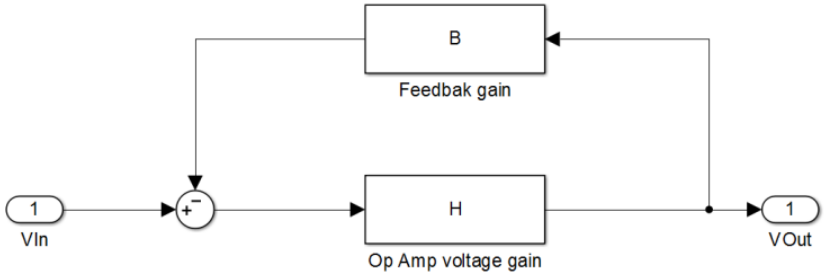

Figure 76. Op Amp closed-loop block diagram.

Taking in account the feedback gain the closed-loop transfer function is given by,

$$H_{CL}(s) = \frac{H(s)}{1 + BH(s)}.$$

Equation 83

The Op Amp frequency response can be analyzed using Equation 82 and Equation 83 with a feedback gain of 1, $B = 1$. The Bode diagram for the closed-loop transfer function is shown in Figure 77 where the magnitude and the phase are plotted, respectively. It is possible to observe that a phase shift occurs at 100 MHz and the Op Amp bandwidth is wider than the MEMS bandwidth, which is defined by the MEMS natural frequency. Frequency analysis depicted in Figure 77 indicates that the Op Amp with the characteristics of the CMOS7 architecture from Sandia National Laboratories has no distortion in the bandwidth of interest for the integration of the MEMS with the memristor

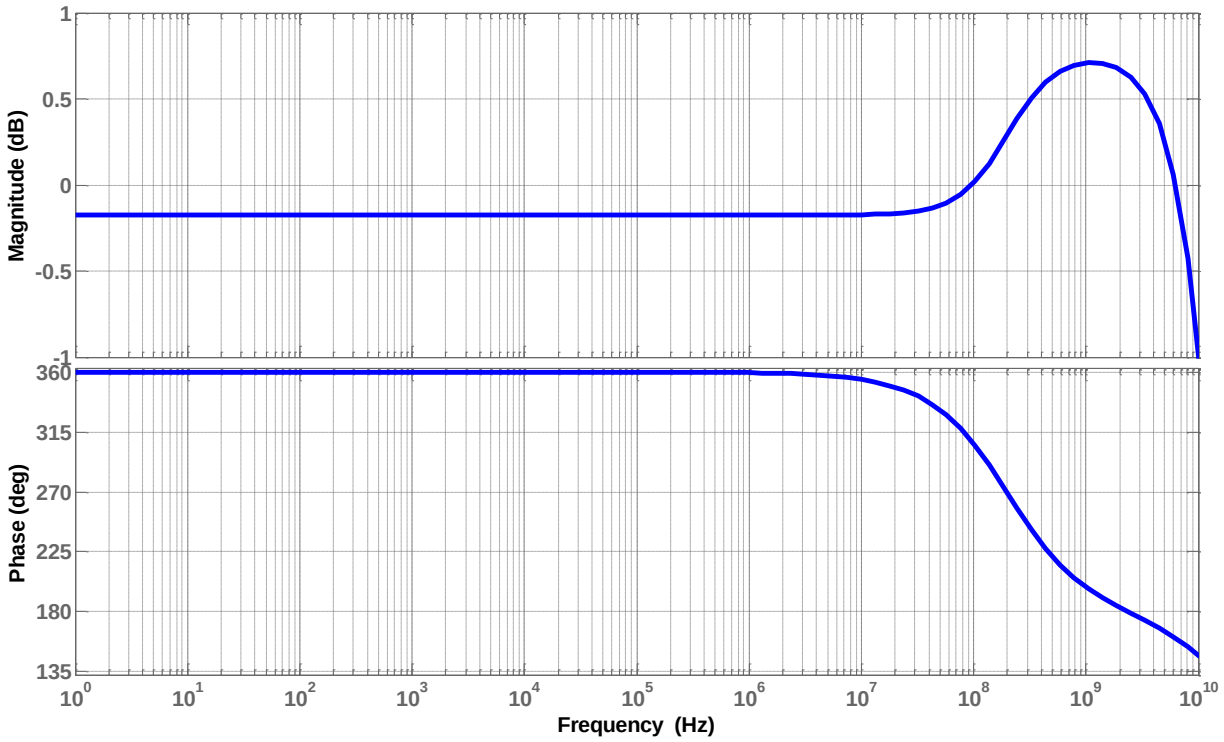

Figure 77. Bode diagram for a closed-loop Op Amp gain, where the magnitud is ploted in the upper chart and the phase in the chart below.

.

4.3.2 Circuit analysis

The previous analysis showed that the Op Amp can operate in the desired bandwidth without any distortion in the signal therefore it can be assumed that the gain for the noninverting amplifier is given by:

$$A_V \approx -\frac{R2}{R1}$$

Equation 84

The following circuit will be considered for the integration of the MEMS and the memristor, where the Op Amp will amplify the voltage at the resistor in series with the MEMS.

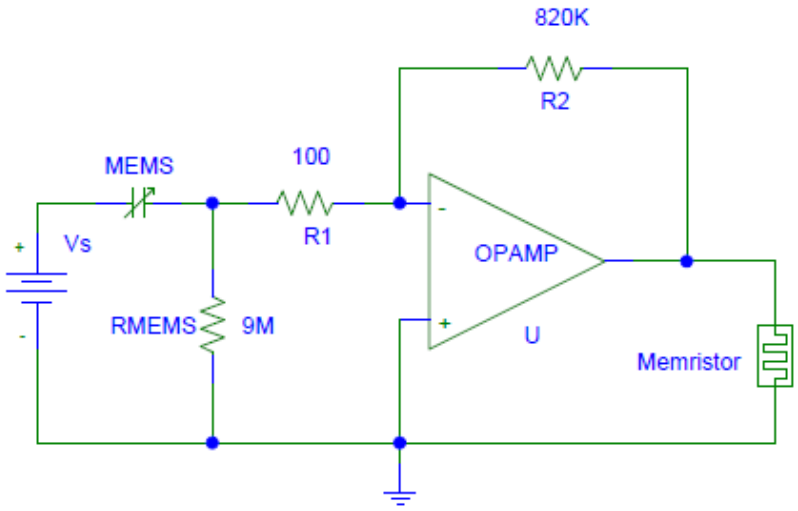

Figure 78. MEMS-Op Amp-memristor circuit schematics.

To simulate the MEMS-Op Amp-memristor circuit presented in Figure 78, Equation 5, Equation 7, Equation 28, Equation 29, Equation 37, and Equation 84 were place in Simulink as shown in Figure 79.

For this case the value of the resistor connected in series with the MEMS is 9.1 MΩ in order to maximize the input voltage for the amplifier, similar to the MOSFET case. The input voltage is the same as the previous cases given by Figure 56 as well the initial conditions: $x_1(0) = 0$, $x_2(0) = 0$ for the MEMS, and for the memristor $w(0) = D/2$ or $M(0) = 2{,}550$ Ohms.

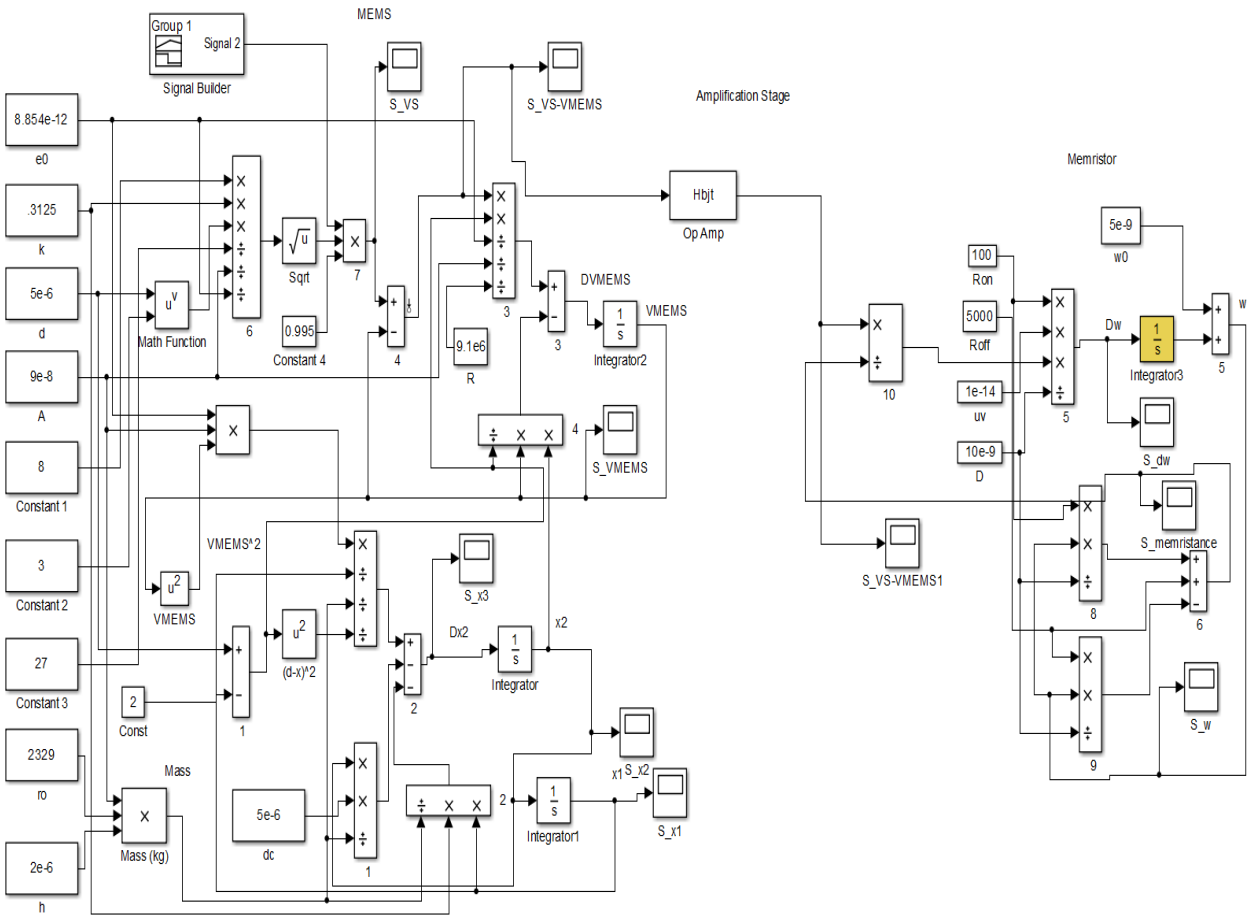

Figure 79. Simulink diagram of the MEMS-Op Amp amplifier-memristor.

Figure 80 a) shows the voltage observed by the 9.1 MΩ resistor connected in series with the MEMS. Figure 80Figure 70 b) shows the amplified voltage across the memristor, without any distortion as expected from previous analysis. Figure 80 c) shows the transient response of the MEMS upper plate with an under-damped behavior. Finally the memristance is plotted in Figure 80 d). The modulation of the memristance is approximately 1 KΩ. Contrary with the previous two cases there no gradual increase in the memristance at $t \geq 0.01$ sec. This is attributed to the elimination of the coupling capacitors needed to isolate the small signal from the dc signal and the high input impedance of the Op Amp. Although this amplifier shows a feasible coupling between the MEMS and the memristor care must be taken in the final fabrication layout to avoid the risk of parasitic capacitance.

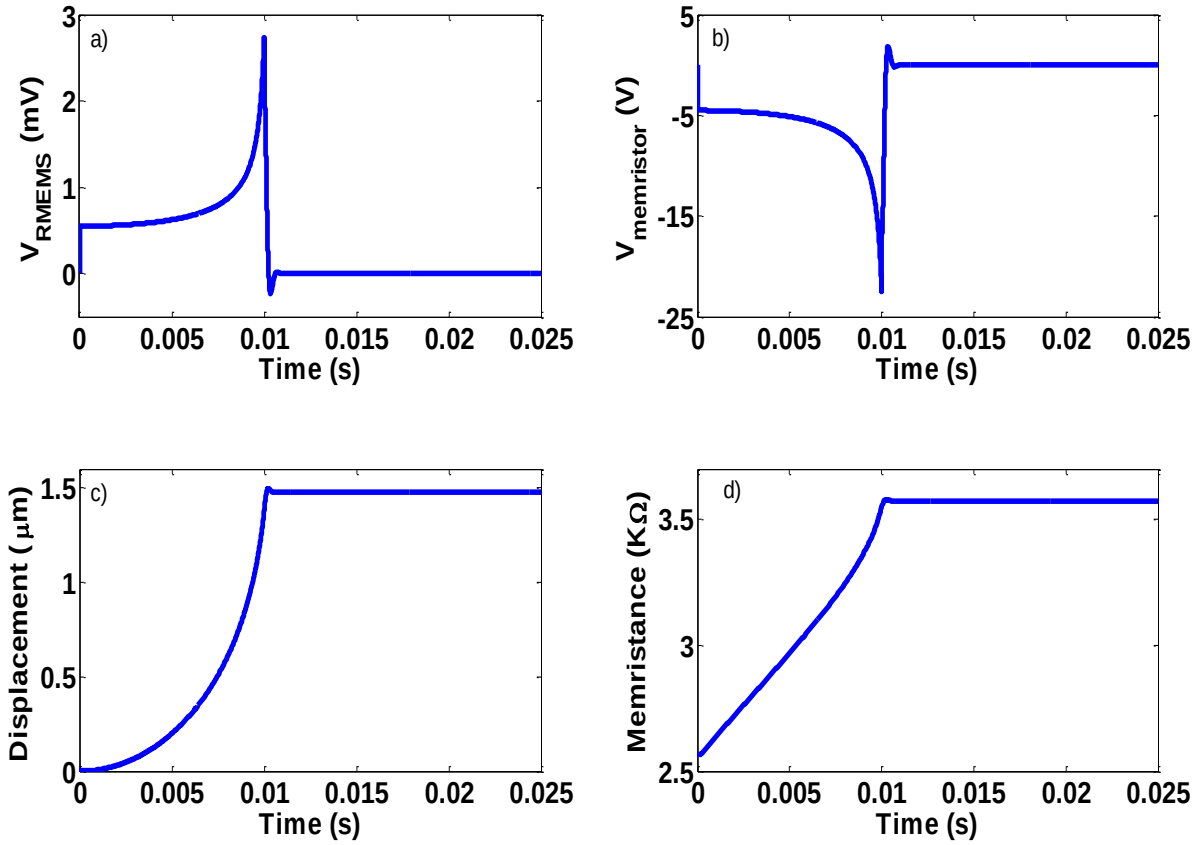

Figure 80. Results from the MEMS-Op Amp inverting amplifier-memristor circuit. a) voltage at the resistor connected in siries with the MEMS, b) amplified voltage applied to the memeristor, c) MEMS displacement, and d) memristance.

The correlation between the MEMS displacement and the memristance is plotted in Figure 81. A quadratic correlation between these two characteristics is observed making the Op Amp an acceptable amplification stage for the coupling of the MEMS and the memristor.

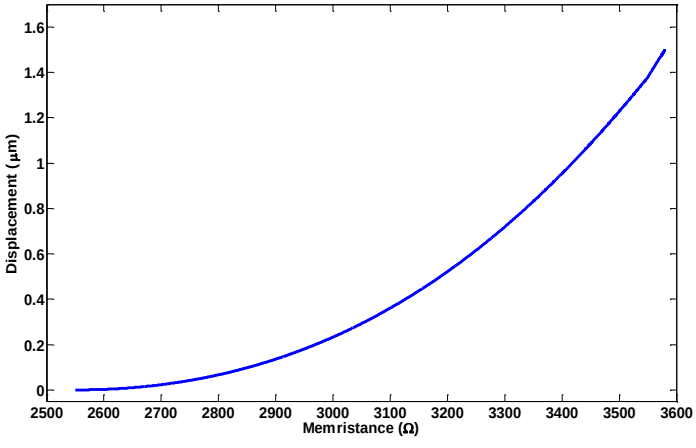

Figure 81. MEMS displacement vs memristance with the Op Amp amplification stage.

The correlation between the MEMS displacement and the memristance with a sinusoidal input voltage at different frequencies is presented in Figure 82, where the amplitude was 0.95 V_{pi} to avoid saturation at the memristor. A correlation can be noticed at low frequencies (10 Hz). In contrast, at higher frequencies (1 KHz) a hysteresis loop is observed due to the memristor response. Contrary from previous amplification stages, for this configuration the frequency is limited only by the memristor characteristics.

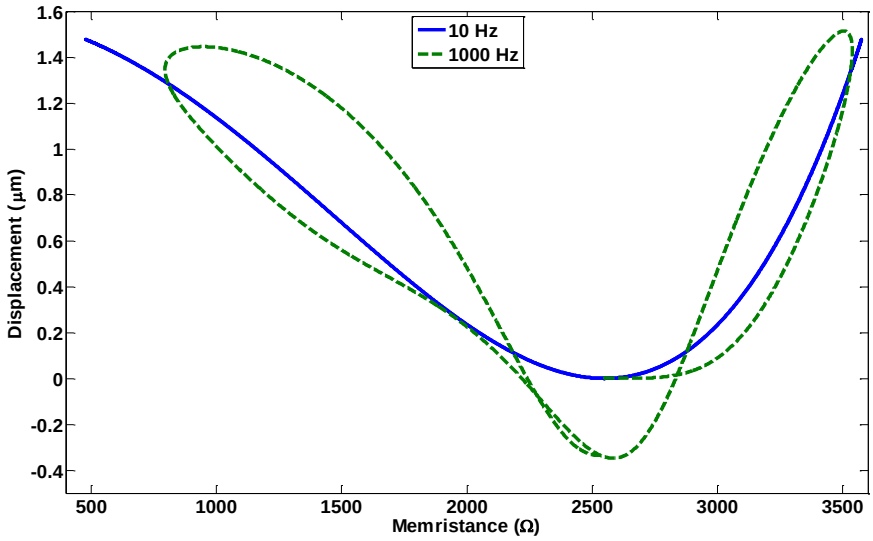

Figure 82. MEMS displacement versus memristance at different frquencies with an Op Amp stage.

4.4 AMPLIFICATION STAGE CONCLUSIONS

In this section three different amplification stages were analyzed in order to integrate the MEMS parallel plate capacitor with the memristor. The first case analyzed was the BJT transistor as an amplifier element. Two transistors in cascade were used in order to observe a significant change in the memristance. The modulation in the memristance was ~750 Ω but a gradual increase in the resistance was observed after the input stage achieves stability, which was attributed to the coupling capacitor discharge and low impedance of the BJT transistors. This condition can be mitigated with bigger coupling capacitors, however an impractical size of capacitor is needed to increase the time constant, τ. On the other hand, the MOSFET amplification has a larger input impedance compared to the BJT

transistor. The drawback in the MOSFET configuration is the low amplification gain which produces a modulation of only ~3 Ω in the memristance of using two transistors in cascade.

Lastly, the Op Amp stage was investigated. This configuration offers a large amplification gain, high input impedance, and there is no need for coupling capacitors. The inverting configuration with an amplification gain A_v = -8200 generates a memristance modulation of ~ 1KΩ, additionally the gradual change in the memresistance when the MEMS stage reaches steady state is practically eliminated. However its physical architecture is more complex requiring optimizations for its layout design to avoid parasitic capacitance.

4.4.1 Memristor and MEMS charge coupling

Although an amplification stage was required to couple the memristor and the MEMS devices, a relationship between the memristance and the MEMS displacement was observed. As both devices depend on the charge, a mathematical expression for the memristance and the MEMS dynamics can be obtained in order to find a function to translate resistance into distance. This function will be used in section 5 as part of the feedback.

For this Op Amp amplification circuit, the correlation between the memristance and the MEMS displacement is as follows,

$$V_{memristor} = A_v V_{RMEMS}$$

Equation 85

$$Mi_{memristor} = A_v R i_{MEMS}$$

Equation 86

$$\int M dq_{memristor} = \int A_v R dq_{MEMS} \,.$$

Equation 87

Substituting **Error! Reference source not found.** in Equation 87 and integrating both sides the following relationship is obtained,

$$\left(\frac{Ron^2 \mu_V}{D^2} - \frac{RonRoff \mu_V}{D^2} \right) \frac{q_{memristor}^2}{2} + Roff q_{memristor} = A_v R q_{MEMS} \,.$$

Equation 88

Replacing the charge of the memristor for the memristance and the charge at the MEMS for **Error! Reference source not found.**, the MEMS dynamics shows a quartic relationship with the memristance as shown in Equation 89. This indicates that the MEMS displacement can be a function of the memristance through a polynomial of 4th order.

$$\frac{1}{2}\frac{D^2 Roff}{Ron^2\mu_V - RonRoff\mu_V}\left((M-Roff)^2+(M-Roff)\right)=A_v R\sqrt{2\varepsilon_0 A}\left(m\frac{d^2x}{dt^2}+d_c\frac{dx}{dt}+kx\right)^{1/2}.$$

Equation 89

Figure 83 shows a fitting of a polynomial of 4th order for the displacement versus the memristance for the Op Amp case. The polynomial will be used to obtain the MEMS displacement from the memristance and is given by:

$$x_f = p_1 M^4 + p_2 M^3 + p_3 M^2 + p_4 M + p_5$$

Equation 90

Where x_f is the fitted displacement, p_1 = 3.8x10^{-19}, p_2 = -4.172x10^{-15}, p_3 = 1.847x10^{-11}, p_4 = -3.809x10^{-08}, and p_5 = 3.015x10^{-05}.

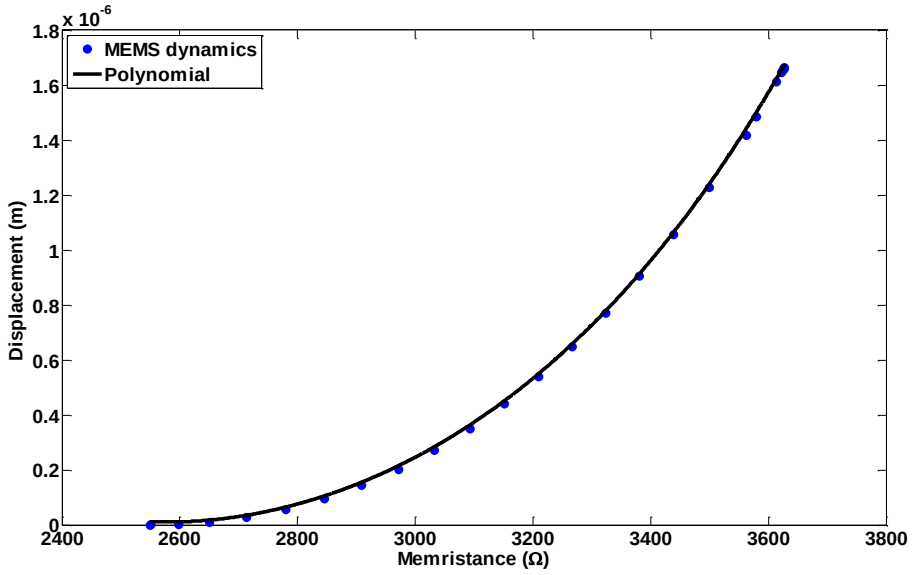

Figure 83. MEMS displacement versus memristance an Op Amp stage, solid line represent a polinomial fitting to describe the MEMS displacement as function of the memristance.

This relationship cannot be observed directly measuring the voltage at the MEMS series resistor as shown in Figure 84.

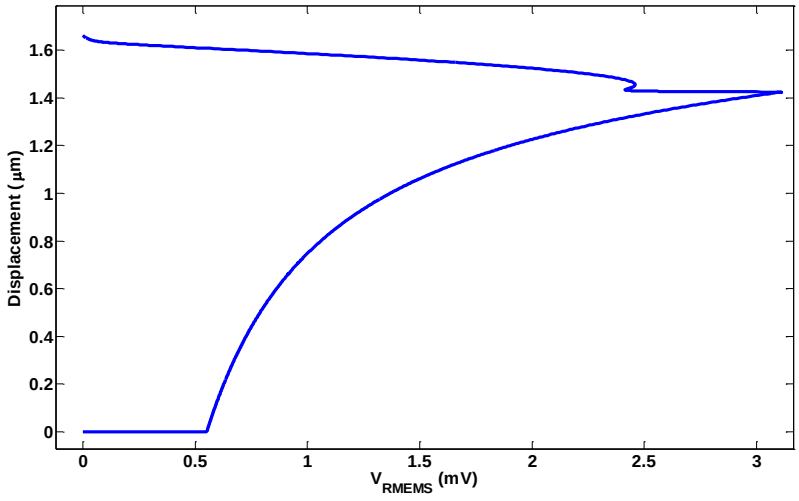

Figure 84. MEMS displacement versus the voltage observe by the resistor in series (V_{RMEMS})

5 MEMS-Memristor Closed-Loop Control

As mentioned above, the displacement for MEMS parallel plate capacitor is limited to 1/3 of the total gap due to force stability. Thus the maximum voltage that can be applied (pull-in voltage) is constrained depending on the MEMS dynamic behavior. There are techniques to improve the working range and the most common is adding extra capacitors in series in the MEMS structure [69]. However this is achieved by adding a dielectric film on the bottom electrode [35] reducing the gap as well. Another technique is to use an open-loop charge controller, which has been shown effective in high range of the total gap [70]. However the drawback is that open-loops are sensitive to external disturbances. A different alternative is implementing a voltage closed-loop control for the upper electrode position [71]. This technique has shown its effectiveness extending the travel range up to 90% of the gap [72]. In order to have a complete closed-loop control a feedback signal is required; for example the MEMS displacement must be measured. Figure 85 shows how a closed-loop control can increase the MEMS displacement working range by manipulating the voltage. The first chart is the upper electrode position from the bottom electrode where it is possible to observe that the initial gap is 100 μm and can be reduce to around 10 μm which is 90% of the total gap with an applied voltage shown in the third chart. It is possible to observe that the voltage goes down when the gap is getting smaller which indicates that applying the correct voltage the electrode position will not collapse [71].

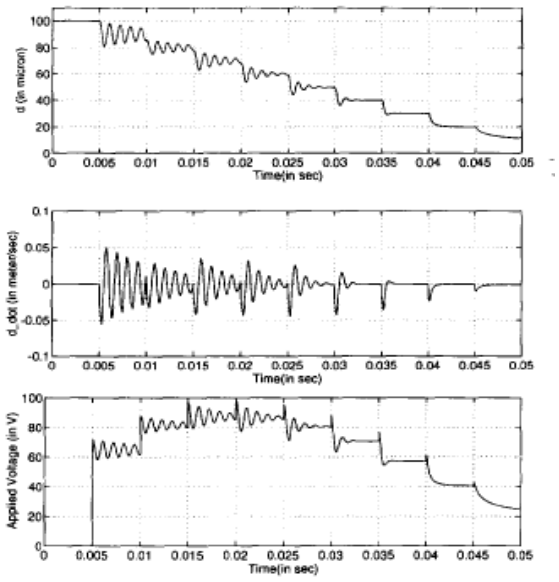

Figure 85. Closed-loop control for the MEMS upper plate position [71].

Even though a control can be designed to increase the MEMS operating range, one of the key elements in the closed-loop control that needs to be addressed is the feedback signal; for this particular case the electrode position needs to be sensed. Thus the main issue with this application is the lack of a suitable displacement sensing element [35]. A usual technique to verify the MEMS dynamics is by optical methods with a set-up depicted in Figure 86, which is not suitable for commercial applications and it is used for testing purposes only.

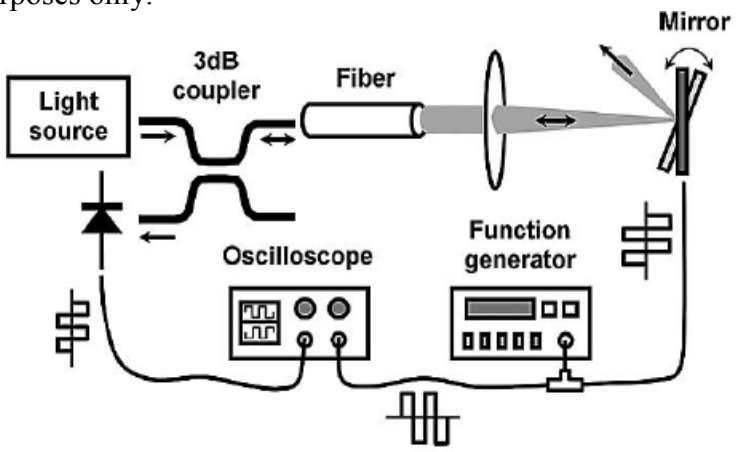

Figure 86. Optical measurement system to measure the angle in a MEMS tilting mirror position [73].

There are other alternatives to sense the MEMS displacement. One of them is to measure the capacitance on the MEMS [74], [75] but modulation, amplification and demodulation processes are required increasing the circuitry and adding ac signals to the system. Another alternative is to measure the electrostatic voltage at the MEMS [76] then apply this measurement to Equation 24 to determine the MEMS position. However external instrumentation needs to be connected directly with the MEMS terminal adding parasitic capacitances and affecting the MEMS behavior. Moreover the voltage needs to be computed in order to obtain the displacement and this creates uncertainty due to the need to solve a nonlinear equation. Importantly, the integration of the memristor with the MEMS can address the feedback deficiency for a closed-loop control. In section 3 it was shown that the memristance can give information about the MEMS displacement dynamics although the resistance modulation was impractical when connecting the memristor directly in series with the MEMS. In section 4 three different amplification stages were analyzed in order to increase the resistance change while

maintaining a correlation with the MEMS displacement and without affecting the MEMS performance avoiding parasitic capacitance connected directly with the MEMS.

In this section, a closed-loop control is proposed using the pole placement design technique. The memristor is treated together with the amplification stage as the feedback element. Figure 87 shows the schematics of the complete system to be analyzed; where the correlation block represents the polynomial equation that correlates the MEMS displacement and the memristance.

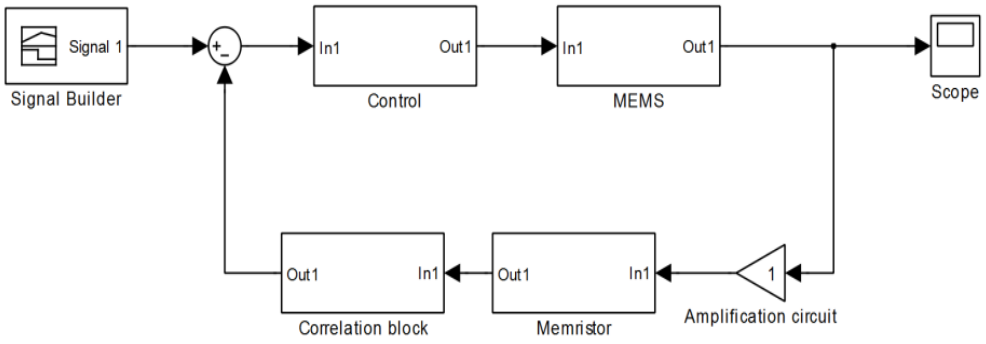

Figure 87. Closed-loop control for the MEMS displacement using the memristor as sensing element.

5.1 MEMS MODEL LINEARIZATION

The state space of the MEMS with the resistor in series can be represented by,

$$\dot{x}_1 = x_2 = f_1$$

Equation 91

$$\dot{x}_2 = \frac{\varepsilon_0 A x_3^2}{2m(d-x_1)^2} - \frac{d_c}{m}x_2 - \frac{k}{m}x_1 = f_2$$

Equation 92

$$\dot{x}_3 = \frac{(Vs - x_3)(d-x_1)}{\varepsilon_0 AR} - \frac{x_3 x_2}{(d-x_1)} = f_3 .$$

Equation 93

Where x_3 is the MEMS voltage V_{MEMS}. The equilibrium points occur when $f_1 = 0$, $f_2 = 0$, and $f_3 = 0$ and are given by,

$$X_2 = 0$$

Equation 94

$$\frac{\varepsilon_0 A X_3^2}{2m(d-X_1)^2} = \frac{k}{m}X_1$$

Equation 95

$$Vs_{eq} = X_3 .$$

Equation 96

Expanding the nonlinear system in terms of perturbations and neglecting the higher order terms in Taylor's series, the linearized model using the previous equilibrium points is given by,

$$\dot{x}_\delta = Ax_\delta + Bu_\delta$$

Equation 97

$$y_\delta = Cx_\delta ,$$

Equation 98

where A is the transition matrix and it is expressed by,

$$A = \begin{bmatrix} \frac{\partial f_1}{\partial x_1} & \frac{\partial f_1}{\partial x_2} & \frac{\partial f_1}{\partial x_3} \\ \frac{\partial f_2}{\partial x_1} & \frac{\partial f_2}{\partial x_2} & \frac{\partial f_2}{\partial x_3} \\ \frac{\partial f_3}{\partial x_1} & \frac{\partial f_3}{\partial x_2} & \frac{\partial f_3}{\partial x_3} \end{bmatrix} = \begin{bmatrix} 0 & 1 & 0 \\ \frac{\varepsilon_0 A X_3^2}{m(d - X_1)^3} - \frac{k}{m} & -\frac{d_c}{m} & \frac{\varepsilon_0 A X_3}{m(d - X_1)^2} \\ 0 & -\frac{X_3}{d - X_1} & -\frac{d - X_1}{\varepsilon_0 A R} \end{bmatrix}.$$

Equation 99

The input vector B is given by,

$$B = \begin{bmatrix} \frac{\partial f_1}{\partial u} \\ \frac{\partial f_2}{\partial u} \\ \frac{\partial f_3}{\partial u} \end{bmatrix} = \begin{bmatrix} 0 \\ 0 \\ \frac{d - X_1}{\varepsilon_0 A R} \end{bmatrix},$$

Equation 100

and the output vector C is equal to:

$$C = \begin{bmatrix} 1 & 0 & 0 \end{bmatrix}.$$

Equation 101

The transfer function of the system can be obtained from

$$H(s) = C(sI - A)^{-1}B,$$

Equation 102

where I is the identity matrix. Replacing A, B, and C the transfer function is express by,

$$H(s) = \frac{C_1}{C_2 s^3 + C_3 s^2 + C_4 s + C_5},$$

Equation 103

where,

$$C_1 = -AX_3\varepsilon_0\left(X_1 - d\right)$$

Equation 104

$$C_2 = AR\varepsilon_0 m\left(X_1^2 - 2X_1 + d^2\right)$$

Equation 105

$$C_3 = ARd_c\varepsilon_0\left(X_1^2 - 2X_1 + d^2\right) + m\left(3dX_1^2 - X_1^3 - 3d^2X_1 + md^3\right)$$

Equation 106

$$C_4 = ARk\varepsilon_0\left(X_1^2 - 2X_1 + d^2\right) + d_cX_1\left(-X_1^2 + 3dX_1 + 3d^2\right) + d_cd^3$$

Equation 107

$$C_5 = kX_1\left(-X_1^2 + 3X_1 - 3d^2\right) + A\varepsilon_0\left(-X_3^2 + Rkd^2\right) + kd^3\,.$$

Equation 108

The transfer function shows three poles, if the equilibrium point is chosen such as $X_1 < \frac{d}{3}$ the poles are located in the left plane indicating a stable system. Figure 88 shows the pole locations for $X_1 = \frac{d}{1000}$. The MEMS voltage is obtained by substituting this value into Equation 95: $X_3 = V_{Seq} = 0.3128$. The two conjugated poles are in the negative part of the real axis near the origin, as shown in the inset, and the third pole is in the left side of real axis far from the origin probing that the system is stable at this point.

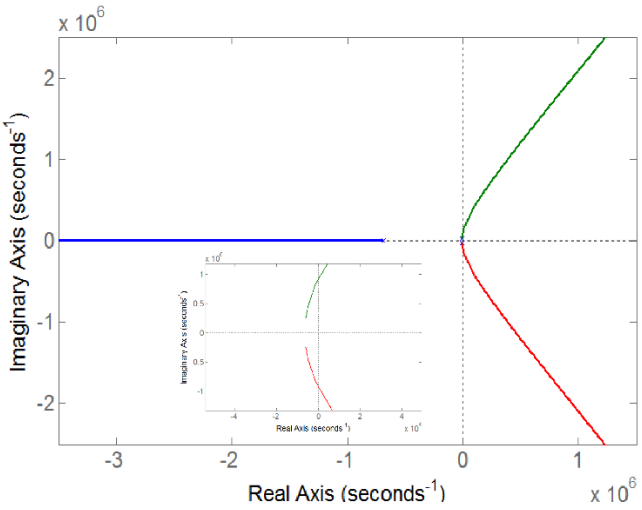

Figure 88. Pole location for the linearized MEMS system for an equilibrium point equal to *d*/1000.

On the other hand if the equilibrium point is selected as $X_1 = \frac{d}{3}$ one of the poles moves to the origin indicating marginal stability. Figure 89 shows the pole locations for this equilibrium point, the

three poles are located in the real axis, two of the in the left side and the third one in the origin, as shown in the inset.

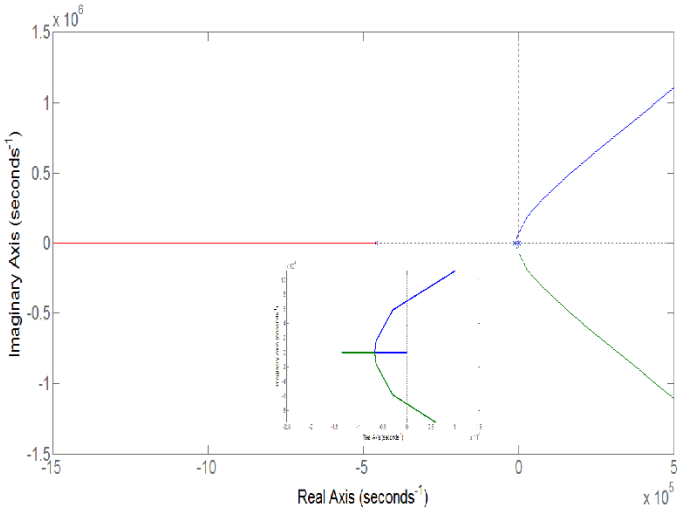

Figure 89. Pole location for the linearized MEMS system for an equilibrium equal to *d*/3.

If the equilibrium point is chosen beyond the pull-in displacement one of the poles will be located in the right side of the real axis thus the system will be unstable. Figure 90 shows the pole location when the equilibrium point is $X_1 = \frac{d}{2}$. Here it is possible to observe the poles in the real axis, two of them in the left side and the third in the right side, as shown in the inset.

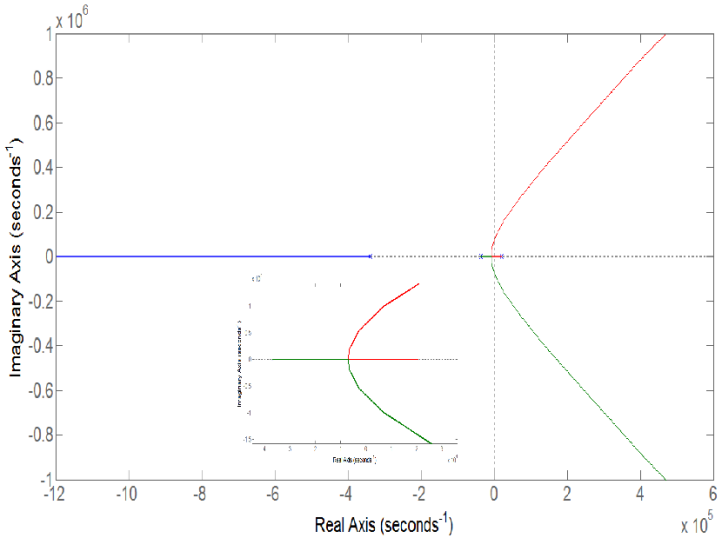

Figure 90. Pole location for the linearized MEMS system for an equilibrium equal to *d*/2.

In order to compare the linear model versus the nonlinear model both models are submitted to a step response with the same initial conditions. Figure 91 shows the time response of the nonlinear model (blue points) versus the linearized model (green solid line) at an equilibrium point of $X_1 = \frac{d}{6}$. For this case the initial condition were: $x_1(t_0) = \frac{d}{6}$, $x_2(t_0) = 0$, $x_3(t_0) = 3.368$, and the systems were subjected to an 89% of V_{pi}.

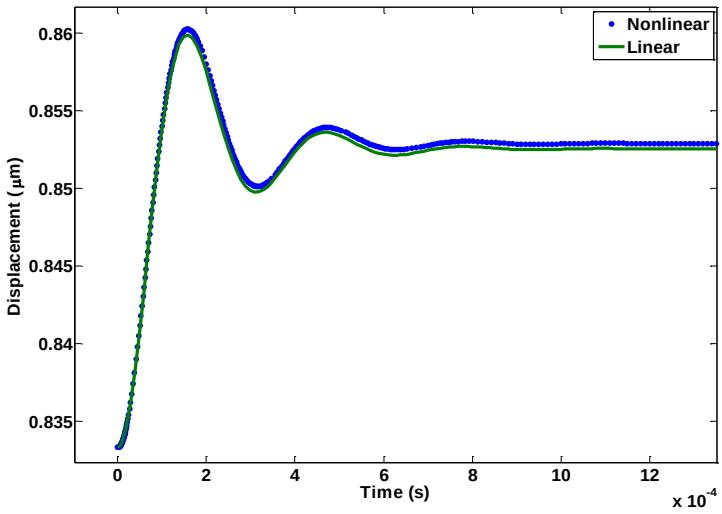

Figure 91. Nonlinear model versus linearized model with the initial condition of $x_1(0) = \frac{d}{6}$.

It is possible to observe that the linearized model has a good approximation to the nonlinear model. However this approximation only works near to the equilibrium point. If the system operates far from that point the error between the linear system and the nonlinear system will be greater.

5.1 CONTROL DESIGN

The controller is design by the conventional pole placement technique using the linearized model in Equation 99 to Equation 101. The control law is given by:

$$u = -Kx$$

Equation 109

where K is the feedback gain vector that will be selected in order to locate the poles in the desired place:

$$K = \begin{bmatrix} K_1 & K_2 & K_3 \end{bmatrix}.$$

Equation 110

Substituting Equation 109 in Equation 97 the space state is represented by,

$$\dot{x}_\delta = Ax_\delta - BKx_\delta = (A - BK)x_\delta .$$

Equation 111

Notice that the transition matrix is changed to (A-BK). In order to obtain the feedback gains, the eigenvalues of the transition matrix should be equal to a desired polynomial that contains the location of the poles. In other words:

$$\det|sI - A + BK| = Pd$$

Equation 112

In this case there are three states thus the polynomial needs three zeros and can be expressed as follows,

$$Pd = (s^2 + 2\zeta\omega_n s + \omega_n^2)(s + a) .$$

Equation 113

Where ζ is the damping coefficient, ω_n determines the time response, and a is an arbitrary pole located in the left side of the real axis. For an over-damped system, where $\zeta > 1$, its generic time response is given by

$$c(t) = 1 - \exp\left(-\left(\zeta - \sqrt{\zeta^2 - 1}\right)\omega_n t\right).$$

Equation 114

In this case the damping coefficient is chosen to be $\zeta = 1.2$ and arbitrary pole to be at -20. Setting the condition that the 98% of the final response needs to be achieved in 20 ms in Equation 114, ω_n can be obtained by

$$\omega_n = \frac{-\ln(1 - c(t))}{\left(\zeta - \sqrt{\zeta^2 - 1}\right)t} = \frac{-\ln(0.02)}{0.02\left(1.2 - \sqrt{1.2^2 - 1}\right)} = 364.4685 .$$

Equation 115

Substituting the values in Equation 113 the K vector can be obtained by solving Equation 112 as follows:

$$\det\left|\begin{bmatrix} s & 0 & 0 \\ 0 & s & 0 \\ 0 & 0 & s \end{bmatrix} - \begin{bmatrix} 0 & 1 & 0 \\ \dfrac{\varepsilon_0 A X_3^2}{m(d - X_1)^3} - \dfrac{k}{m} & -\dfrac{d_c}{m} & \dfrac{\varepsilon_0 A X_3}{m(d - X_1)^2} \\ 0 & -\dfrac{X_3}{d - X_1} & -\dfrac{d - X_1}{\varepsilon_0 AR} \end{bmatrix} + \begin{bmatrix} 0 & 0 & 0 \\ 0 & 0 & 0 \\ \dfrac{d - X_1}{\varepsilon_0 AR}K_1 & \dfrac{d - X_1}{\varepsilon_0 AR}K_2 & \dfrac{d - X_1}{\varepsilon_0 AR}K_3 \end{bmatrix}\right| = Pd$$

Equation 116

In this case the equilibrium point is chosen to be $X_1 = \frac{d}{1000}$ thus the vector gain values are:

$$K = \begin{bmatrix} 4.998x10^5 & -37.3858 & -1.016 \end{bmatrix}$$

Equation 117

The block diagram for the closed-loop control is shown in the Figure 92.

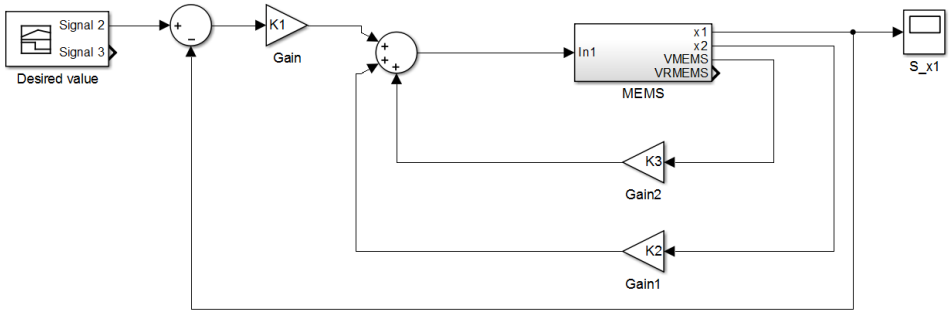

Figure 92. Block diagram for a closed-loop control with the nonlinear MEMS model.

Figure 93 shows the normalized input and output of the block diagram above. It is possible to observe that the output is not achieving the desired set point. This is due to the normalization error, the gain constants are calculated based in an equilibrium point if the system is set to a position far from this point the stationary error will increase.

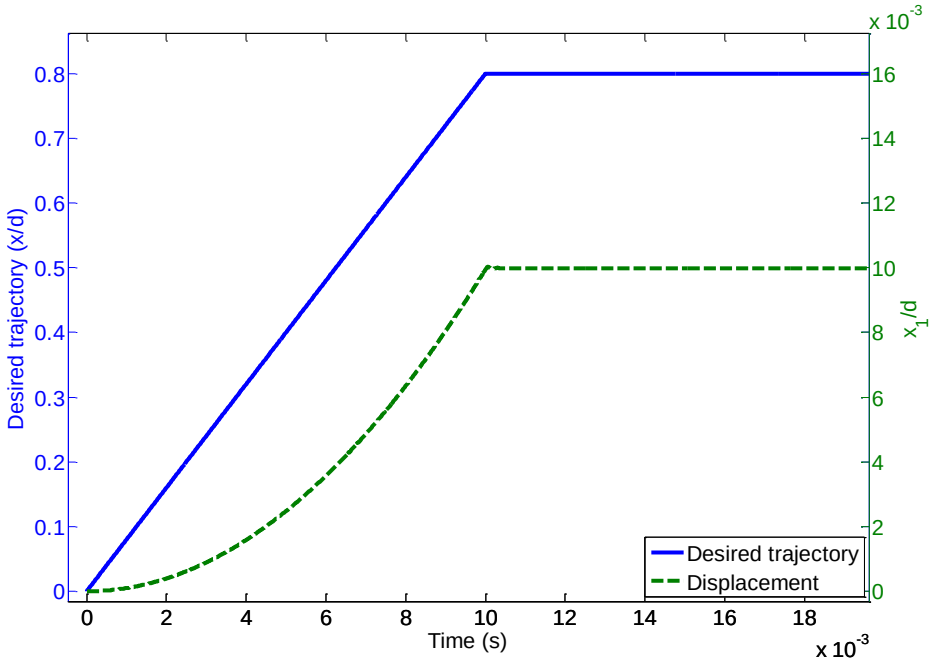

Figure 93. MEMS displacement desired trajectory versus the MEMS displacement real trajectory with calculated feedback gains for the nonlinear model.

This can be addressed by tuning the gain constants. After the tuning procedure, the gain vector can be as follow:

$$K = \begin{bmatrix} 1.7499x10^{8} & -1.1216x10^{4} & -1.016 \end{bmatrix}.$$

Equation 118

Figure 94 shows a desired trajectory versus the MEMS response for the nonlinear model. Two final set points are plotted, the first case is at 95% of the total displacement and the second case is at 50%. Here it is possible to observe a minimal stationary error as well as good response to the desired trajectory.

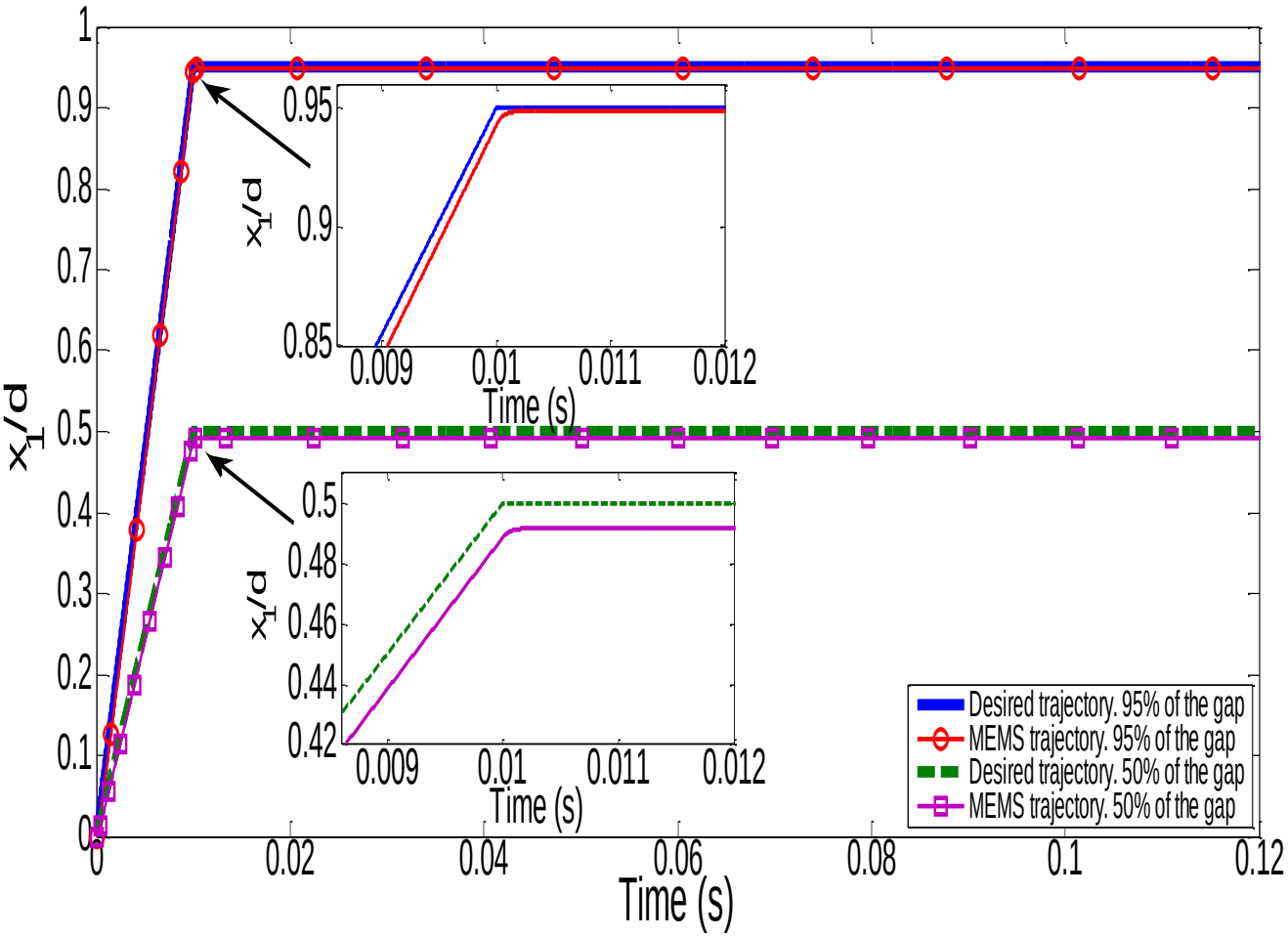

Figure 94. MEMS displacement desired trajectory versus the MEMS displacement real trajectory with tuned feedback gains for the nonlinear model.

5.2 MEMRISTOR INTEGRATION TO THE CONTROL LOOP

The control designed in the previous section is considering that all the states are monitored. However as mentioned before, measuring the MEMS position or its velocity is not a straight forward task. Usually the velocity is estimated by designing a speed observer [77]. Therefore the potential for the memristor in this application is not limited to the measurement of the MEMS displacement but it can be used to estimate the velocity as well.

Figure 95 shows the block diagram contemplating the memristor as a sensing element, taking in consideration the amplification stage between the MEMS and the memristor. The block after the memristor is the correlation block which is the polynomial obtained in Equation 90.

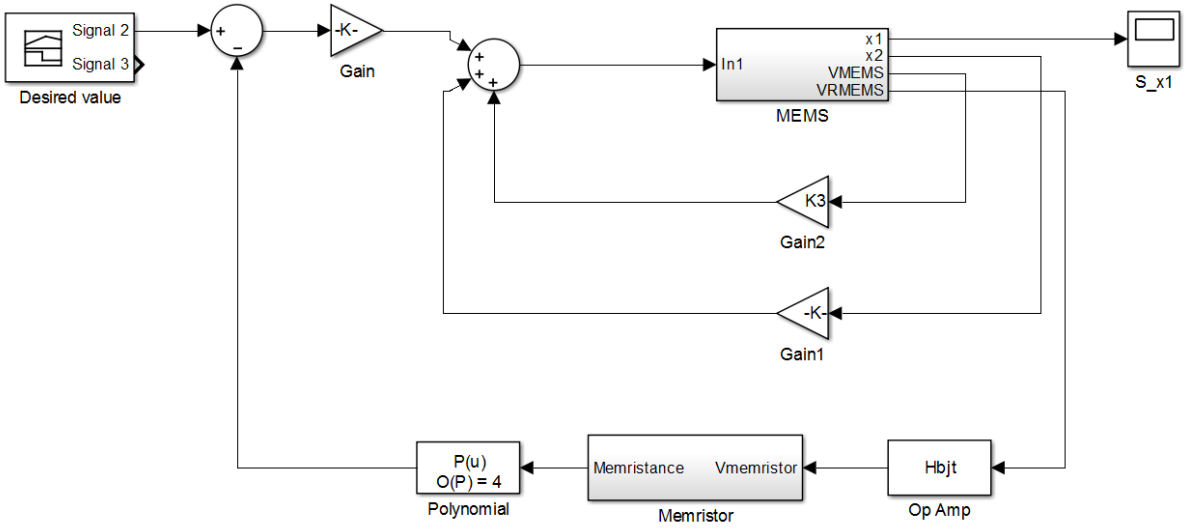

Figure 95. Block diagram for a closed-loop control with the nonlinear MEMS model and the memristor as position sensor.

Due to sudden voltage change in the resistor connected to the MEMS in series, the gain constants need to be tuned to avoid saturation in the memristor and in the amplification stage. Thus, for this case the gain vector is given by:

$$K = \begin{bmatrix} 1.999x10^{7} & -3.7386x10^{3} & -1.016 \end{bmatrix}.$$

Equation 119

Figure 96 shows the displacement estimated with the memristor and the nonlinear MEMS displacement.

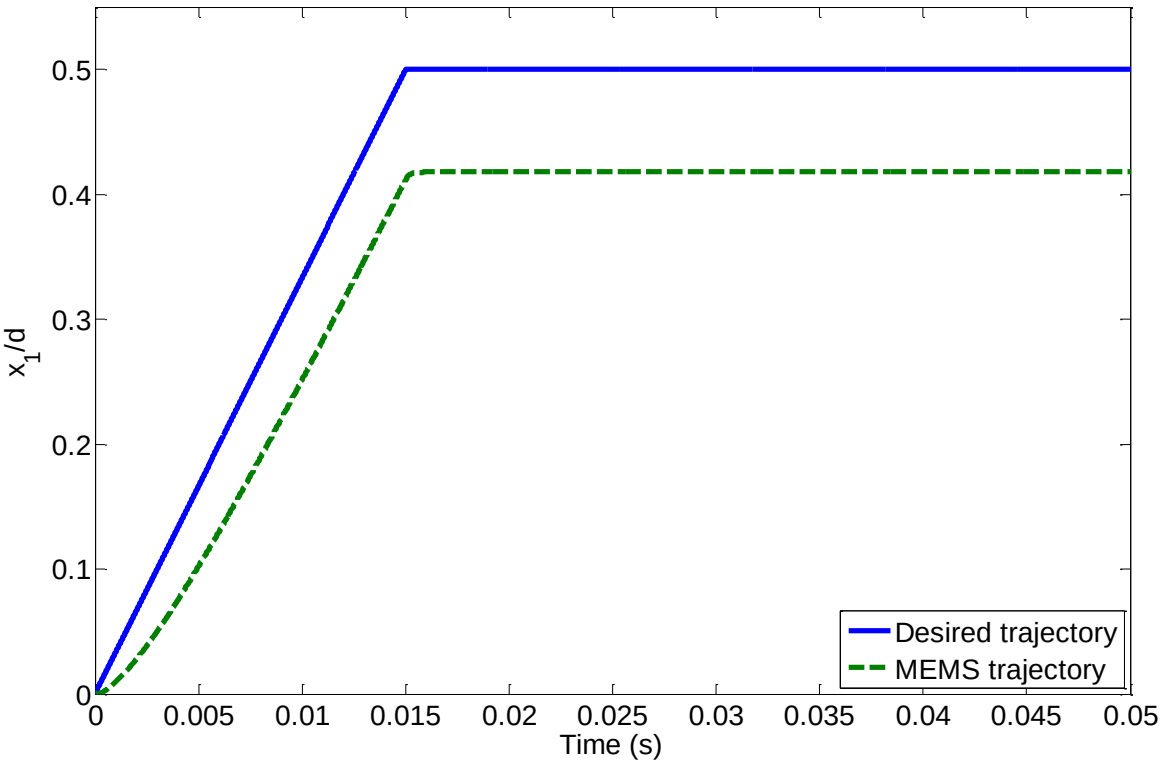

Figure 96. MEMS displacement desired trajectory versus the MEMS displacement real trajectory with tuned feedback gains for the nonlinear model using the memristor as feedback element.

It is possible to observe a considerable error in the full trajectory as well as in the stationary state. Additional the MEMS upper plate speed needs to be measure as well the voltage at the MEMS. In order to estimate the velocity, the displacement obtained by the memristor can be differentiated with respect time.

The estimated velocity $\hat{x}_2$ is given by,

$$\hat{x}_2 = \frac{1000s+1}{s+1000}\left(p_1 M^4 + p_2 M^3 + p_3 M^2 + p_4 M + p_5\right).$$

Equation 120

Figure 97 shows the velocity through the time of the MEMS upper plate, solid line, and the estimated velocity obtained from Equation 120. Thus this is an acceptable estimation for the speed.

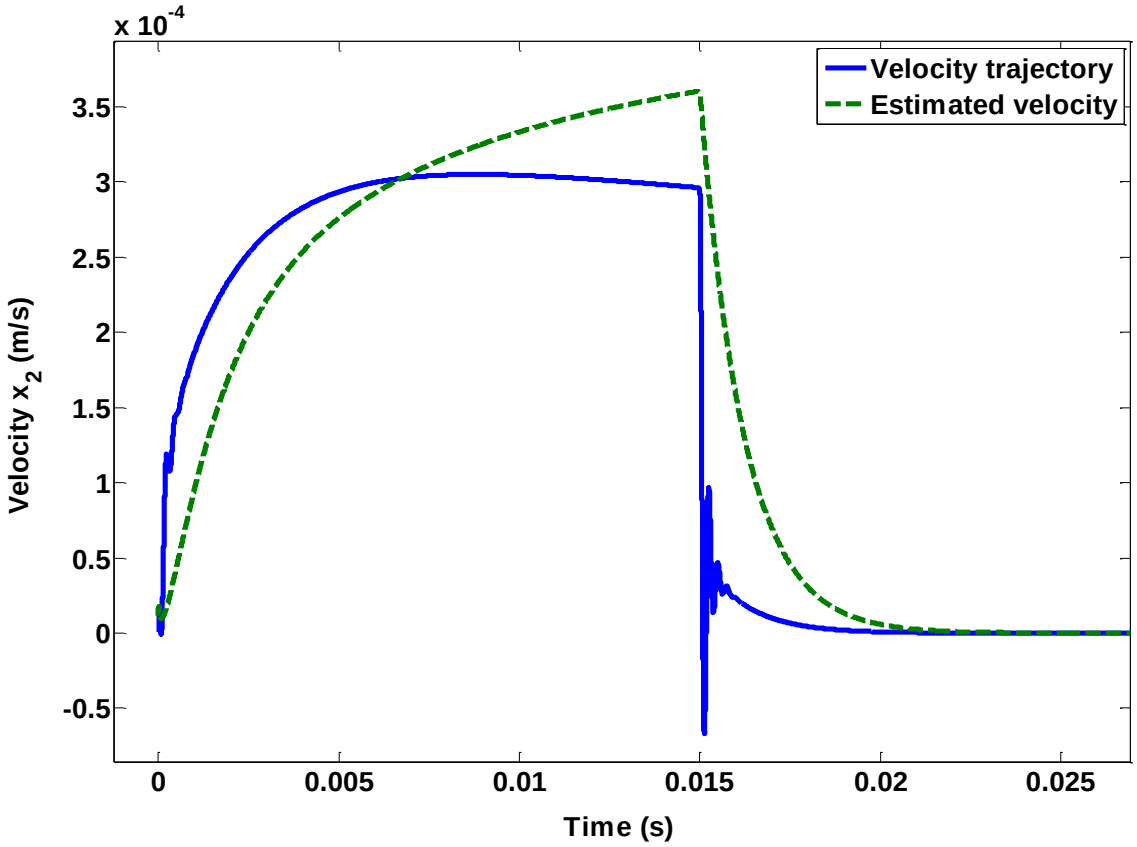

Figure 97. MEMS velocity trajectory, solid line, and the MEMS estimated velocity, dotted line.

Two of the states can be measured or estimated with the memristor, the upper plate position is measured by the memristance and the velocity is estimated by the derivative of the memristance with respect to time. The third state, which is the voltage at the MEMS, requires to be measured as well. Any direct contact with the MEMS should be avoided in order to maintain the dynamics of the actuator intact. A final closed-loop control is designed where the third state is ignored and an integrator is added with the intention to eliminate the stationary error and compensate for the unmeasured state.

5.3 FINAL CONTROL PROPOSED

The final control is a proportional-integrator-derivative (PID) like structure with the difference that the derivative gain is applied directly to the estimated velocity instead of the error. Figure 98 shows the block diagram of the final control structure, where the gains are tuned for this configuration.

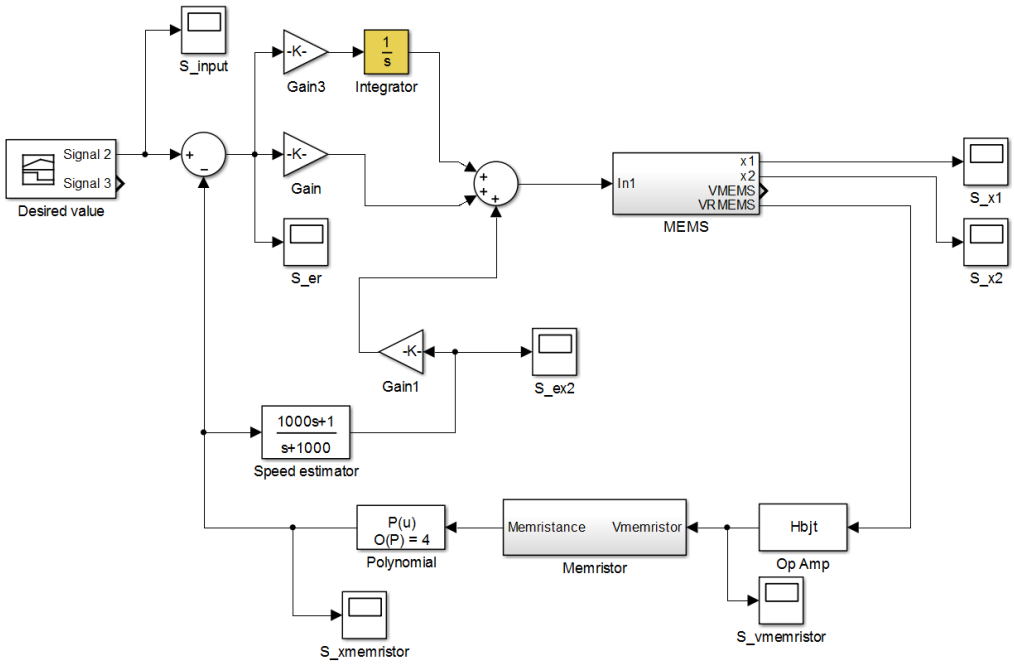

Figure 98. Block diagram representing the structure of the final closed-loop control.

Figure 99 shows the time response of the MEMS, here it is possible to observe a difference between the memristor measurement and the real MEMS trajectory. This difference is due to the polynomial fitting, the previous polynomial was calculated in range of $\frac{d}{3}$ but as the operation displacement has increased a new fitting needs to be performed to eliminate that error.

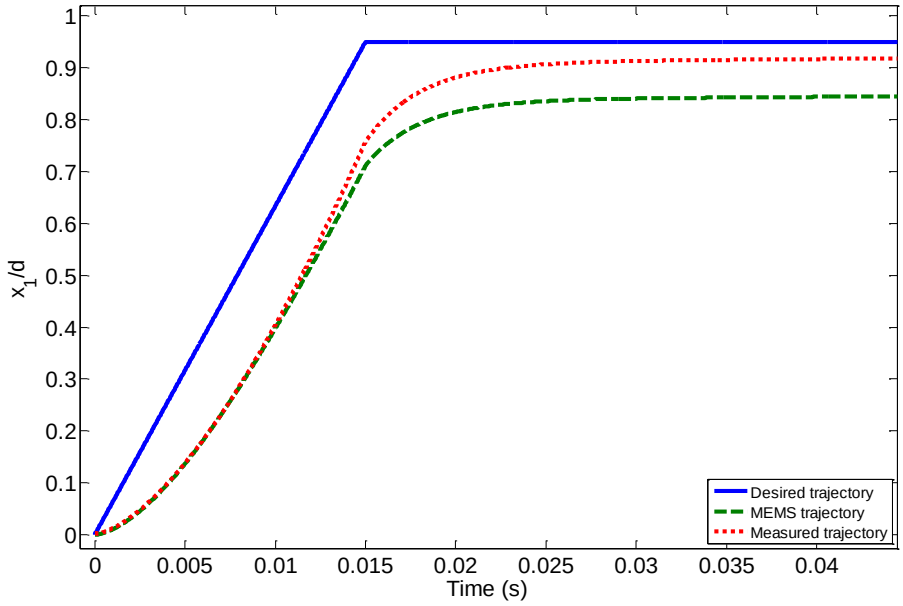

Figure 99. MEMS desired trajectory (solid line), the MEMS real trajectory (dashed line), and the measured trajectory by the memristor (dotted line).

The new fitting parameters are: p_1 = 5.917x10^{-20}, p_2 = -2.822x10^{-16}, p_3 = 8.822x10^{-13}, p_4 = -2.938x10^{-09}, and p_5 = 3.933x10^{-06}. Furthermore a fine tuning was performed for the control gains including the integration gain. The resulting gains are as follows,

$$K = \begin{bmatrix} K_1 & K_2 & K_i \end{bmatrix} = \begin{bmatrix} 1.099x10^{8} & -1.8693x10^{4} & 2x10^{9} \end{bmatrix}.$$

Equation 121

Figure 100 shows the desired trajectory versus the MEMS response for the nonlinear model using the memristor as a position sensor as well as velocity observer. Two final set points are plotted, the first one is at 95% of the total displacement and the second one is at 50%. Here it is possible to observe a minimal stationary error as well as good response to the desired trajectory.

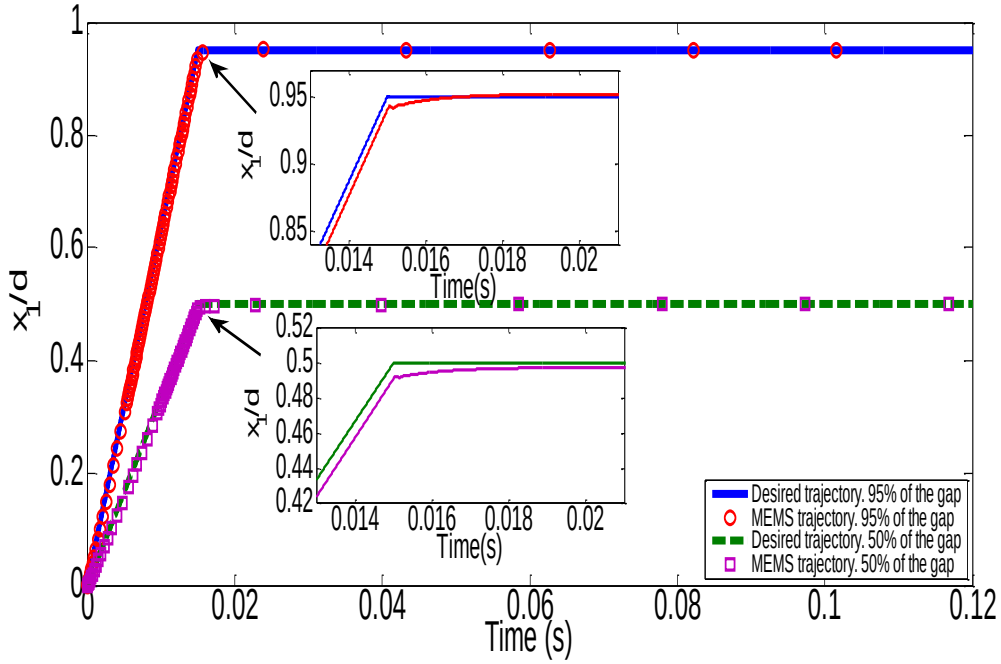

Figure 100. MEMS displacement desired trajectory versus the MEMS displacement real trajectory with fined tuned feedback gains and the memristor as feedback for the nonlinear MEMS model.

Even though the control demonstrates a very high performance where the desired trajectory is closely matched, the resistor in series with the MEMS experiences very high voltage peaks. These transitory events are amplified by the Op Amp and applied to the memristor. Figure 101 shows the input voltage to the MEMS circuit in a solid line and the voltage applied to the memristor where voltage spikes of 200 V and -400 V are present.

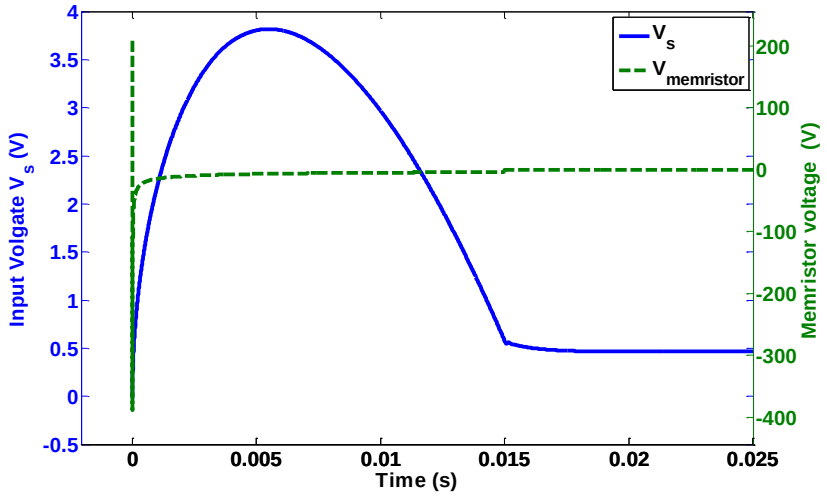

Figure 101. Input voltage to the MEMS circuit (solid line) and the voltage applied to the memristor (dotted line).

The controller can be tuned taking in account that the voltage applied to the memristor does not overpass ±10 V in order to avoid any saturation in the Op Amp or damage to the memristor. There is tradeoff between limiting the voltage and the performance following the trajectory.

After tuning the controller constraining the applied voltage to the memristor the gain constants are as follows:

$$K = \begin{bmatrix} K_1 & K_2 & K_i \end{bmatrix} = \begin{bmatrix} 2.499x10^{6} & -1.8693x10^{3} & 3x10^{7} \end{bmatrix}.$$

Equation 122

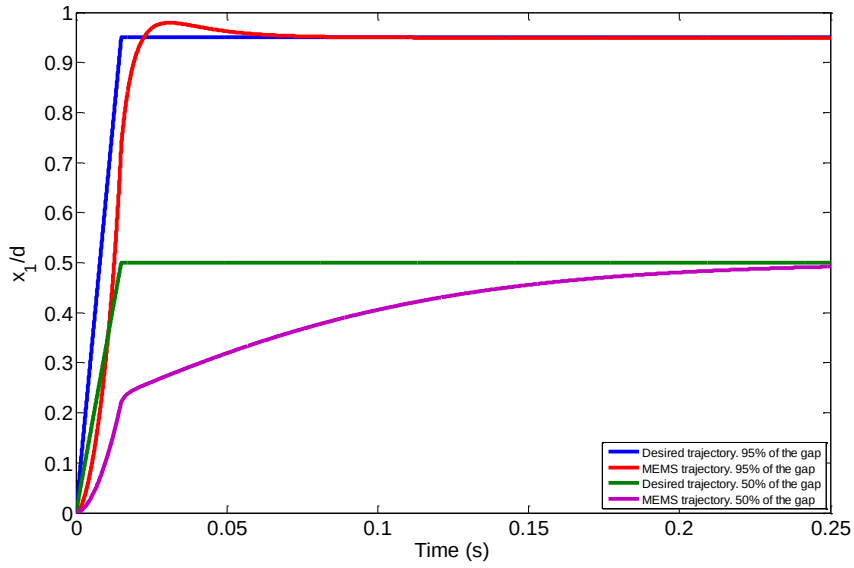

Figure 102. MEMS displacement desired trajectory versus the MEMS displacement real trajectory tuned to constrain the applied voltage to the memristor.

Figure 102 shows a desired trajectory versus the MEMS response for the nonlinear model tuning the controller to constraint the voltage applied to the memristor. The system is submitted to two different trajectories. The first one is with a final set point at 95% of the total displacement; in this case it is possible to observe that the MEMS displacement is close to the desired trajectory with small overshoot limiting the system to 95% of the total MEMS gap. As the final set point is set to a lower displacement range the MEMS displacement deviate from the desired trajectory having a delay to achieve the final set point. This is attributed to the voltage limiting and the nonlinearity of the system.

In this case the applied voltage to the memristor is within the range of ±10 V, as shown in Figure 103 where the solid line is the voltage applied to MEMS circuit and the dotted line is the voltage observed by the memristor.

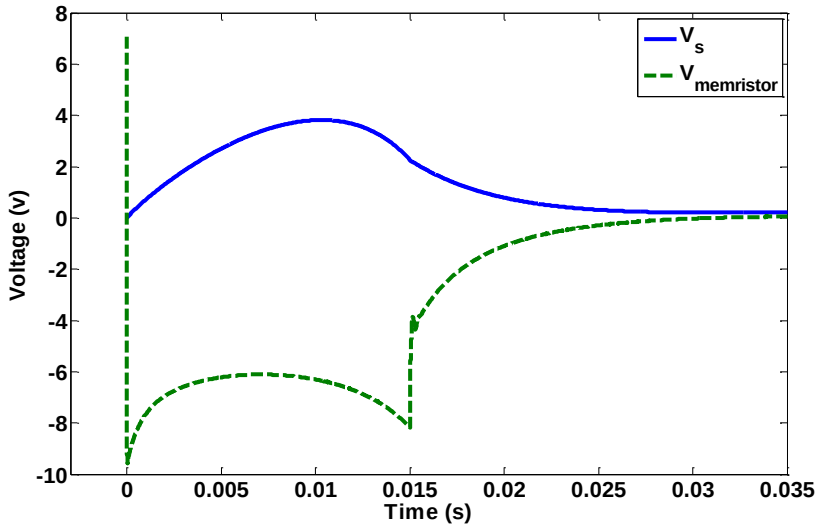

Figure 103. Input voltage to the MEMS circuit (solid line) and the voltage applied to the memristor (dotted line) with the tuned controller to limiting the voltage.

5.4 CONTROL LOOP CONCLUSIONS

In this section a design for a simple voltage closed-loop control is shown which can stabilize the MEMS upper plate position up to 95% of the total gap. The memristor is used to measure the position of the MEMS as well to estimate the velocity closing the loop for two states of the system. The final control design eliminates the measurement of the MEMS voltage to avoid any interaction with its dynamics. In order to compensate this state an integration block was added to minimize the stationary

error. The controller can be tuned to constrain the applied voltage saving power or avoiding saturation in the memristor. However there is a tradeoff with the power consumption and the system performance.

Several approaches for the controller design have been reported like: an active disturbance rejection controller (ADRC) which consists of an extended state observer that estimates the system states and the external disturbance, combined with a PD controller [72]. Another example is to use a Lyapunov-based nonlinear control [77] [78] [79], which treat the nonlinearities of the system with control Lyapunov functions and back-stepping to ensure the desired performance. All the approaches need a position (and in some cases velocity) feedback. For that reason the memristor as a sensing element and velocity estimator is not limited to one type of controller but can be employed in a wide variety of controller designs.

6 Conclusions

Memristors have attracted much attention due to its application for non-volatile memories. Its behavior has not been limited to memristor applications to the digital field but it can be used as an analog device. In this work, the analog application branch is expanded when this device is integrated to micro-electro-mechanical systems. More specifically, the memristor can play an important role when it is combined with electrostatic parallel plate MEMS actuators.

One of the main concerns for the parallel plate MEMS actuator is the limited motion of the upper plate to one third of the total gap before the plates collapse, reducing the MEMS functionality. There are different approaches to overcome this issue one of the most promising is to use a voltage closed-loop control. One limitation is the complexity of the existing feedback methods making a complex system and affecting the MEMS dynamics in some cases. This work shows the potential of the memristor to measure MEMS displacement and translate it to resistance instead of capacitance based on charge transfer.

When the MEMS and the memristor are integrated in a simple series circuit configuration it is possible to observe that the displacement can be a function of the memristance giving the possibility of interpreting the upper electrode position in form of resistance instead of capacitance. This phenomenon was observed with sinusoidal voltage inputs, with low frequencies, and with dc step, in a transient trajectory. This is not the case for high frequencies where no correlation is observed limited to the small ion mobility in the memristor. Equating the expression for the charge in both devices it is possible to observe the quadratic relationship between the MEMS dynamics and the memristance; indicating that the memristance intrinsically interprets the MEMS displacement in the form of resistance without any other calculation. However this configuration has a deficiency which is the small change in the memristance due to low memristor voltage and low current flow limited by the MEMS.

To overcome this drawback different application stages are proposed using three basic elements: a BJT amplification, a MOSFET amplification, and an Op Amp stage. For the BJT stage two transistors in cascade were needed to observe a significant change in the memristance, the memristance modulation was ~750 Ω. A gradual increase in the memristance is present after the MEMS displacement achieves

stability, this is attributed to the coupling capacitors discharge and the low impedance of the BJT transistor. This condition can be attenuated with bigger couple capacitors to increase the constant time, τ. The MOSFET case showed a larger input impedance, compared to the BJT amplifier attenuating the effect of the memristance change when the MEMS is in steady state, but this amplifier has a low amplification gain. The resistance change in the memristor was ~3 Ω for the two-transistor cascade configuration. The last amplification stage studied was the inverting Op Amp configuration showing a good amplification gain, no coupling capacitors required, and high input impedance allowing to mitigate the memristance change when the MEMS is in steady state. This Op Amp was designed using the CMOS7 Sandia National Laboratories technology and uses a Miller compensation capacitor for output stability. A memristance modulation of ~1 KΩ was observed with this amplification stage. Moreover, a quartic relationship of the memristance and the MEMS dynamics is shown by equating the charge of the MEMS device with the charge in the memristor. Thus the MEMS displacement can be interpreted with a polynomial of 4^{th} order.

Finally a simple design for a voltage closed-loop control is presented and it is shown that the MEMS upper plate position can be stabilized up to 95% of the total gap. The memristor is used to measure the position of the MEMS as well to estimate the velocity. In the final control design the measurement of the MEMS voltage is avoided to prevent any side effect in the MEMS dynamics. In order to compensate for the lack of measuring this state directly and to minimize the stationary error, an integration block was added. The controller can be tuned to constrain the applied voltage saving power or avoiding saturation in the memristor; however there is a tradeoff with the power consumption and the system performance.

These results indicate an extension to the memristor applications as well as a new method to translate the charge in the form of resistance using simpler mathematical expressions. As well, a method to improve the working range for an electrostatic MEMS actuator is presented where it can be manipulated up to 95% of the total gap with low power consumption.

7 Further work

This work opens opportunities to several research subjects. Including the following:

1. Simulate the integration of the unipolar memristor with MEMS. This work only covers the integration of the MEMS with a bipolar memristor thus the integration with the unipolar may explore other applications for both devices. A specific task would be a numerical simulation using experimental results from the unipolar memristor fabricated at the NanoMIL.

2. This purpose of this work is to explore the potential of the integration for the MEMS and the bipolar memristor. An important application was found for this configuration opening up the opportunity to experimentally probe this device configuration. UACJ in collaboration with Sandia National Laboratories have the capability to build a MEMS with the characteristics mentioned in this work. Due to the complexity of memristor fabrication an alternative is the emulation of this device. A circuit configuration is presented by Kim et al. [80] which emulates the memristor behavior.

3. The integration of the MEMS and unipolar memristors requires experimental proof. Therefore the fabrication of the MEMS by UACJ in collaboration with Sandia Nation Laboratories can be unified with unipolar SnO_2 memristors fabricated at the NanoMIL at UTEP.

4. Expanding the memristor applications, a memristor array can be used for a digital to analog converter (DAC). Switching high and low resistance creating voltage dividers as shown in Figure 104. Similar configuration has been presented using memristors with combination with Op Amp [81]. A creation of a DAC using memristor only has not been proposed.

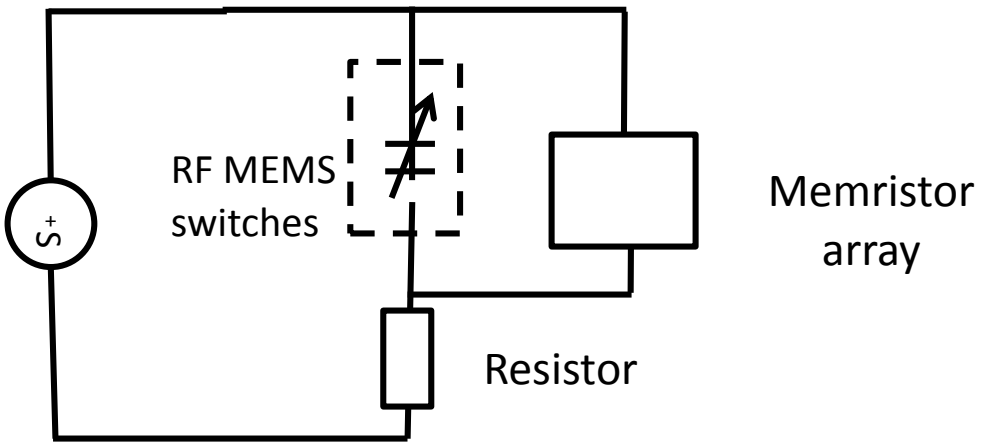

Figure 104. Memristor array that can be used as DAC creating voltage dividers

5. Other applications for the bipolar memristors have been reported as programmable op-amp filter [82] . In particular this application has not been expanded to unipolar memristor where the SnO_2 structures fabricated at UTEP can be explore for this type of applications.

References

[1] A. Sawa, "Resistive switching in transition metal oxides," *Materials today,* vol. 11, no. 6, Jun. 2008.

[2] B. Bao, Z. Liu and J. Xu, "Steady periodic memristor oscillator with transient chaotic behaviours," *Electronics Letters,* vol. 46, no. 3, pp. 237-238, Feb 2010.

[3] Y. V. Pershin, S. L. Fontaine and M. D. Ventra, "Memristive model of amoeba's learning," *Nature Precedings,* Oct. 2008.

[4] B. Linares-Barranco and T. Serrano-Gotarredona, "Memristance can explain Spike-Time-Dependent-Plasticity in Neural Synapses," *Nature Precedings,* Mar. 2009.

[5] J. Borghetti, Z. Li, J. Straznicky, X. Li, D. A. A. Ohlberg, W. Wu, D. R. Stewart and R. S. Williams, "A hybrid nanomemristor/transistor logic circuit capable of self-programming," *PNAS,* vol. 106, no. 6, Feb. 2009.

[6] R. Kozma, R. E. Pino and G. E. Pazienza, "Are Memristors the Future of AI?," in *Advances in Neuromorphic Memristor Science and Applications*, Springer Science+Business Media Dordrecht, 2012.

[7] C. K. H-L, L. S. R, Z. Y, H. R. T, B. S. F and M. R. G, "An integrated force-balanced capacitive accelerometer for low-g applications," *The 8th International Conference on Solid-state Sensors and Actuators, and Eurosensors IX,* 1995.

[8] A. Chavan and K. Wise, "Batch-processed vacuum-sealed capacitive pressure sensors," *Microelectromechanical Systems, Journal of,* vol. 10, no. 4, pp. pp.580-588, Dec 2001.

[9] S.-S. Lee, E. Motamedi and M. Wu, "Surface-micromachined free-space fiber optic switches with integrated microactuators for optical fiber communication systems," *Solid State Sensors and Actuators, 1997. TRANSDUCERS '97 Chicago., 1997 International Conference on ,* vol. 1, pp. 16-19, Jun 1997.

[10] M. Zougagh and A. Rıos, "Micro-electromechanical sensors in the analytical field," *The Royal Society of Chemistry,* vol. 134, p. 1274–1290, 2009.

[11] D. S. Greywall, P. A. Busch, F. Pardo, D. W. Carr, G. Bogart and H. T. Soh, "Crystalline Silicon Tilting Mirrors for Optical Cross-Connect Switches," *Journal of Microelectromechanical Systems,* vol. 12, no. 5, Oct. 2003.

[12] J. J. Yao, "RF MEMS from a device perspective," *J. Micromech. Microeng,* vol. 10, p. R9–R38, 2000.

[13] E. Saucedo-Flores, R. Ruelas, M. Flores and J.-c. Chiao, "Study of the Pull-In Voltage for MEMS Parallel Plate Capacitor Actuator," *Materials Research Society,* pp. 1-5, Dec 2003.

[14] A. Kaiser, "The potential of MEMS components for re-configurable RF interfaces in mobile communication terminals," *Solid-State Circuits Conference,* pp. 25-28, Sept 2001.

[15] D. Zubia, S. Almeida, A. Talukdar, J. Mireles and E. MacDonald, "SnO2-based memristors and the potential synergies of integrating memristors with MEMS," *SPIE 8373, Micro- and Nanotechnology Sensors, Systems, and Applications IV,* vol. 83731V, May 2012.

[16] L. O. Chua, "Memristor—the missing circuit element," *IEEE Trans. Circuit Theory,* Vols. CT-18,

no. 5, p. 507–519, Sept. 1971.

[17] L. O. Chua, "The Fourth Element," vol. 100, no. 6, 2012.

[18] S. Almeida, "Resistive switching of tin dioxide (SnO2) for memristor applications," 2010.

[19] R. S. Williams, "How We Found the Missing Memristor," *IEEE Spectrum,* pp. 30-35, Dec 2008.

[20] D. B. Strukov, G. S. Snider, D. R. Stewart and R. S. Williams, "The missing memristor found," *Nature,* vol. 453, pp. 80-83, May 2008.

[21] R. Waser and M. Aono, "Nanoionics-based resistive switching memories," *Nature Materials,* vol. 6, Nov. 2007.

[22] R. Waser, "Nanoionics-based resistive switching memories," *Nature Materials,* vol. 6, Nov. 2007.

[23] S. Lee, H. Kim, D.-J. Yun, S.-W. Rhee and K. Yong, "Resistive switching characteristics of ZnO thin film grown on stainless steel for flexible nonvolatile memory devices," *Applied Physics Letters,* vol. 95, no. 262113-1, Dec 2009.

[24] S.-Y. Wang, D.-Y. Lee, T.-Y. Tseng and C.-Y. Lin, "Effects of Ti top electrode thickness on the resistive switching behaviors of rf-sputtered ZrO2 memory films," *Applied Physics Letters,* vol. 95, no. 112904, Aug. 2009.

[25] M. Chan, T. Zhang, V. Hob and P. Lee, "Resistive switching effects of HfO2 high-k dielectric," *Microelectronic Engineering,* vol. 85, no. 12, Dec. 2008.

[26] M. K. Yang, J.-W. Park, T. K. Ko and a. J.-K. Lee, "Bipolar resistive switching behavior in Ti/MnO2 /Pt structure for nonvolatile memory devices," *Applied Physics Letters,* vol. 95, no. 042105, Jul. 2009.

[27] J. J. Yang, M. D. Pickett, X. Li, D. A. A. Ohlberg, D. R. Stewart and R. S. Williams, "Memristive switching mechanism for metal/oxide/metal nanodevices," *Nature Nanotechnology,* vol. 3, no. 429-433, Jun. 2008.

[28] J. W. Seo, J.-W. Park, K. S. Lim, S. J. Kang and Y. H. Hong, "Transparent flexible resistive random access memory fabricated at room temperature," *Applied Physics Letters,* vol. 95, no. 133508, Sep. 2009.

[29] H. Peng and T. Wua, "Nonvolatile resistive switching in spinel ZnMn2O4 and ilmenite ZnMnO3," *Applied Physics Letters,* vol. 95, no. 152106, Oct. 2009.

[30] S.-O. Kang, S. Hong, J. Choi, J.-S. Kim and I. Hwang, "Electrochemical growth and resistive switching of flat-surfaced and (111)-oriented Cu2O films," *Applied Physics Letters,* vol. 95, no. 092108, Sep. 2009.

[31] S. Almeida, B. Aguirre, N. Marquez, J. McClure and D. Zubia, "Resistive Switching of SnO2 Thin Films on Glass Substrates," *Integrated Ferroelectrics ,* 2011.

[32] P. Mazumde, S. M. Kang and R. Waser, "Memristors: Devices, Models, and Applications," vol. 100, no. 6, pp. 1911-1919, 2012.

[33] Y. H. Do, J. S. Kwak, Y. C. Bae, K. Jung, H. Im and J. P. Hong, "Hysteretic bipolar resistive switching characteristics in TiO2 /TiO2−x multilayer homojunctions," vol. 95, 2009.

[34] D. B. Strukov and S. Williams, "Exponential ionic drift: fast switching and low volatility of thin-film memristors," vol. 95, 2008.

[35] J. Bryzek, "Control Issues for MEMS," *Proceedings of the 42nd IEEE Conference on Decision and Control,* pp. 3039-3047, Dec. 2003.

[36] J. Bryzek, "Emergence of a $ Trillion MEMS sensor market," in *Nanotechradar*, Hayward, 2012.

[37] A. Dec and K. Suyama, "Microwave MEMS-Based Voltage-Controlled Oscillators," *IEEE*

Transactions On Microwave Theory And Techniques, vol. 48, no. 11, Nov. 2000.

[38] G. M. Rebeiz and J. B. Muldavin, "RF MEMS switches and switches circuits," 2001.

[39] U. Hofmann, M. Aikio, J. Janes, F. Senger, V. Stenchly, M. Weiss, H.-J. Quenzer, B. Wagner and W. Benecke, "Resonant biaxial 7-mm MEMS mirror for omnidirectional scanning," 2013.

[40] J. A. Perreault, T. G. Bifano, B. M. Levine and M. N. Horenstein, "Adaptive optic correction using microelectromechanical deformable mirrors," vol. 41, no. 3, 2002.

[41] T. Juneau, K. Unterkofler, T. Seliverstov, S. Zhang and M. Judy, "Dual-axis optical mirror positioning using a nonlinear colsed-loop controller," 2003.

[42] L. Y. Lin and E. L. Goldstein, "Opportunities and Challenges for MEMS in Lightwave Communications," vol. 8, no. 1, 2002.

[43] J. I. Dadap, I. B. P. B. Chu, C. D. L. C. Pu, N. B. K. Bergman, T. Chau, M. Chou, R. Doran, R. Gibson, R. Harel, J. J. Johnson, S. S. Lee, S. Park, D. R. Peale, R. Rodriguez, M. T. D. Tong, W. Z. C. Wu, E. L. Goldstein and L. Y. Lin, "Modular MEMS-Based Optical Cross-Connect With Large Port-Count," vol. 15, no. 12, 2003.

[44] T. Brosnihan, S. Brown, A. Brogan, C. Gormley, D. Collins, S. Sherman, M. Lemkin, N. Polce and M. Davis, "Optical Imems ® – A Fabrication Process For Mems Optical Switches With Integrated On-Chip Electronics," 2003.

[45] T.-W. Yeow, K. L. E. Law, a. A. Goldenberg and U. o. Toronto, "MEMS Optical Switches," 2001.

[46] K. Nagashima, T. Yanagida, K. Oka and T. Kawai, "Unipolar resistive switching characteristics of room temperature grown SnO2 thin films," vol. 94, 2009.

[47] Y. Yang, P. Gao, S. Gaba, T. Chang, X. Pan and W. Lu, "Observation of conducting filament growth in nanoscale resistive memoreis," *Nature communications,* vol. 3, no. 732, 2012.

[48] D. R. Stewart, D. A. A. Ohlberg, P. A. Beck, Y. Chen and a. R. S. Williams, "Molecule-Independent Electrical Switching in Pt/Organic Monolayer/Ti Devices," vol. 4, no. 1, 2004.

[49] Y. N. Joglekar and S. J. Wolf, "The elusive memristor: properties of basic electrical circuits," vol. 30, 2009.

[50] Z. BIOLEK, D. BIOLEK and V. BIOLKOVÁ, "SPICE Model of Memristor with Nonlinear Dopant Drift," vol. 18, no. 2, 2009.

[51] T. Prodromakis, B. P. Peh, C. Papavassiliou and C. Toumazou, "A versatile memristor model with non-linear dopant kinetics," vol. 58, no. 9, 2011.

[52] P. R. Mickel, A. J. Lohn, B. J. Choi, J. J. Yang, M.-X. Zhang, M. J. Marinella, C. D. James and R. S. Williams, "A physical model of switching dynamics in tantalum oxide memristive devices," vol. 102, no. 223502, 2013.

[53] M. D. Pickett, D. B. Strukov, J. L. Borghetti, J. J. Yang, G. S. Snider, D. R. Stewart and R. S. Williams, "Switching dynamics in titanium dioxide memristive devices," vol. 106, no. 074508, 2009.

[54] J. G. Simmons, "Electric tunnel effect between dissimilar electrodes separeted by a thin insulating film," vol. 34, no. 9, 1963.

[55] H. Abdalla and M. D. Pickett, "SPICE Modeling of Memristors," 2011.

[56] S. Kvatinsky, E. G. Friedman, A. Kolodny and U. C. Weiser, "TEAM: ThrEshold Adaptive Memristor Model," vol. 60, no. 1, 2013.

[57] T. Xiao-Bo, X. Hui and L. Qing-Jiang, "The conductive mechanisms of a titanium oxide memristor with dopant drift and a tunnel barrier," vol. 22, no. 8, 2013.

[58] M. Bao, Analysis and Design Principles of MEMS Devices, Elsevier, 2005.

[59] S. a. D. Z. Almeida, "Integration of memristors with MEMS in different circuit configurations.," in *NSTI-Nanotech 2013*, Washintong, 2013.

[60] R. Boylestad and L. Nashelsky, Electronic Devices and Circuit Theory, Pearson, 2009.

[61] Inductiveload, "wikipedia," 2 08 2010. [Online]. Available: http://en.wikipedia.org/wiki/Bipolar_junction_transistor. [Accessed 6 11 2013].

[62] K. Kano, Semiconductor Devices, Prentice-Hall, 1998.

[63] C. M. o. Macao, "How an npn Bipolar Junction Transistor (BJT) works," Communications Museum of Macao, 04 05 2013. [Online]. Available: http://macao.communications.museum/eng/exhibition/secondfloor/moreinfo/2_10_3_howtransistorworks.html. [Accessed 6 11 2013].

[64] B. Nashelsky, Electronic Devices and Circuit Theory, Pearson, 2003.

[65] L. Fuller, "MicroE," Rochester Institute of Technology, 21 03 2012. [Online]. Available: http://people.rit.edu/lffeee/BJT_Amplifiers.pdf. [Accessed 6 11 2013].

[66] "Brigham Young University," Brigham Young University, [Online]. Available: http://www.cleanroom.byu.edu/MOSFET_calc.parts/14.jpg. [Accessed 6 11 2013].

[67] S.-M. Kang and Y. Leblebici, CMOS Digital Integrated Circuits, New York: Tara McGraw-Hill, 2003.

[68] S. Franco, Design with operational amplifiers and analog integrated circuits, New York: McGraw-Hill, 2002.

[69] E. K. Chan and R. W. Dutton, "Electrostatic Micromechanical Actuator with Extended Range of Travel," *JOURNAL OF MICROELECTROMECHANICAL SYSTEMS,* vol. 9, no. 3, 2000.

[70] J. I. Seeger and B. E. Boser, "Charge Control of Parallel-Plate, Electrostatic Actuators and the Tip-In Instability," *JOURNAL OF MICROELECTROMECHANICAL SYSTEMS,* vol. 15, no. 5, 2003.

[71] P. B. Chu and K. S. J. Pister, "Analysis of Closed-loop Control of Parallel-Plate Electrostatic MicroGrippers," *Robotics and Automation, 1994. Proceedings., 1994 IEEE International Conference,* vol. 1, pp. pp.820-825 , May 1994.

[72] L. Dong, "Closed-loop Voltage Control of a Parallel-plate MEMS Electrostatic Actuator," in *American Control Conference*, Baltimore, 2010.

[73] D. Hah, S. T.-Y. Huang, J.-C. Tsai, H. Toshiyoshi and M. C. Wu, "Low-Voltage, Large-Scan Angle MEMS Analog Micromirror Arrays With Hidden Vertical Comb-Drive Actuators," *Journal Of Microelectromechanical Systems,* vol. 13, no. 2, Apr. 2004.

[74] R. C. Anderson, B. Kawade, K. Ragulan, D. H. S. Maithripala, J. M. Berg, R. O. Galec and W. P. Dayawansa, "Integrated charge and position sensing for feedback control of electrostatic MEMS," in *Sensors and Smart Structures Technologies for Civi, lMechanical, and Aerospace Systems*, Bellingham, 2005.

[75] M. S.-C. Lu and G. K. Fedder, "Position Control of Parallel-Plate Microactuators for Probe-Based Data Storage," *Journal Of Microelectromechanical Systems,* vol. 13, no. 5, Oct. 2004.

[76] R. A. Diasa, P. J. Macedo, H. D. Silva, R. F. Wolffenbuttel, E. Cretu and L. A. Rocha, "Closed-loop operated time-based accelerometer," vol. 47, 2012.

[77] G. Zhu, J. L´evine and L. Praly, "Improving the Performance of an Electrostatically Actuated MEMS by Nonlinear Control: Some Advances and Comparisons," in *Proceedings of the 44th IEEE Conference on Decision and Control, and the European Control Conference 2005*, Seville,

Spain, 2005.

[78] G. Zhu and L. Saydy, "Robust Output Feedback Control of an Electrostatic Micro-Actuator," in *American Control Conference*, New York City, 2007.

[79] G. Zhu, J. Penet and L. Saydy, "Robust Control of an Electrostatically Actuated MEMS in the Presence of Parasitics and Parametric Uncertainties," in *American Control Conference*, Minnesota, 2006.

[80] H. Kim, M. P. Sah, C. Yang, S. Cho and L. O. Chua, "Memristor Emulator for Memristor Circuit Applications," *IEEE TRANSACTIONS ON CIRCUITS AND SYSTEMS,* vol. 99, no. 10, pp. 2422-2431, 2012.

[81] L. Gao, F. Merrikh-Bayat, F. Alibart, X. Guo, B. D. Hoskins, K.-T. Cheng and D. B. Strukov, "Digital-to-Analog and Analog-to-Digital Conversion with Metal Oxide Memristors for Ultra-Low Power Computing," in *Proc. NanoArch'13*, New York, 2013.

[82] R. Berdan, T. Prodromakis, I. Salaoru, A. Khiat and C. Toumazou, "Memristive devices as parameter setting elements in programmable gain amplifiers," *Applied Physics Letters,* vol. 101, no. 24, pp. pp.243502-243502-3, Dec 2012.

Appendix A

This appendix contains the Matlab code for function and scripts developed to solve models and circuits in this work.

Matlab code used to solve the memristor model for section 2.1.1. This script can run all the functions below on changing the @function name at the ode45 line.

```
%***********Matlab script to solve memristor models and MEMS**************

%*****************Memristor parameters************************************
Ron = 100;                              %High resistance value Ron (Ohms)
Roff = 5000;                            %Low resistance value Ron (Ohms)
uv = 1e-14;                             %Average ion mobility (m^2V^-1s^-1)
D = 10e-9;                              %Device length (m)
w0 = 1e-9;                              %initial condition for state variable (m)
p =2;

%************************MEMS parameters**********************************
e0 = 8.854e-12;                         %Vacuum permittivity (F/m)
d = 5e-6;                               %Plates distance (m)
k = 0.3125;                             %spring constant (N/m)
A = (300e-6)^2;                         %Plates area (m^2)
dc = 5e-5;                              %Damping constant (Kg/s)
rho = 2329;                             %Upper plate density (Kg/m^3)
h = 2e-6;                               %Upper plate thickness (m)
m = rho*A*h;                            %Upper electrode mass (Kg)
x10 = 0;                                %Position initial condition (m)
x20 = 0;                                %Velocity initial condition (m/s)
fVpi = 1;                               %Vpi factor, if 1 input voltage = Vpi

%*****************************************************************************

options = odeset('RelTol',...           %Solver parameters, tolerance solution
    1e-12,'AbsTol',1e-12,...            %set at 1e-9 m, and maximum step time
    'MaxStep',1e-5);                    %1 ms.

trange = [0,0.25];                      %Time range to solve LDD model

wfreq = 2*pi;                           %Input voltage frequency (rad/s)
amp = 0.85;                             %Input voltage amplitude (V)
offset = 0;                             %Input voltage phase shift (rad)

[tsp,wmem]=ode45(@memristor,...         %Numerical solution for LDD model
    trange,w0,options,wfreq,...         %ode45 function was used.
    amp,offset,Ron,Roff,uv,D);          %Output value w (m) and time (s)

[Stsp,Swmem]=ode45(@NDDStrukov,...      %Numerical solution for SNDD model
    trange,w0,options,wfreq,...         %ode45 function was used.
    amp,offset,Ron,Roff,uv,D);          %Output value w (m) and time (s)

[Jtsp,Jwmem]=ode45(@NDDJoglekar,...     %Numerical solution for JNDD model
```

```
    trange,w0,options,wfreq,...          %ode45 function was used.
    amp,offset,Ron,Roff,uv,D,p);         %Output value w (m) and time (s)

[Mtsp,yMEM]=ode23s(@tMEMS,...           %Numerical solution for MEMS model
    trange,[x10 x20],options,wfreq,...   %ode23s function was used.
    amp,offset,e0,d,k,A,dc,m,fVpi);      %Output value w (m) and time (s)
```

In order to run the matlab functions below an m file needs to be created with the function name

```
%*************LDD model function to solve w*******************************
function wsol = memristor(t,y,wfreq,amp,offset,Ron,Roff,uv,D)

Rres = Ron*y/D+Roff*(1-y/D);              %Memristance (Ohms)
Vs = amp*(sin(wfreq*t-offset));           %Input voltage (V)

wsol = uv*Ron*Vs/(Rres*D);                %dw/dt state variable
                                          %differential equation
t                                         %Solution progress display


%*************NDD Strukov model function to solve w************************
function wsol = NDDStrukov(t,y,wfreq,amp,offset,Ron,Roff,uv,D)

Rres = Ron*y/D+Roff*(1-y/D);                %Memristance (Ohms)
Vs = amp*(sin(wfreq*t-offset));             %Input voltage (V)

f = y*(D-y)/D^2;
wsol = uv*Ron*Vs/(Rres*D)*f;                %dw/dt state variable
                                            %differential equation

t                                           %Solution progress display


%*************NDD Joglekar model function to solve w***********************
function wsol = NDDJoglekar(t,y,wfreq,amp,offset,Ron,Roff,uv,D,p)

Rres = Ron*y/D+Roff*(1-y/D);                %Memristance (Ohms)
Vs = amp*(sin(wfreq*t-offset));             %Input voltage (V)

f = 1-(2*y/D-1)^(2*p);
wsol = uv*Ron*Vs/(Rres*D)*f;                %dw/dt state variable
                                            %differential equation

t                                           %Solution progress display

%*************MEMS Transient solution *************************************
function ysol = tMEMS(t,y,wfreq,amp,offset,e0,d,k,A,dc,m,fVpi)


Vs = fVpi*sqrt(8*k*d^3/(27*A*e0));          %MEMS applied voltage

ysol1 = y(2);                               %MEMS velocity dx/dt

ysol2 = e0*A*Vs^2/(2*m*(d-y(1))^2)...       %MEMS acceleration d2x/dt2
    -dc*y(2)/m-k*y(1)/m;
```

```
t                                          %Solution progress display

ysol = [ysol1;ysol2];

%**********MEMS with resistor Transient solution *************************
function ysol = tResMEMS(t,y,wfreq,amp,offset,e0,d,k,A,dc,m,fVpi,R)


Vs = fVpi*sqrt(8*k*d^3/(27*A*e0));         %Circuit voltage Vs

ysol1 = y(2);                              %MEMS velocity dx/dt

ysol2 = e0*A*y(3)^2/(2*m*(d-y(1))^2)...    %MEMS acceleration d2x/dt2
    -dc*y(2)/m-k*y(1)/m;


ysol3 = (Vs-y(3))*(d-y(1))/(R*e0*A)...     %dVMEMS/dt derivative of the
    -y(2)*y(3)/(d-y(1));                   %voltage at the MEMS

t                                          %Solution progress display

ysol = [ysol1;ysol2;ysol3];


%**********memristor and MEMS Transient solution *************************
function ysol = tmemMEMS(t,y,wfreq,amp,offset,e0,d,k,A,dc,m,fVpi,Ron,...
    Roff,uv,D)

Rres = Ron*y(4)/D+Roff*(1-y(4)/D);         %Memristance (Ohms)

Vs = fVpi*sqrt(8*k*d^3/(27*A*e0));         %Circuit voltage Vs

ysol1 = y(2);                              %MEMS velocity dx/dt

ysol2 = e0*A*y(3)^2/(2*m*(d-y(1))^2)...    %MEMS acceleration d2x/dt2
    -dc*y(2)/m-k*y(1)/m;


ysol3 = (Vs-y(3))*(d-y(1))/(Rres*e0*A)...  %dVMEMS/dt derivative of the
    -y(2)*y(3)/(d-y(1));                   %voltage at the MEMS

ysol4 = uv*Ron*(Vs-y(3))/(Rres*D);         %dw/dt state variable
                                           %differential equation


t                                          %Solution progress display

ysol = [ysol1;ysol2;ysol3;ysol4];
```

Curriculum vitae

Sergio Fabian Almeida earned his Bachelor of Engineering degree in Mechatronics Engineering from Tecnologico de Monterrey campus Juarez in 2007. He received his Master of Science degree in Electrical and Computer Engineering from the University of Texas at El Paso in 2010, his thesis title: "Resistive Switching of Tin Dioxide (SnO_2) for Memristor Applications" supervised by Dr. David Zubia. In 2010 he joined the doctoral program in Electrical and Computer Engineering at the University of Texas at El Paso.

Dr. Almeida was awarded from 2009 to 2010 with the Chihuahua state Scholarship for academic merits. He also earned experience in the industry while pursuing his degree including: product development at Delphi Mexico Technical Center and Technical Specialist for product testing at Cummins.

He has been part of the nanoMIL research group where he performed research activities in the nanoelectronics field. His research has been presented in international conferences including: Microelectronics and MEMS of the VI International Conference on Surfaces and NSTI-Nanotech 2013 Washington DC conference. Furthermore his work has been published in SPIE Micro- and Nanotechnology Sensors Systems and Applications proceedings and the Integrated Ferroelectrics journal.

Dr. Almeida worked as a teacher and research assistant at the University of Texas at El Paso, where he has mentored several students. He is looking forward for a postdoctoral position where he can continue his academic career.

Dr. Almeida's dissertation title "Integration of memristors with MEMS for dynamic displacement control" under Dr. Zubia and Dr. Mireles Jr. supervision.

Permanent address: 2424 Bosque de Palma
Juárez, Chihuahua, 32539

This thesis/dissertation was typed by Sergio Fabian Almeida